Journal of Nanomaterials

Synthesis and Applications of Multifunctional Nanomaterials Composites

Lead Guest Editor: Chandragiri V. Reddy
Guest Editors: Kakarla R. Reddy, R.V. Ravikumar, Inturu Omkaram, and Bathula Babu

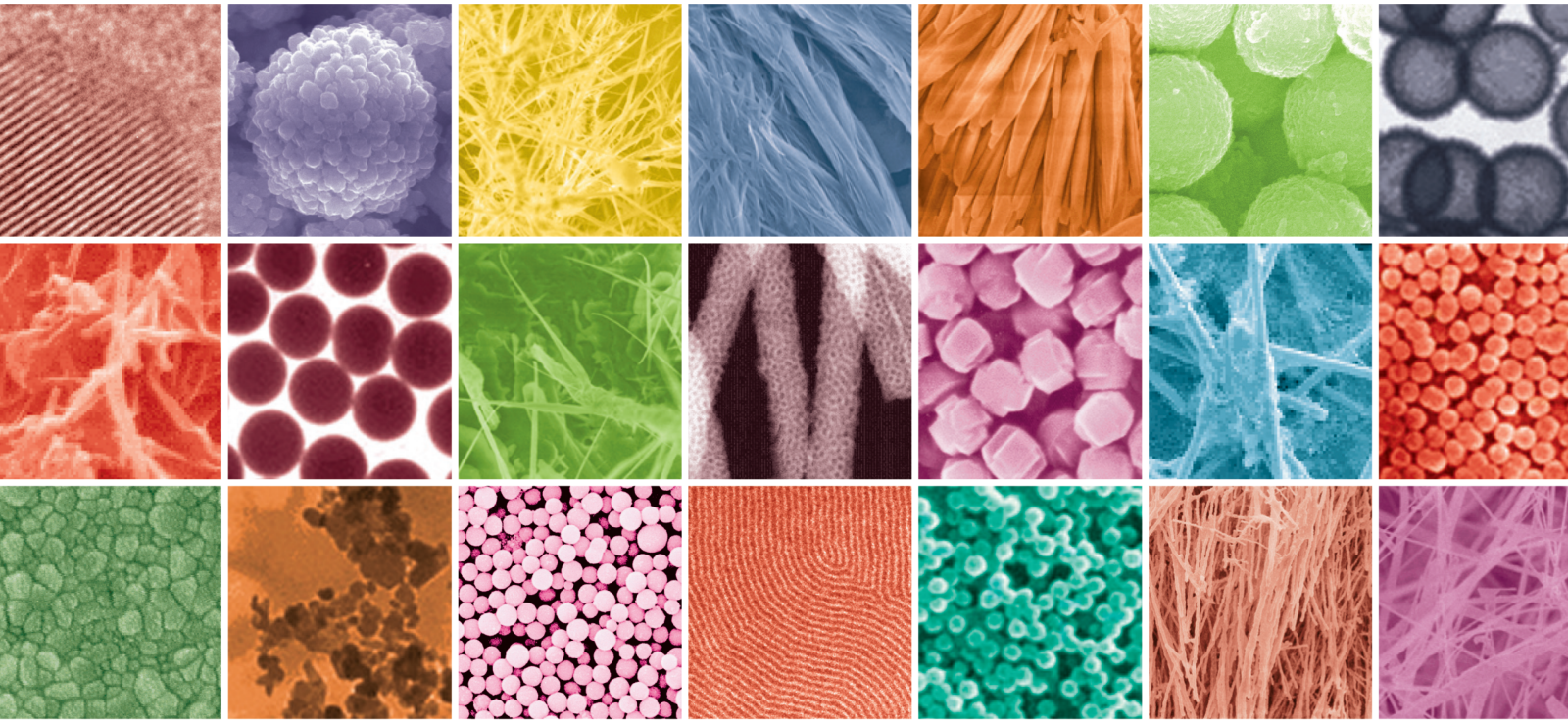

Synthesis and Applications of Multifunctional Nanomaterials Composites

Journal of Nanomaterials

Synthesis and Applications of Multifunctional Nanomaterials Composites

Lead Guest Editor: Chandragiri V. Reddy
Guest Editors: Kakarla R. Reddy, R.V. Ravikumar, Inturu Omkaram, and Bathula Babu

Contents

Hindawi
Journal of Nanomaterials
Volume 2019, Article ID 1251598, 8 pages
https://doi.org/10.1155/2019/1251598

Research Article

Synthesis of High-Quality Carboxyl End-Functionalized Poly(3-hexylthiophene)/CdSe Nanocomposites

He-Ping Shi,[1] Da-Wei Lin,[2] and Rui-feng Wu[2]

[1]*College of Science, Inner Mongolia Agricultural University, Hohhot, Inner Mongolia 010018, China*
[2]*College of Chemical Engineering, Inner Mongolia University of Technology, Hohhot 010051, China*

Correspondence should be addressed to Rui-feng Wu; rfwu02@163.com

Received 26 September 2018; Accepted 18 August 2019; Published 15 September 2019

Guest Editor: Kakarla R. Reddy

Carboxyl end-functionalized poly(3-hexylthiophene) (P3HT-COOH) was grafted chemically with CdSe nanocrystals (NCs) by a phosphine-free method. The particle quality of P3HT-COOH/CdSe nanocomposites was better than that of P3HT/CdSe nanocomposites, which were synthesized using the same method. Nanocrystals with controllable particle size exhibited a wurtzite crystalline structure and showed excellent nanocrystal dispersion in the P3HT-COOH matrix. Photoluminescence (PL) characterization performed on nanocomposites suggested the efficient charge transfer at the P3HT-COOH/CdSe interface. This approach based on the phosphine-free method is not only environmentally friendly but also highly efficient.

1. Introduction

P3HT has been extensively utilized as conjugated polymers (CPs) for CP/CdSe nanocomposites due to its well-matched energy level with CdSe [1–5]. However, P3HT/CdSe was widely prepared by physically mixing P3HT and CdSe. Phase separation of P3HT and CdSe is inevitable, thereby limiting the direct electronic interaction between them [6–8]. Grafting P3HT with CdSe by a chemical method is an effect strategy to eliminate phase separation and to promote the electronic interaction between P3HT and CdSe [6, 8]. Previously, the ligand exchange process was used to graft CPs to NCs because the derivatization of the composite has a broad range of functional groups [9, 10]. In spite of the fact that the original ligands can be replaced by the desired ligands, NCs still tend to aggregate when mixed with CPs, which leads to phase separation [11–14].

A strategy to decrease or eliminate macrophase separation is to use end-functionalized P3HT as ligands [2, 8, 15–17]. End-functionalized P3HT equipped with alcohol, ethynyl, carboxylic acid, pyridines, thiols, amine, and phosphate groups has been developed [14, 17–19]. The research shows that it also generates chemically defined interfaces that improve electronic communication between the CPs and NCs. Polythiophene with carboxylic acid functional groups has been used to prepare many nanocomposites because it increases the interactions at the interface with the NCs [20–22]. Photoinduced electron transfer from CPs to NCs was also improved by replacing the P3HT with P3HT-COOH [23].

Many works on the synthesis of CP/NC nanocomposites have been reported [9, 19, 24–31]. But some key chemicals, such as tri-n-octylphosphine oxide (TOPO) and trioctylphosphine (TOP), used in traditional routes are extremely toxic, expensive, explosive, and pyrophoric [7, 11, 12, 28, 31]. So phosphine-free synthesis schemes have extended to green and low-cost cadmium carboxylate precursors, fatty acid ligands, and noncoordination solvents (ODE, heat transfer fluids, and paraffin liquid) [32–34]. P3HT/CdSe has been successfully synthesized in ODE without using TOP and TOPO [4]. The result shows that it is a uniform dispersion of NCs without any indication of phase separation. However, this method is not desirable because dimethylcadmium is used, which is a pyrophoric and explosive reagent. CdSe NCs obtained from the phosphine-free solvent systems are generally imperfect. The size of CdSe NCs is not easily controlled [9, 32, 35], and their surface is not suitable for epitaxial

growth [36, 37]. An environmentally friendly, effective, and ligand exchange-free method should be developed to achieve chemically grafted CPs on the QD surface.

In this paper, two kinds of P3HT-COOH/CdSe nanocomposites were prepared by an in situ synthesis method without using organophosphine as a ligand. The p-type/n-type hybrid nanocomposites have high quality and show fluorescence quenching, indicating an effective charge transfer at the interface between P3HT-COOH and CdSe.

2. Experiment

2.1. General Procedures and Chemicals. All reactions were carried out under nitrogen gas flow using a standard Schlenk line. The glassware was predried before use at 120°C. All chemicals, including 1-octadecene (ODE), trichlorobenzene, selenium powder, ethynylmagnesium bromide (1 mol/L in THF), and P3HT (number average molecular weight was 30,000 g/mol), were purchased from J&K (China). Cadmium stearate was purchased from Aladdin (China). THF (Aladdin, 99%) was refluxed over sodium wire.

2.2. Synthesis of Ethynyl-Terminated P3HT. Ethynyl-terminated P3HT (i.e., P3HT-≡) was synthesized by the quasiliving Grignard metathesis (GRIM) method [38]. P3HT (0.09 g, 0.03 mmol) was dissolved in 20 mL THF, and Ni(dppp)Cl_2 (0.0225 g, 0.041 mmol) was added. The resulting mixture was first stirred for 10 min at room temperature, followed by a reaction with ethynylmagnesium bromide (0.03 mL, 0.03 mmol) in THF for 30 min. The product, P3HT-≡, was obtained by precipitating the reaction mixture in methanol, filtering in an extraction thimble, and washing by Soxhlet extraction with methanol, hexanes, and chloroform sequentially.

2.3. Synthesis of P3HT-COOHs. P3HT-COOHs contain P3HT-Z-COOH, and P3HT-M-COOH is synthesized by click reaction [38] (Scheme 1). The 4-aminophenylacetic acid (i.e., Z) and sodium azide were mixed in water to substitute the amino group of 4-aminophenylacetic acid into azide (N_3), yielding N_3-functionalized-phenylacetic acid complexes (Z-N_3). The 4-(bromomethyl)benzoic acid (i.e., M) and sodium azide were mixed in DMF to substitute the bromide group of 4-(bromomethyl)benzoic acid into azide (N_3), yielding N_3-functionalized-methylbenzoic acid complexes (M-N_3).

Subsequently, the synthesized P3HT-≡ and Z-N_3 or M-N_3 were mixed in THF and kept at 60°C under Ar for 3 days, yielding P3HT-Z-COOH or P3HT-M-COOH complexes. The resulting solution was precipitated in methanol to remove the excess amount of Z-N_3 or M-N_3, which was not coupled with P3HT-≡.

2.4. Synthesis of the Se Precursor. Selenium powder 0.079 g (1.0 mmol) was added to a three-necked flask with 2 mL of oleylamine and 10 mL of ODE, and the mixture was then stirred under Ar at 220°C to produce an optically clear solution.

2.5. Synthesis of P3HT-COOH/CdSe Nanocomposites. P3HT-COOHs 0.009 g (0.500 mmol) and cadmium stearate 0.395 g (0.500 mmol) were mixed in ODE (13 mL) and trichlorobenzene (1 mL) and kept at 220°C under Ar until the liquid color was bright orange. The product is P3HT-COO-Cd solution (P3HT-Z-COO-Cd or P3HT-M-COOH-Cd). Subsequently, 10 mL Se precursor solution was rapidly injected into the P3HT-COOH-Cd solution. The reaction solution color immediately changed to brown from bright orange indicating the formation of CdSe nanoparticles. Nanoparticles were allowed to grow at 220°C for 1 h. The resulting P3HT-COOH/CdSe nanocomposites were cooled down and precipitated with methanol and redissolved in chloroform.

3. Characterizations

The morphology of P3HT-COOH/CdSe nanocomposites was imaged by using transmission electron microscopes (Tecnai G2 F20 S-TWIN, FEI). The absorption and emission spectra were recorded with a UV-vis spectrometer (UV-2600, Shimadzu) and a spectrofluorophotometer (CaryEclipse, Varian), respectively. All samples were excited at $\lambda_{ex} = 445$ nm, and the emission was collected at $\lambda_{em} > 400$ nm. The Fourier transform infrared spectroscopy (FT-IR) spectra were obtained using a FT-IR spectrometer (FTIR-8400s, Shimadzu). The X-ray diffraction (XRD) (XD8-AdranceX, Bruker Corporation, Germany) measurement was carried out using a Cu-Kα radiation source ($\lambda = 1.5418$ Å), and the 2θ range used was from 5° to 80°.

4. Results and Discussion

The synthesis routes of P3HT-COOH/CdSe nanocomposites are illustrated in Scheme 2. The P3HT-COOH (e.g., P3HT-M-COOH and P3HT-Z-COOH in Scheme 1) plays an important role in the synthesis of CdSe nanocrystals. The growth process of nanocrystals can be controlled via P3HT-COOH as a template. First of all, according to a recent report, the carboxyl of P3HT-COOH can react with Cd^{2+} to form P3HT-COO-Cd compounds linked by metal carboxylate linkage [39, 40]. The Se precursor was then injected and subjected to a subsequent nucleation-and-growth process.

FT-IR spectroscopy in Figures 1(a) and 1(b) was used to identify and characterize the metal carboxylate linkage between Cd^{2+} and -COOH. In Figure 1(a), the absorption peaks at 1639 cm^{-1} and 3433 cm^{-1} assigned to the characteristic C=O stretching vibration and -O-H stretching vibration of P3HT-Z-COOH disappeared in the FT-IR spectrum of P3HT-Z-COOH/CdSe nanocomposites, and the absorption peaks at 1556 cm^{-1} (carboxylate stretching) appeared, clearly indicating the success of chemical coupling (see Scheme 1) between CdSe and P3HT-Z-COOH. The same happens in Figure 1(b). Figure 1(c) compares the FT-IR spectra of P3HT-Z-COOH/CdSe nanocomposites and P3HT-M-COOH/CdSe nanocomposites. As shown in the FT-IR spectra, the -CH_2- characteristic vibration shifts from 1103 to 991 cm^{-1} due to the different locations of -CH_2- in the two kinds of P3HT-COOHs.

The high boiling point solvent ODE was employed to dissolve P3HT-COO-Cd (P3HT-Z-COO-Cd and P3HT-M-COO-Cd) for the synthesis of high-quality P3HT-COOH/CdSe NC nanocomposites. The injection of Se-

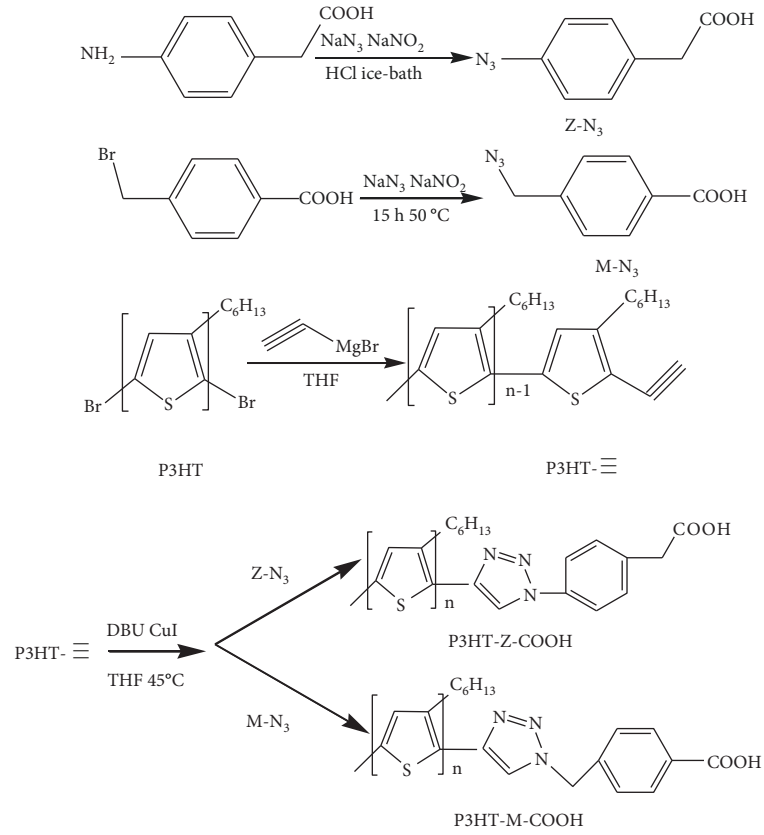

Scheme 1: Synthetic route to P3HT-COOHs by click reaction.

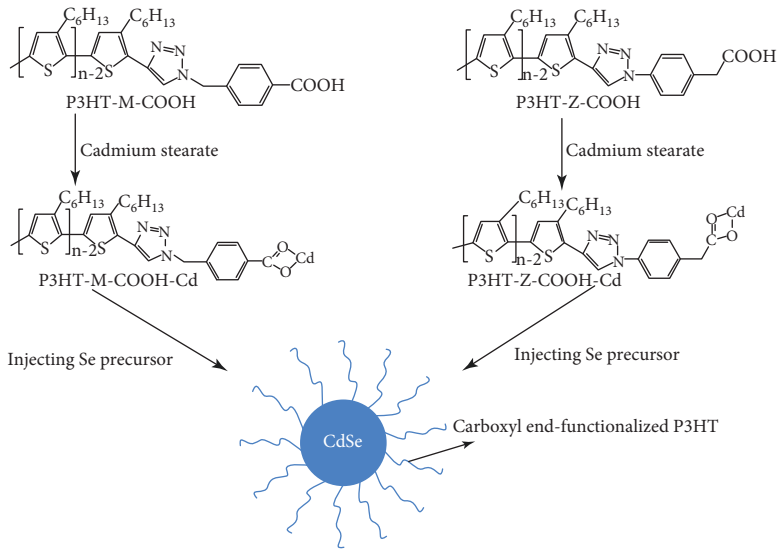

Scheme 2: Synthetic route to carboxyl end-functionalized P3HT/CdSe nanocomposites by P3HT-M-COOH (left panel) and P3HT-Z-COOH (right panel).

oleylamine solution initiated the nucleation and growth of CdSe NCs having direct contact with P3HT-COOH (see Experiment). The presence of P3HT-COOH imposed steric hindrance during the growth of CdSe NCs, thereby preventing the agglomeration of CdSe NCs.

As a result, despite the absence of hazardous organometallic ligands (e.g., widely used tri-n-octylphosphine oxide (TOPO) and trioctylphosphine (TOP) for high-quality CdSe QD synthesis), uniform CdSe QDs tethered with P3HT chains were obtained. It is clear that transmission electron

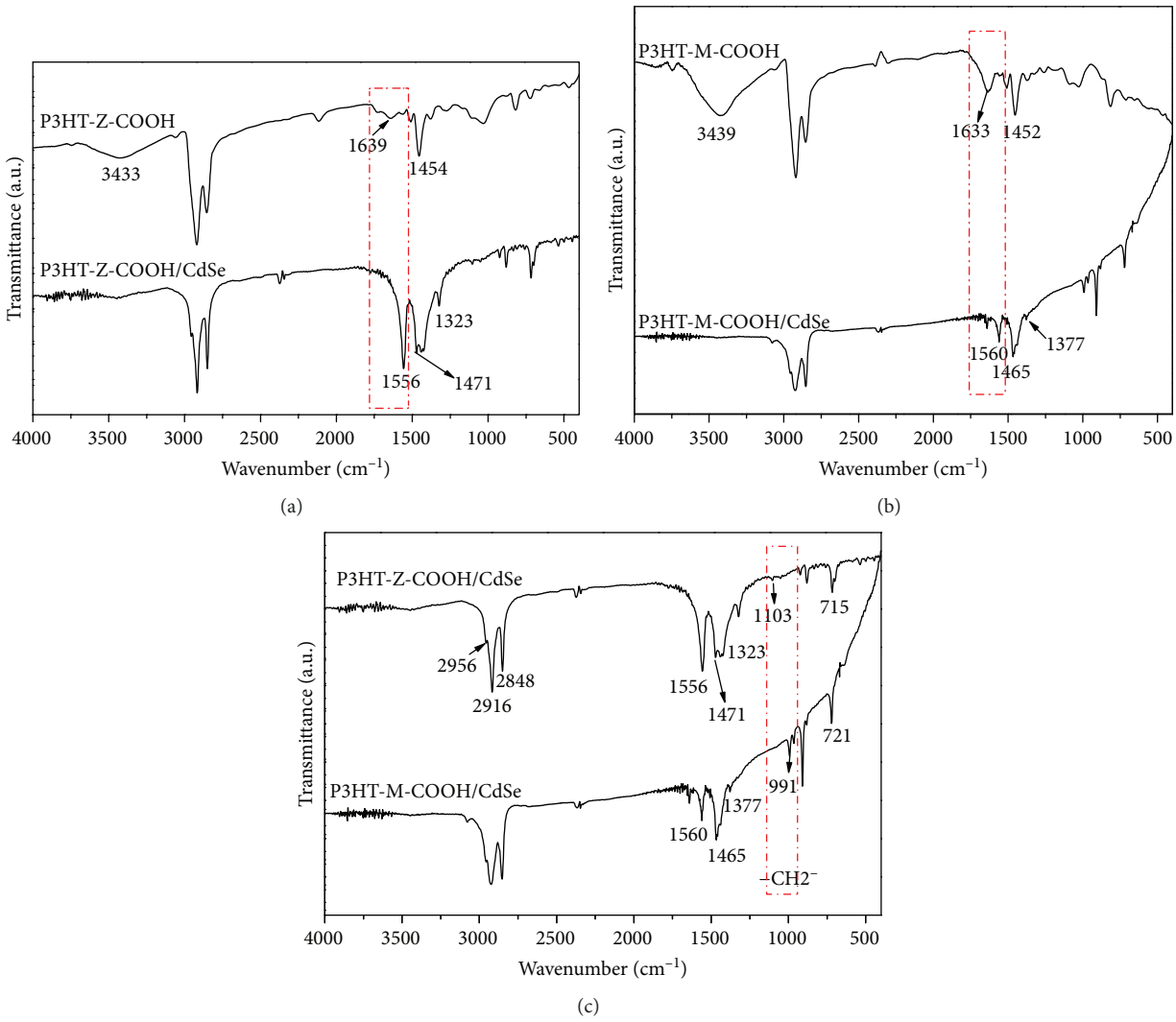

Figure 1: (a) FTIR spectrum of P3HT-Z-COOH and P3HT-Z-COOH/CdSe. (b) FTIR spectrum of P3HT-M-COOH and P3HT-M-COOH/CdSe. (c) FTIR spectra of P3HT-Z-COOH/CdSe nanocomposites and P3HT-M-COOH/CdSe nanocomposites.

microscopy (TEM) measurements revealed a homogeneous dispersion of P3HT-COOH/CdSe QD nanocomposites as shown in Figure 2. The diameters of these spherical CdSe nanocrystals increase to about 6.7 nm (P3HT-Z-COOH/CdSe) and 7.9 nm (P3HT-M-COOH/CdSe), respectively. It must be pointed out that the diameters of these spherical CdSe nanocrystals can be controlled by changing reaction conditions. In the same reaction time, the size of P3HT-M-COOH/CdSe NCs increased more obviously than P3HT-Z-COOH/CdSe NCs, revealing that P3HT-M-COOH is more effective for nucleation and growth of nanocrystals as the polymer matrix. It was found in TEM images that there is a narrow size distribution of the nanoparticles, and the shapes of these nanocrystals are regular, the dispersion of CdSe nanoparticles in P3HT-COOH is greatly improved, and the majority of the nanoparticles are spherical with an average grain size of 6 to 8 nm.

The photophysical properties of the resulting P3HT-COOH/CdSe nanocomposites were examined by UV-vis absorbance and photoluminescence (PL) studies. The absorption spectra of P3HT-COOH/CdSe nanocomposites are shown in Figure 3. As seen from Figure 3(a), the peak at 636 nm and 652 nm corresponds to P3HT-Z-COOH/CdSe and P3HT-M-COOH/CdSe absorption, respectively. The diameters of these spherical CdSe nanocrystals obtained by the calculation according to published equations [41] are consistent with the observation from TEM images. After the carboxyl functionalization, their optical properties both varied and the wavelength range of nanocomposites exhibited a red shift in comparison with the P3HT/CdSe nanocomposite [42]; it means that the size of the nanocomposites increased, indicating that carboxyl functionalization is sufficient for forming size-tunable P3HT-COOH/CdSe nanocomposites. In comparison with P3HT/CdSe nanocomposites [42], the size of P3HT-M-COOH/CdSe nanocomposites increased more obviously than that of P3HT-Z-COOH/CdSe NCs, which is in line with the TEM analysis.

The PL spectra of P3HT-Z-COOH/CdSe nanocomposites and P3HT-M-COOH/CdSe nanocomposites are shown in Figure 3(b). In contrast with P3HT-COOHs, nearly complete

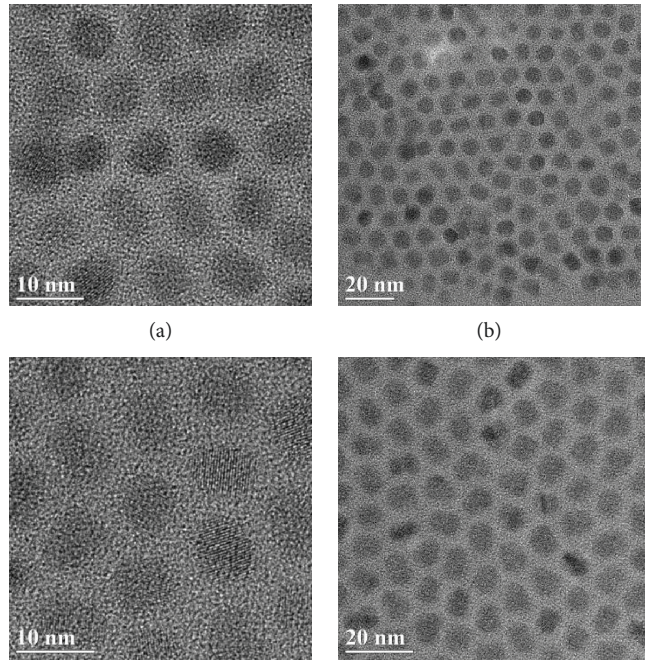

Figure 2: TEM images of P3HT-Z-COOH/CdSe nanocomposites (a, b) and P3HT-M-COOH/CdSe nanocomposites (c, d).

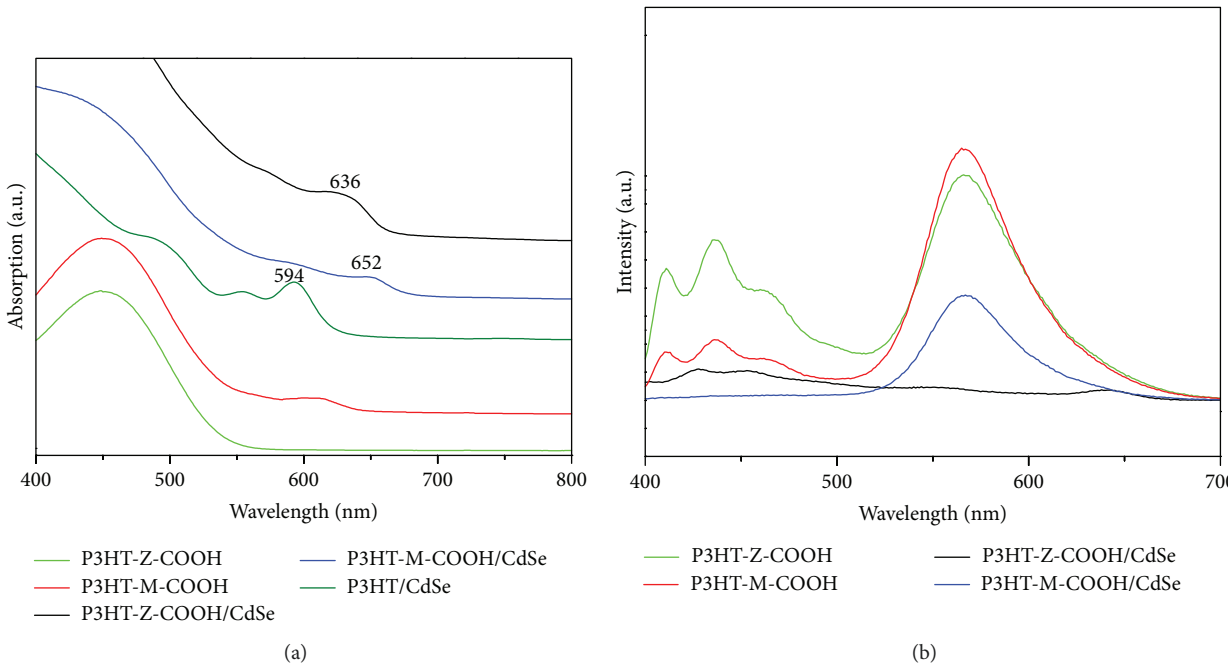

Figure 3: UV-vis spectra (a) and photoluminescence spectra (b) of P3HT-COOH/CdSe nanocomposites.

quenching of nanocomposite fluorescence was seen, implying efficient charge transfer from P3HT-COOHs to CdSe NCs. This observation further confirmed intimate chemical contact between P3HT-COOHs and CdSe NCs. It must be mentioned that the PL intensity of P3HT-M-COOH/CdSe nanocomposites is relatively higher. In contrast, nearly complete quenching of P3HT-Z-COOH/CdSe nanocomposite fluorescence was seen. One of the possible reasons for the different PL intensities could be attributed to different chemical structures of the two P3HT-COOHs. In P3HT-M-COOH, the carboxyl group is connected with phenyl. On the contrary, the carboxyl group is connected with methylene in P3HT-Z-COOH. Methylene has lower steric hindrance so that it can react with the CdSe NCs more easily. In

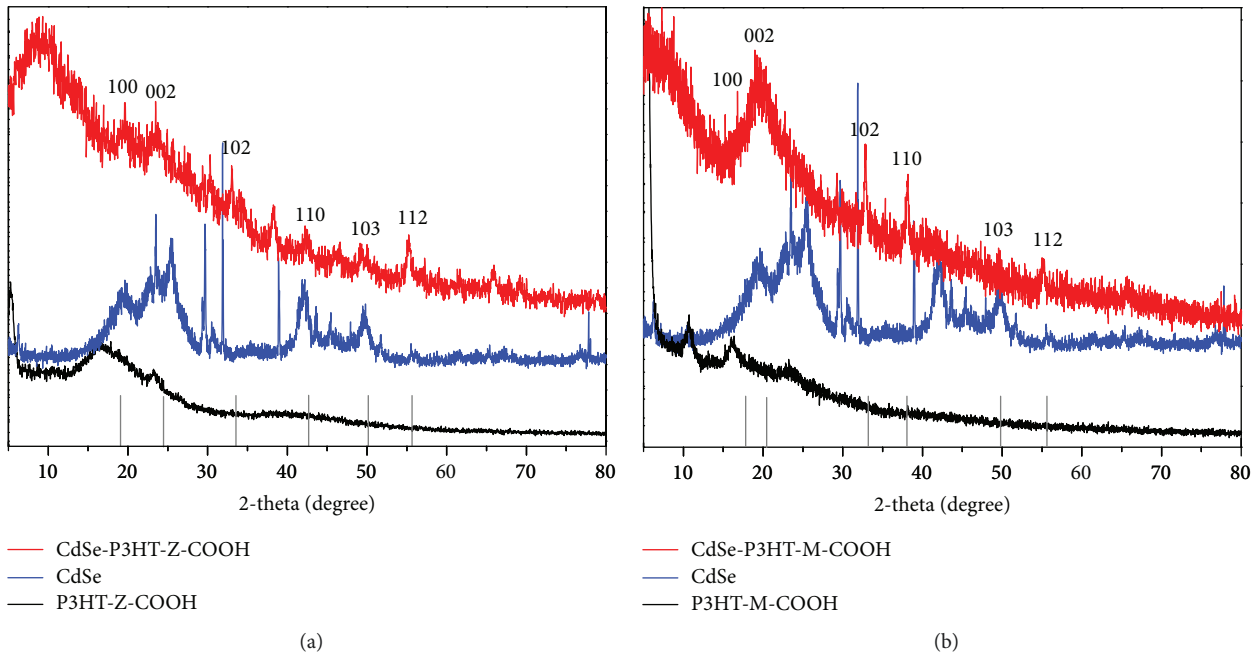

Figure 4: XRD patterns of P3HT-COOH/CdSe nanocomposites: (a) P3HT-Z-COOH/CdSe; (b) P3HT-M-COOH/CdSe.

comparison to the P3HT/CdSe nanocomposites [42], the significant PL quenching of nanocomposites after the carboxyl functionalization suggested the efficient charge transfer from P3HT-COOHs to CdSe NCs, which confirmed the intimate chemical contact between P3HT-COOH and CdSe QDs.

X-ray diffraction (XRD) analysis was performed to investigate the crystalline structure of P3HT-COOH/CdSe nanocomposites (Figure 4). In the XRD patterns of the carboxyl end-functionalized P3HT/CdSe nanoparticles, a series of characteristic peaks of (100), (002), (102), (110), (103), and (112) are observed, which are in accordance with the wurtzite phase of CdSe Qdots (JCPD No. 08-0456). Moreover, in TEM images, the lattice spacing of the spherical CdSe nanocrystals is 0.35 nm, corresponding to the (111) plane of cubic CdSe.

5. Conclusions

In summary, we demonstrated phosphine-free synthetic routes of P3HT-COOH/CdSe nanocomposites to achieve chemical tethering between the polymer matrix and the NC surface. P3HT-COOH can first react with Cd^{2+} to form P3HT-COOCd compounds linked by a metal carboxylate linkage. The precursor of Se was then injected and subjected to a subsequent nucleation-and-growth process. The scrutiny on the effects of P3HT-COOH/CdSe nanocomposites revealed that the carboxyl end-functionalized P3HTs were more effective in improving the characteristics of CdSe NCs than the pure P3HT and promoted CdSe NCs' effective charge transport and good dispersion of nanoparticles. In addition, the particle size of CdSe NCs was controllable. Therefore, this phosphine-free method provides a promising platform to craft a variety of functionalized polymer-nanocrystal nanocomposites.

Data Availability

The experimental data used to support the findings of this study are included within the article.

Conflicts of Interest

There are no conflicts to declare.

Acknowledgments

This work was supported by the Natural Science Foundation of Inner Mongolia (grant no. 2017MS0202).

References

[1] W. U. Huynh, J. J. Dittmer, and A. P. Alivisatos, "Hybrid Nanorod-Polymer Solar Cells," *Science*, vol. 295, no. 5564, pp. 2425–2427, 2002.

[2] S. H. Choi, H. Song, I. K. Park et al., "Synthesis of size-controlled CdSe quantum dots and characterization of CdSe–conjugated polymer blends for hybrid solar cells," *Journal of Photochemistry and Photobiology A: Chemistry*, vol. 179, no. 1-2, pp. 135–141, 2006.

[3] J. D. Olson, G. P. Gray, and S. A. Carter, "Optimizing hybrid photovoltaics through annealing and ligand choice," *Solar Energy Materials and Solar Cells*, vol. 93, no. 4, pp. 519–523, 2009.

[4] S. Dayal, N. Kopidakis, D. C. Olson, D. S. Ginley, and G. Rumbles, "Direct Synthesis of CdSe Nanoparticles in Poly(3-hexylthiophene)," *Journal of the American Chemical Society*, vol. 131, no. 49, pp. 17726-17727, 2009.

[5] R. Liu, "Hybrid Organic/Inorganic Nanocomposites for Photovoltaic Cells," *Materials*, vol. 7, no. 4, pp. 2747–2771, 2014.

[6] A. Smeets, K. Van den Bergh, J. De Winter, P. Gerbaux, T. Verbiest, and G. Koeckelberghs, "Incorporation of Different End Groups in Conjugated Polymers Using Functional Nickel Initiators," *Macromolecules*, vol. 42, no. 20, pp. 7638–7641, 2009.

[7] S. Ren, L. Y. Chang, S. K. Lim et al., "Inorganic–Organic Hybrid Solar Cell: Bridging Quantum Dots to Conjugated Polymer Nanowires," *Nano Letters*, vol. 11, no. 9, pp. 3998–4002, 2011.

[8] A. Smeets, P. Willot, J. De Winter, P. Gerbaux, T. Verbiest, and G. Koeckelberghs, "End Group-Functionalization and Synthesis of Block-Copolythiophenes by Modified Nickel Initiators," *Macromolecules*, vol. 44, no. 15, pp. 6017–6025, 2011.

[9] F. Alam, N. Kumar, and V. Dutta, "Study of surfactant-free lead sulfide nanocrystals-P3HT hybrid polymer solar cells," *Organic Electronics*, vol. 22, pp. 44–50, 2015.

[10] L. Li, M. J. Greaney, K. Li, A. Sachdeva, R. L. Brutchey, and J. C. Campbell, "Effects of surface ligands on energetic disorder and charge transport of P3HT:CdSe hybrid solar cells," *Physica Status Solidi B*, vol. 252, no. 6, pp. 1325–1333, 2015.

[11] D. Loubiri, Z. Ben Hamed, S. Ilahi, M. A. Sanhoury, F. Kouki, and N. Yacoubi, "Effect of TBPO-capped CdSe nanoparticles concentration on sub-bandgap absorption in poly(3-hexylthiophene) thin films studied by photothermal deflection spectroscopy," *Synthetic Metals*, vol. 206, pp. 1–7, 2015.

[12] J. Jung, Y. J. Yoon, M. He, and Z. Lin, "Organic-inorganic nanocomposites composed of conjugated polymers and semiconductor nanocrystals for photovoltaics," *Journal of Polymer Science Part B: Polymer Physics*, vol. 52, no. 24, pp. 1641–1660, 2014.

[13] G. Grancini, M. Biasiucci, R. Mastria et al., "Dynamic Microscopy Study of Ultrafast Charge Transfer in a Hybrid P3HT/Hyperbranched CdSe Nanoparticle Blend for Photovoltaics," *The Journal of Physical Chemistry Letters*, vol. 3, no. 4, pp. 517–523, 2012.

[14] L. Zhao and Z. Lin, "Crafting Semiconductor Organic–Inorganic Nanocomposites via Placing Conjugated Polymers in Intimate Contact with Nanocrystals for Hybrid Solar Cells," *Advanced Materials*, vol. 24, no. 32, pp. 4353–4368, 2012.

[15] W. M. Kochemba, D. L. Pickel, B. G. Sumpter, J. Chen, and S. M. Kilbey II, "In Situ Formation of Pyridyl-Functionalized Poly(3-hexylthiophene)s via Quenching of the Grignard Metathesis Polymerization: Toward Ligands for Semiconductor Quantum Dots," *Chemistry of Materials*, vol. 24, no. 22, pp. 4459–4467, 2012.

[16] H. Ma, H. Gao, Z. Zhou, W. Xu, and F. Ren, "Direct Synthesis of P3HT/CdS Nanocomposites With End-functionalized P3HT as the Template," *Polymers & Polymer Composites*, vol. 23, no. 7, pp. 435–442, 2015.

[17] N. V. Handa, A. V. Serrano, M. J. Robb, and C. J. Hawker, "Corrigendum: Exploring the synthesis and impact of end-functional poly(3-hexylthiophene)," *Journal of Polymer Science Part A: Polymer Chemistry*, vol. 53, no. 15, pp. 1841–1841, 2015.

[18] J. Liu, T. Tanaka, K. Sivula, A. P. Alivisatos, and J. M. J. Fréchet, "Employing End-Functional Polythiophene To Control the Morphology of Nanocrystal–Polymer Composites in Hybrid Solar Cells," *Journal of the American Chemical Society*, vol. 126, no. 21, pp. 6550-6551, 2004.

[19] M. Wright and A. Uddin, "Organic—inorganic hybrid solar cells: A comparative review," *Solar Energy Materials and Solar Cells*, vol. 107, pp. 87–111, 2012.

[20] R. A. Krüger, T. J. Gordon, T. Baumgartner, and T. C. Sutherland, "End-Group Functionalization of Poly(3-hexylthiophene) as an Efficient Route to Photosensitize Nanocrystalline TiO2 Films for Photovoltaic Applications," *ACS Applied Materials & Interfaces*, vol. 3, no. 6, pp. 2031–2041, 2011.

[21] F. Boon, A. Thomas, G. Clavel et al., "Synthesis and characterization of carboxystyryl end-functionalized poly(3-hexylthiophene)/TiO2 hybrids in view of photovoltaic applications," *Synthetic Metals*, vol. 162, no. 17-18, pp. 1615–1622, 2012.

[22] H. Nakashima, K. Furukawa, K. Ajito, Y. Kashimura, and K. Torimitsu, "Selective Chemisorption of End-Functionalized Conjugated Polymer on Macro- and Nanoscale Surfaces," *Langmuir*, vol. 21, no. 2, pp. 511–515, 2005.

[23] H.-C. Liao, S.-Y. Chen, and D.-M. Liu, "In-Situ Growing CdS Single-Crystal Nanorods via P3HT Polymer as a Soft Template for Enhancing Photovoltaic Performance," *Macromolecules*, vol. 42, no. 17, pp. 6558–6563, 2009.

[24] V. Kazukauskas, E. Couderc, A. Sakavicius et al., "Analysis of carrier transport in photovoltaic structures of P3HT with CdSe nanocrystals," *Applied Surface Science*, vol. 334, pp. 169–173, 2015.

[25] S. Dayal, H. Z. Zhong, N. Kopidakis, G. D. Scholes, and G. Rumbles, "Improved power conversion efficiency for bulk heterojunction solar cells incorporating CdTe-CdSe nanoheterostructure acceptors and a conjugated polymer donor," *Journal of Photonics for Energy*, vol. 5, no. 1, p. 057409, 2015.

[26] F. A. Roghabadi, M. Kokabi, V. Ahmadi, and G. Abaeiani, "Structure optimization of P3HT:CdSe hybrid solar cell using optical analysis and electrochemical impedance spectroscopy," *Thin Solid Films*, vol. 621, pp. 19–25, 2017.

[27] J. Lee, J. Lee, J. Yang, T. Park, S. J. Ahn, and W. Yi, "Polymer Quantum Dot-Sensitized Solar Cell Incorporating Single-Walled Carbon Nanotubes," *Journal of Nanoscience and Nanotechnology*, vol. 17, no. 8, pp. 5496–5500, 2017.

[28] J. Jung, Y. J. Yoon, and Z. Lin, "Intimate organic–inorganic nanocomposites via rationally designed conjugated polymer-grafted precursors," *Nanoscale*, vol. 8, no. 36, pp. 16520–16527, 2016.

[29] S. M. Jin, I. Kim, J. A. Lim, H. Ahn, and E. Lee, "Interfacial Crystallization-Driven Assembly of Conjugated Polymers/-Quantum Dots into Coaxial Hybrid Nanowires: Elucidation of Conjugated Polymer Arrangements by Electron Tomography," *Advanced Functional Materials*, vol. 26, no. 19, pp. 3226–3235, 2016.

[30] S. Bera and S. K. Ray, "The Role of Nanocrystal Size in Solution Processable CdSe:P3HT Hybrid Photovoltaic Devices," *Journal of Nanoscience and Nanotechnology*, vol. 16, no. 5, pp. 4840–4845, 2016.

[31] A. Benchaabane, Z. Ben Hamed, A. Lahmar et al., "Optical properties of P3HT:tributylphosphine oxide-capped CdSe nanocomposites," *Applied Physics A*, vol. 122, no. 8, pp. 720–724, 2016.

[32] S. Sapra, A. L. Rogach, and J. Feldmann, "Phosphine-free synthesis of monodisperse CdSe nanocrystals in olive oil," *Journal of Materials Chemistry*, vol. 16, no. 33, pp. 3391–3395, 2006.

[33] J. Jasieniak, C. Bullen, J. van Embden, and P. Mulvaney, "Phosphine-Free Synthesis of CdSe Nanocrystals," *The Journal of Physical Chemistry B*, vol. 109, no. 44, pp. 20665–20668, 2005.

[34] S. Asokan, K. M. Krueger, A. Alkhawaldeh et al., "The use of heat transfer fluids in the synthesis of high-quality CdSe

quantum dots, core/shell quantum dots, and quantum rods," *Nanotechnology*, vol. 16, no. 10, pp. 2000–2011, 2005.

[35] M. Sun and X. Yang, "Phosphine-Free Synthesis of High-Quality CdSe Nanocrystals in Noncoordination Solvents: "Activating Agent" and "Nucleating Agent" Controlled Nucleation and Growth," *Journal of Physical Chemistry C*, vol. 113, no. 20, pp. 8701–8709, 2009.

[36] L. J. Zhang, X. C. Shen, and H. Liang, "A Mild Phosphine-Free Synthesis of Alkylamine-Capped CdSe Nanocrystals," *Journal of Nanoscience and Nanotechnology*, vol. 10, no. 8, pp. 4979–4984, 2010.

[37] F. Monnaie, W. Brullot, T. Verbiest et al., "Synthesis of End-Group Functionalized P3HT: General Protocol for P3HT/Nanoparticle Hybrids," *Macromolecules*, vol. 46, no. 21, pp. 8500–8508, 2013.

[38] M. Urien, H. Erothu, E. Cloutet, R. C. Hiorns, L. Vignau, and H. Cramail, "Poly(3-hexylthiophene) Based Block Copolymers Prepared by "Click" Chemistry," *Macromolecules*, vol. 41, no. 19, pp. 7033–7040, 2008.

[39] P. E. Chen, N. C. Anderson, Z. M. Norman, and J. S. Owen, "Tight Binding of Carboxylate, Phosphonate, and Carbamate Anions to Stoichiometric CdSe Nanocrystals," *Journal of the American Chemical Society*, vol. 139, no. 8, pp. 3227–3236, 2017.

[40] N. C. Anderson, M. P. Hendricks, J. J. Choi, and J. S. Owen, "Ligand Exchange and the Stoichiometry of Metal Chalcogenide Nanocrystals: Spectroscopic Observation of Facile Metal-Carboxylate Displacement and Binding," *Journal of the American Chemical Society*, vol. 135, no. 49, pp. 18536–18548, 2013.

[41] W. W. Yu, L. Qu, W. Guo, and X. Peng, "Experimental Determination of the Extinction Coefficient of CdTe, CdSe, and CdS Nanocrystals," *Chemistry of Materials*, vol. 15, no. 14, pp. 2854–2860, 2003.

[42] F. F. Chang, *Preparation and performance of nanocomposites based on CdE nanocrastals and P3HT derivatives. (Master's degree)*, Inner Mongolia University of technology, Hohhot, China, 2015.

Hindawi
Journal of Nanomaterials
Volume 2019, Article ID 3959037, 13 pages
https://doi.org/10.1155/2019/3959037

Research Article

PEGylation of Ginsenoside Rg3-Entrapped Bovine Serum Albumin Nanoparticles: Preparation, Characterization, and In Vitro Biological Studies

Lijun Zhang,[1,2,3] Junfeng Hui,[1,2,3] Pei Ma,[1,2,3] Yu Mi,[1,2,3] Daidi Fan,[1,2,3] Chenhui Zhu,[1,2,3] Lei Chi,[1,2,3] and Yanan Dong[1,2,3]

[1]*Shaanxi Key Laboratory of Degradable Biomedical Materials, School of Chemical Engineering, Northwest University, 229 North Taibai Road, Xi' an, Shaanxi 710069, China*
[2]*Shaanxi R&D Center of Biomaterials and Fermentation Engineering, School of Chemical Engineering, Northwest University, 229 North Taibai Road, Xi' an, Shaanxi 710069, China*
[3]*Biotech & Biomed Research Institute, Northwest University, 229 North Road Taibai, Xi' an, Shaanxi 710069, China*

Correspondence should be addressed to Yu Mi; mi_yu@nwu.edu.cn and Daidi Fan; fandaidi@nwu.edu.cn

Received 10 October 2018; Revised 11 December 2018; Accepted 2 January 2019; Published 27 March 2019

Guest Editor: Kakarla R. Reddy

Ginsenoside Rg3 (Rg3) is one of three triterpene saponins from red ginseng. It has important structural functions and pharmacological properties. However, due to its poor solubility, low bioavailability, and short half-life in blood circulation, its clinical application was unsuccessful for the treatment of a variety of cancers. In order to overcome this limitation, this study prepared mPEGylation-Rg3 bovine serum albumin nanoparticles (mPEG-Rg3-BSA NPs). The characteristics of the NPs, such as drug entrapment efficiency, drug loading efficiency, surface morphology, thermal stability, and cytotoxicity in vitro, were investigated. The results showed that the appropriate particle size of the obtained NPs was 149.5 nm, the water solubility and stability were better than free Rg3, and the drug entrapment efficiency and drug loading efficiency were 76.56% and 17.65%, respectively. Moreover, the cytotoxicity assays of the mPEG-Rg3-BSA NPs and free Rg3 revealed that the mPEG-Rg3-BSA NPs have greater anticancer effects in HepG2 cells and A549 cells. However, the cytotoxic effect of free Rg3 was higher than the mPEG-Rg3-BSA NPs in L929 cells. The results indicated that using the mPEGylation method and selecting BSA as a carrier to form the nanodrug carrier system were effective for improving the properties of Rg3.

1. Introduction

Cancer is a serious threat to human health and life and causes a high death rate [1]; there are various drugs available to cure cancer. However, their major drawbacks are poor distribution, poor water solubility, poor target specificity, and a short half-life in blood circulation, which reduces the therapeutic effect to a large extent. Therefore, clinical applications are unsuccessful for the treatment of a variety of cancers [2]. Ginsenoside is a sterol compound with three terpene saponins. It is mainly extracted from ginseng medicinal materials, including protopanaxadiols (Ppd) and protopanaxatriols (Ppt), which have many medicinal properties, such as anti-inflammatory, anticancer, and antioxidant effects [3]. 20(R)-Rg3 (Rg3) is one of the major Ppd types with no toxicity and has hydrophobic triterpenes, steroid aglycones, and hydrophilic sugar side chains in its structure. Recent studies showed that Rg3 is a powerful anticancer drug for the treatment of a variety of cancers [4]. It can inhibit the proliferation of tumor cells and induce the apoptosis of tumor cells. Moreover, it can prevent tumor cell adhesion, invasion, and metastasis and it can regulate the proliferation of tumor cells. Although Rg3 possesses a variety of medically beneficial effects, the clinical application of Rg3 is restricted due to its poor water solubility and short circulation half-life and bad target specificity into tumor tissues [5]. Furthermore, low aqueous solubility limits its bioavailability, thereby not distinguishing healthy from cancerous tissues [6]. It

requires polyethylene glycol (PEG) 400 or polyethoxylated castor oil and ethanol as a vehicle. These agents cause severe allergic reactions upon intravenous administration [7]. Polyethylene glycol modification is considered an ideal potential method for the delivery of poorly water-soluble drugs. Currently, it is one of the common techniques by which we can use it or its derivatives to improve the molecular structure of drugs. As a water-soluble restorative agent with the properties of nontoxicity and low immunity, it can increase the circulation half-life and colloidal stability under physiological salt concentrations [8, 9]. A number of small-molecule drugs, such as paclitaxel, camptothecin, and doxorubicin hydrochloride, have been modified by PEG or its derivatives [10, 11], and their solubility has been improved greatly. Therefore, we selected methoxy polyethylene glycol succinic acid (mPEG-SA) as a water-soluble restorative agent to enhance the water solubility of Rg3.

In recent years, great progress has been made in nanodrug delivery systems, which has been reported to accumulate drugs in tumor tissues more efficiently due to the enhanced permeability retention effect (EPR). They are designed to deliver poorly water-soluble drugs and improve the pharmacological and therapeutic properties of drugs administered parenterally. Moreover, the hydrophilicity of nanoparticles provides excellent water solubility and superior biocompatibility, because they effectively protect the activity of drugs, achieve slow and controlled release, and avoid reticuloendothelial system (RES) phagocytosis [12–14]. Thus far, many types of nanocarriers have been invented by researchers, such as lipid- or polymer-based nanoparticles, nanofibres, and biodegradable carrier systems [15–17]. As a common and natural biomacromolecule protein, studies show that BSA [18–20] has its own unique advantages with respect to drug delivery. Among them, BSA has been widely employed as a biomacromolecule nanocarrier for improving the therapeutic efficacy of anticancer drugs, which has important physiological functions in the body and regulates the total osmotic pressure of the blood. Furthermore, it has many advantages, such as being safe and nontoxic, with low immunogenicity, biodegradability, and good biocompatibility, and it is an abundant endogenous protein in human serum. Moreover, BSA NPs were prepared using the desolvation method followed by glutaraldehyde fixation [21]. Collectively, BSA can be considered a safe, effective, and biocompatible target carrier to deliver mPEG-Rg3 to form a nanodrug delivery system.

Briefly, this paper used mPEG-SA and BSA to improve the properties of Rg3, which were expected to enhance the aqueous solubility and exert anticancer effects by potent delivery of Rg3 with passive target specificity to tumor cells. As shown in Figure 1, Rg3 was modified by mPEG-SA to synthesize mPEG-Rg3, and then, mPEG-Rg3 was entrapped within the BSA to form mPEG-Rg3-BSA NPs using the desolvation method. The mPEG-Rg3-BSA nanostructure had characteristics of excellent stability, high anticancer effects, and slow release. Furthermore, the physicochemical and biochemical properties of mPEG-Rg3-BSA NPs were measured by dynamic light scattering (DLS), scanning electron microscopy (SEM), transmission electron microscopy (TEM), thermogravimetry (TG), and differential scanning calorimetry (DSC). The cellular uptake of mPEG-Rg3-BSA NPs was visualized using confocal laser scanning microscopy (CLSM), whereas the cytotoxicity of mPEG-Rg3-BSA NPs was evaluated by MTT assay, apoptosis was observed by chromatin staining with Hoechst 33342, and the in vivo biodistribution behavior was investigated by near-infrared imaging system.

2. Materials and Methods

2.1. Materials. BSA was obtained from AMRESCO (Solon, OH, USA). Ginsenoside Rg3 was purchased from Sigma-Aldrich (Shanghai, China). Methoxy polyethylene glycol succinic acid (mPEG-SA) was purchased from Hua Teng Pharma. Co. Ltd. (Hunan, China). Dicyclohexylcarbodiimide (DCC), Dimethylaminopyridine (DMAP). and N,N-Dimethylformamide (DMF) were purchased from Tianjin KGM Chemical Reagent Co. Ltd. (Tianjin, China). Ultrapure water used in all experiments was produced with a Milli-Q synthesis system (Millipore Corp., Billerica, MA, USA). Fluorescein isothiocyanate (FITC) was purchased from Sigma (USA), and Gibco Dulbecco's modified Eagle's medium (DMEM) was obtained from HyClone (LA, USA). Foetal bovine serum (FBS) was supplied by Gibco (NY, USA). Penicillin, streptomycin, and methyl thiazolyl tetrazolium kit (MTT) were supplied by KeyGEN Biological Technology Development Co. Ltd. (Nanjing, China). Hoechst 33342 fluorescent dye was obtained from Beyotime Biotechnology (Shanghai, China). DiR was purchased from Biotium Inc. (USA). The human hepatoma carcinoma cells (HepG2 cells) and human lung carcinoma cells (A549 cells) were obtained from the American Type Culture Collection (ATCC) (Manassas, VA, USA). All other regents were of analytical grade.

2.2. Synthesis of mPEG-Rg3. mPEG-Rg3 was prepared by esterification [11]. As shown in Figure 2(a), mPEG-SA (190 mg, 0.095 mmoL) was activated by DMAP (3.863 mg, 0.317 mmoL) and DCC (19.58 mg, 0.095 mmoL) in a solution (4 mL DMF and 1 mL CH_2Cl_2) after the solution was stirred for 0.5 h at room temperature. Then, Rg3 (25 mg, 0.032 mmoL) was added to the mixture. When the solution was stirred for 72 h at room temperature, the prepared compounds were extracted three times using ultrapure water and dichloromethane and then evaporated in vacuo. At the same time, it was further purified on a silica gel column, after which the products were dialyzed for 72 h against purified water. The mPEG-Rg3 was obtained by freeze drying. Then, the structure of mPEG-Rg3 was confirmed by ^{13}C NMR (Japan Electron Optics Laboratory Co. Ltd., Japan) and FT-IR (Brook Spectrometer Co. Ltd., USA).

2.3. Preparation of mPEG-Rg3-BSA NPs. The mPEG-Rg3-BSA NPs were prepared using a desolvation technique [22–24]. As shown in Figure 2(b), BSA (2 mL, 10 mg/mL) was first dissolved in ultrapure water; then, NaOH solution (30 μL, 0.02 mg/mL) was slowly added to the BSA solution. The mPEG-Rg3 (6 mL, 0.76 mg/mL) was dissolved in absolute ethyl alcohol and later added slowly to the BSA solution.

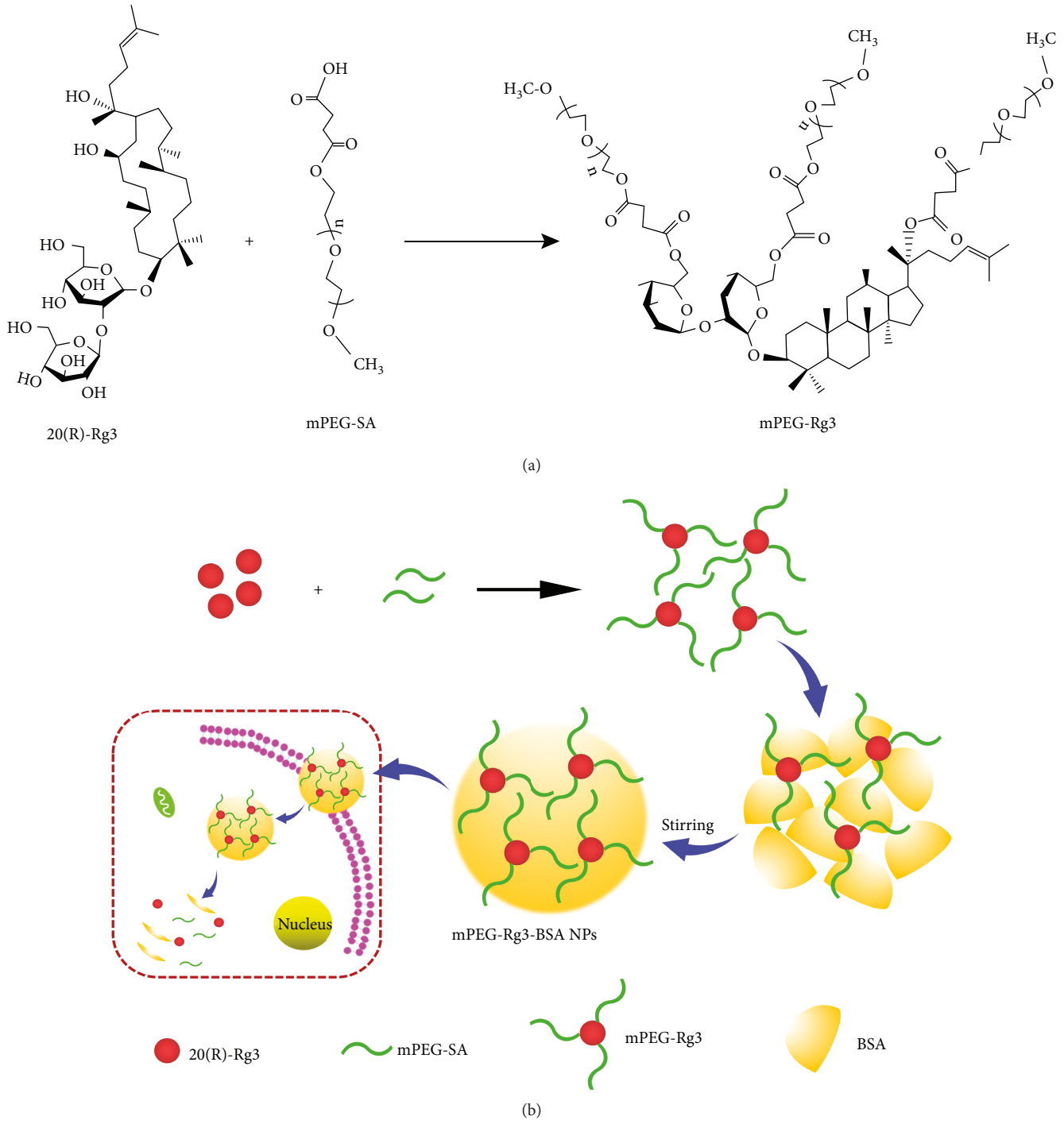

Figure 1: Schematic illustration of the synthesis of mPEG-Rg3 (a) and mPEG-Rg3-BSA NPs (b).

After the reaction mixture was stirred at 500 rpm for 24 h at room temperature, this reconstitution solution was centrifuged (18000 × g, 15 min) to separate the unloaded Rg3. This purification process was repeated six times using ultrapure water. After each centrifugation, the residue was redispersed to the original volume with deionized water using a mechanical stirrer. Then, the resulting solution was freeze dried after a final redispersion to achieve mPEG-Rg3-BSA NPs. Furthermore, the supernatants from each centrifugation were pooled to determine the drug loading capacities (DLC) and encapsulation efficiency (EE).

2.4. Characterization of mPEG-Rg3-BSA NPs. The characterization of mPEG-Rg3-BSA NPs was confirmed by FT-IR. The mPEG-Rg3-BSA NP suspension was diluted with water, and the average size and distribution of mPEG-Rg3-BSA NPs were determined by DLS (Malvern Instruments Ltd., UK) at room temperature. The size and morphology of the nanoparticles

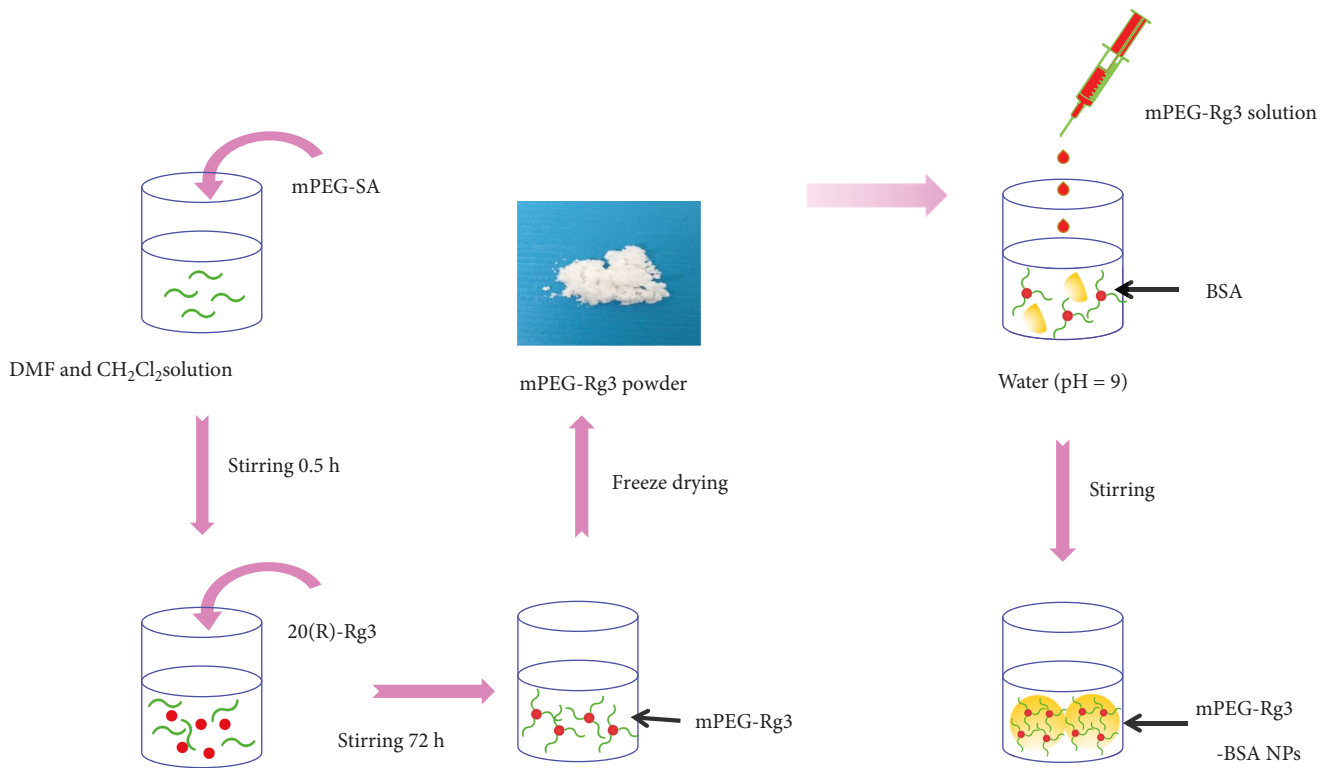

Figure 2: Synthetic route for the preparation of mPEG-Rg3 (a) and mPEG-Rg3-Rg3 NPs (b).

were observed using SEM (Hitachi Ltd., Japan) and TEM (Hitachi Ltd., Japan). For SEM, the mPEG-Rg3-BSA NP powder was placed on a conductive tape and the excess powder was removed with tweezers. Because of the poor conductivity of the sample, gold plating was needed. After an interval, the mPEG-Rg3-BSA NP powder was deposited on the sample plate by SEM. For TEM, the proper amount of mPEG-Rg3-BSA NP suspension was absorbed and the suspension was first removed to a special copper screen. It was incubated for five minutes, and filter paper was used to dry the redundant suspension in the copper screen. For negative staining with 3% phosphotungstic acid solution, the suspension was stained for 3 min. After staining, the morphology and size of the mPEG-Rg3-BSA NPs were investigated by TEM.

The supernatant from each centrifugation was collected to determine the drug entrapment efficiency and drug loading efficiency, which was analyzed for residual drug concentration using high-performance liquid chromatography (HPLC) (Rg3: 203 nm; specific volume ratio mixture of acetonitrile-water as a mobile phase; flow rate at 1.5 mL·min^{-1}) [25, 26]. DLC and EE were calculated according to the following equations:

$$\begin{aligned} \mathrm{DLC}(\%) &= \left(\frac{\text{weight of loaded drug}}{\text{weight of nanoparticles}}\right) \times 100\%, \\ \mathrm{EE}(\%) &= \left(\frac{\text{weight of loaded drug}}{\text{weight of drug of Rg3}}\right) \times 100\%. \end{aligned} \quad (1)$$

The thermal properties of Rg3, mPEG-Rg3, BSA, and mPEG-Rg3-BSA NPs were investigated using TG and DSC (Shimadzu, Kyoto, Japan). For TG, the samples were set from 50°C to 750°C at a ramping rate of 10°C·min^{-1}; 20 mg of each sample was placed in a standard aluminum pan. For DSC, the samples were set from 30°C to 550°C at a ramping rate of 10°C·min^{-1}; 20 mg of each sample was placed in a standard aluminum pan.

For the time-dependent stability studies, the sizes and zeta potentials were measured by evaluating the time dependency of mPEG-Rg3-BSA NPs at regular time intervals. Moreover, the mPEG-Rg3-BSA NPs were studied for up to 18 days at 4°C [27].

The release of drugs from the NPs was analyzed using a dialysis method [28]. The mPEG-Rg3-BSA NP suspension was first loaded into a dialysis bag (MWCO 3500). Then, the dialysis bag was immersed in 80 mL of PBS (pH = 7.4) and placed in a shaking bath (37°C, 100 rpm). An aliquot (2 mL) of the medium was collected at timed intervals, and the Rg3 concentration in the buffer was determined using HPLC. The amount released was then calculated. Each profile represents the average of three independent runs with the same sampling schedules, and the standard deviation of each point was typically 5% or less.

2.5. Haemolysis Assay. Haemolysis experiments were conducted to evaluate the biocompatibility of free Rg3 and mPEG-Rg3-BSA NPs according to the general procedure of the haemolysis test. Five millilitres of fresh blood samples was collected from rabbits and then added to blood collection tubes immediately to prevent coagulation. One millilitre of fresh blood samples from the blood collection tube was placed into 1.25 mL normal saline, and the different

concentrations free Rg3 and mPEG-Rg3-BSA NP suspension (5 mL) were dispersed in 100 μL aliquots. At the same time, normal saline and distilled water were dispersed in 100 μL aliquots as negative and positive controls. Then, samples were incubated under constant shaking for 1 h at 37°C. The red blood cells (RBCs) were collected by centrifugation at 1500 rpm for 5 min at 4°C. After centrifugation at 1500 rpm for 5 min at 4°C, the supernatant (100 μL, 96-well plates) was analyzed for haemoglobin release at 545 nm using a microplate spectrophotometer (Tecan, Switzerland) [29]. Haemolysis was determined from three independent experiments. The haemolytic ratio (HR) was calculated according to the following equation:

$$\mathrm{HR}\% = \frac{A_{\text{sample}} - A_{\text{negative control}}}{A_{\text{positive control}} - A_{\text{negative control}}} \times 100\%. \quad (2)$$

2.6. In Vitro Cell Cytotoxicity and Cellular Uptake. The MTT assay was used to evaluate the cell inhibition of different samples [30, 31]. Briefly, L929 cells and HepG2 cells and A549 cells were seeded in 96-well plates at a density of 1×10^4 per well in 100 μL culture medium and incubated for 24 h. Then, the cells were treated with samples at 37°C in a humidified incubator with 5% CO_2 for 24 h. The free Rg3 and mPEG-Rg3-BSA NPs (60, 120, 180, 240, and 300 μM) were dissolved in dimethyl sulfoxide and diluted in culture medium before the assay. A total of 50 μL of MTT solution was added to each well and incubated for 2 h at 37°C. Then, the supernatants were removed and added to 150 μL of DMSO. The absorbance at 490 nm was then read with a microplate reader (BioTek Instruments Inc., USA). The data were representative of three independent experiments.

Cellular uptake and distribution of Rg3 from the NPs were observed by CLSM (Leica, Germany) [32]. First, mPEG-Rg3-BSA NPs (180 μM) were labelled with FITC to investigate the uptake of NPs into L929 and HepG2 cells according to the method of Leamon and Low (1991). After the L929 and HepG2 cells achieved 70–80% confluency, the cells were trypsinized and seeded onto culture slides at a density of 7×10^5 cells per well (surface area of 10 cm^2 per well) and incubated for 24 h at 37°C. FITC-labelled mPEG-Rg3-BSA NPs were added and incubated for 4 h. After incubation, all reagents were removed. Cells were washed with PBS (pH = 7.4) at least 3 times for 2 minutes each and fixed with paraformaldehyde for 10 min. After the cells were washed with PBS, the nuclei were counterstained with DAPI for 5 min. Finally, the cell monolayer was washed three times with PBS and observed by CLSM.

2.7. Apoptosis Assay. Apoptosis was observed by chromatin staining with Hoechst 33342. HepG2 cells were seeded in 96-wells and incubated for 24 h at 37°C. The mPEG-Rg3-BSA NPs and free Rg3 (180, 240, and 300 μM) were added and incubated for 24 h. After incubation, all reagents were removed. Cells were washed with RPMI 1640 cell culture medium at least 2 times for 2 minutes each. Then, Hoechst 33342 (100 μL) was added in the dark. When cells were incubated for 15 min, they were washed with PBS at least 3 times. The nuclear morphology changes were observed under a fluorescence microscope (Nikon, Tokyo, Japan) [33].

2.8. Biodistribution of DiR-Loaded mPEG-Rg3-BSA NPs in Tumor-Bearing Mice. To study the biodistribution of the mPEG-Rg3-BSA NPs in tumor-bearing mice [34], the mPEG-Rg3-BSA NPs were labelled with DiR using the same protocol for the preparation of the mPEG-Rg3-BSA NPs. When the subcutaneous HepG2 tumors grew up to 300~400 mm^3, mice were injected with free DiR and DiR-labelled mPEG-Rg3-BSA NPs at a dose of 0.5 mg/kg. Fluorescent images were taken at different intervals (2, 8, and 24 h) using the vivo imaging system (IVIS® Lumina XR Series III, PerkinElmer). Then, the HepG2 tumor-bearing mice were dissected at 24 h for imaging.

2.9. Statistical Analysis. All data are given as the mean values ± standard deviation (SD). A p value of 0.05 or less was considered to be statistically significant.

3. Results and Discussion

3.1. ^{13}C NMR and FT-IR of mPEG-Rg3-BSA NPs. The mPEG-Rg3 powder was obtained by freeze drying, and the water solubility of Rg3 was 1 mg/mL after being conjugated with mPEG-SA, and the yield was 48.5%. As shown in Figure 3(a), a characteristic succinic acid peak of mPEG-SA was present at 174.48 ppm. For the next step, mPEG-SA was conjugated to Rg3 via the formation of ester bonds. As expected, the ^{13}C NMR spectrum of the mPEG-Rg3 conjugate contains all expected resonance peak characteristics of mPEG-SA and Rg3 and the carbon double bonds of mPEG-Rg3 were at 124.12 ppm and 129.90 ppm. The extent of mPEG-SA conjugation was calculated based on the ester bonds of mPEG-Rg3 at 172.18 ppm and 169.38 ppm. From the ^{13}C NMR results, we determined that the C-20 hydroxyl and C-6 sugar hydroxyl groups of Rg3 underwent ester bonding [33].

As shown in Figure 3(b), the mPEG-Rg3 contained the characteristic peak ($\nu_{C=C}$) of Rg3 at 1647 cm^{-1} and the wavelength $C = O$ was at 1734 cm^{-1}. From the FT-IR, Rg3 may react with the carboxylic group of mPEG-SA. Moreover, this conclusion tested the results of Figure 3(a). At the same time, the FT-IR results demonstrated that the characteristic peak of carbon oxygen bonds (ν_{C-O}, 1075 cm^{-1}) for mPEG-Rg3 appeared for mPEG-Rg3-BSA NPs, which was possible because the hydroxyl of Rg3 interacted with the aromatic residues (tryptophan, tyrosine) of BSA [34], and Rg3 was encapsulated into the core of the NPs.

3.2. Size and Morphology of mPEG-Rg3-BSA NPs. The desolvation technique [35], which is classic, simple, and easy to operate, was used to prepare the mPEG-Rg3-BSA NPs. The results demonstrated that the ratio of solvent and the pH of the BSA solution were important to avoid coalescence and agglomeration during desolvation. For the pH of the BSA solution, changes in pH can lead to denaturation and had an effect on the charge of the raw materials, as lower pH values (such as pH 7 or 8) would lead to precipitation and higher pH values (pH = 10) would increase the size of the

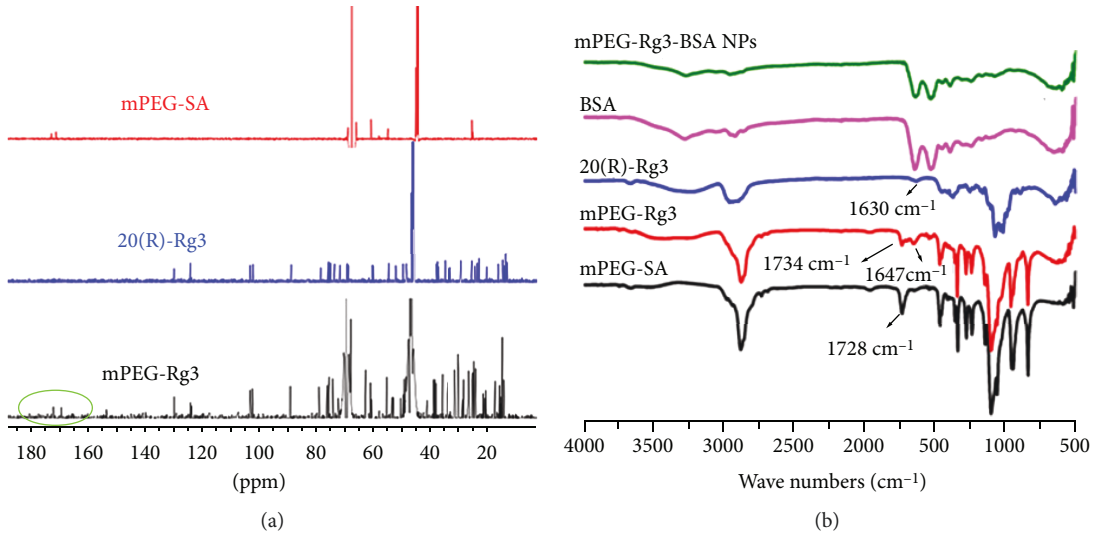

FIGURE 3: (a) The ^{13}C NMR spectrum of mPEG-Rg3, 20(R)-Rg3, and mPEG-SA. (b) The FT-IR spectra of mPEG-SA, mPEG-Rg3, 20(R)-Rg3, BSA, and mPEG-Rg3-BSA NPs.

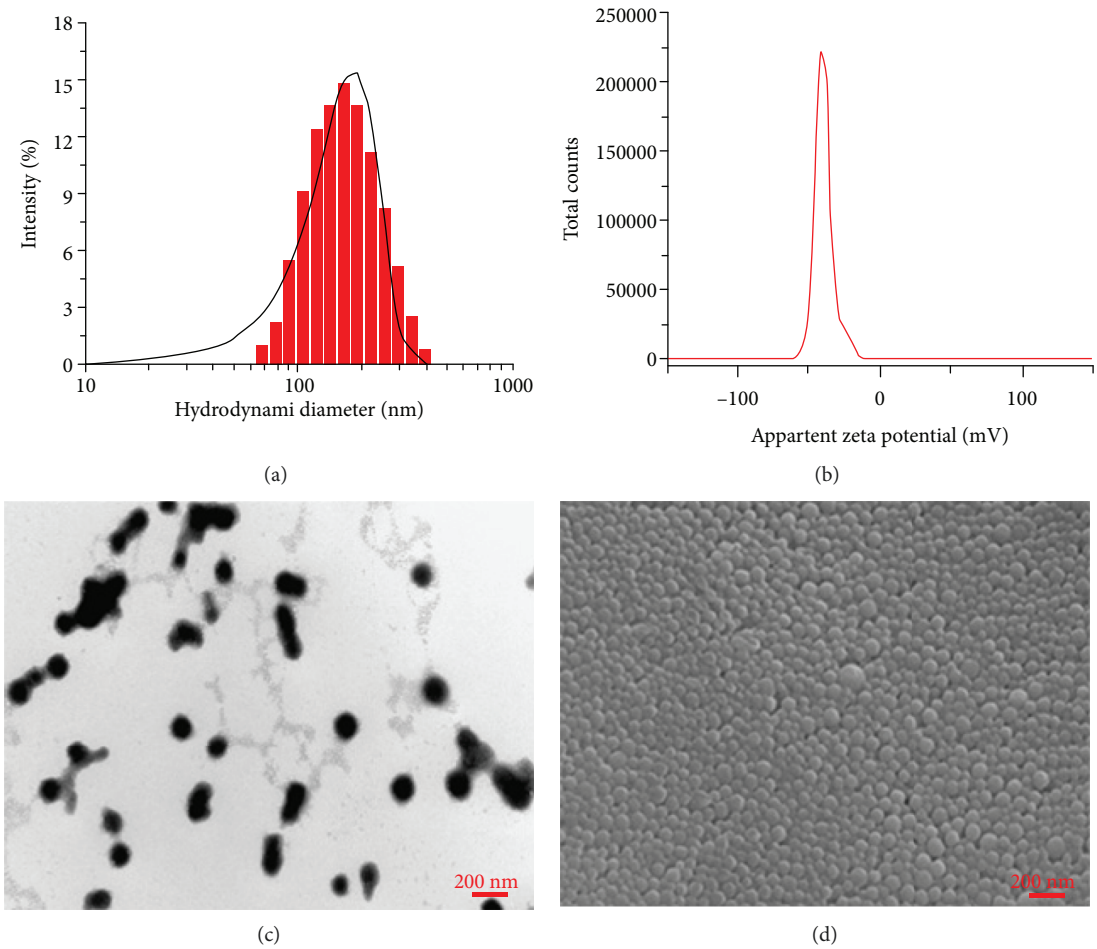

FIGURE 4: (a) Hydrodynamic size distribution, (b) zeta potential, (c) TEM images, and (d) SEM images of mPEG-Rg3-BSA NPs.

NPs, so the optimum pH was determined to be pH 9. As shown in Figure 4, the NP images and size distribution were measured by DLS and electron microscopy. Imaging showed that the NPs were generally spherical in shape with a narrow size distribution and that the mean particle size and zeta potential of the mPEG-Rg3-BSA NPs were 149.5 nm

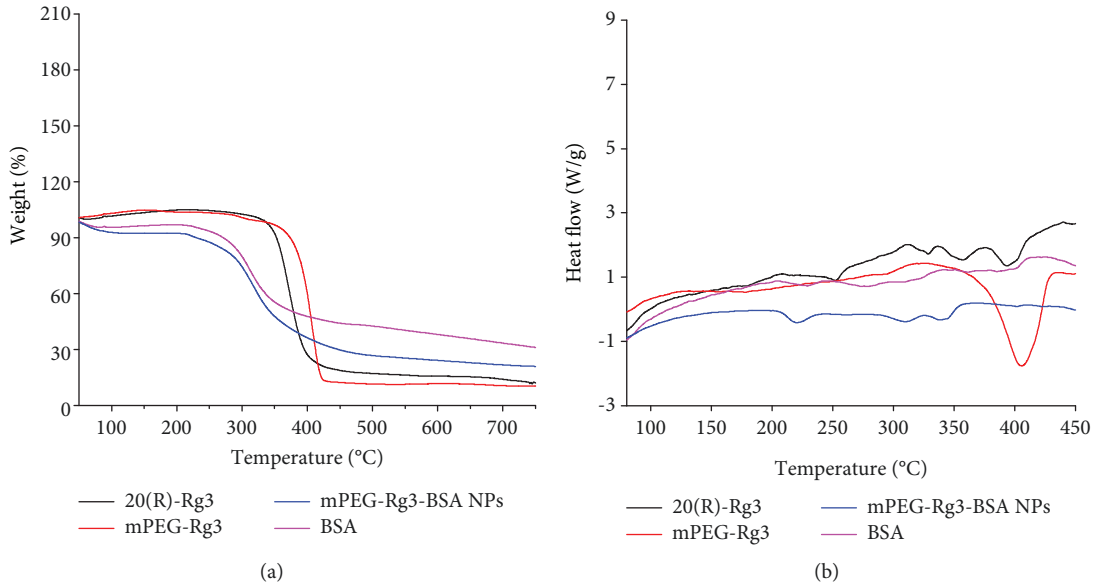

Figure 5: (a) TG analysis curves and (b) DSC thermograms of BSA, mPEG-Rg3-BSA NPs, mPEG-Rg3, and 20(R)-Rg3.

(PDI = 0.117) and -40.2 mV, respectively. The higher the zeta potential, the more stable the NPs. In addition, when the particle size is less than 200 nm, nanoparticles are more likely to enter cells by EPR, and moreover, the size was reported to more efficiently resist capture by RES. The mean drug loading capacity of the mPEG-Rg3-BSA NPs was 17.65%, and the EE value of Rg3 for the mPEG-Rg3-BSA NPs was 76.56%. At the loading level of mPEG-Rg3-BSA NPs, the effective concentration of Rg3 was 6.8 mg/mL, which is 107 times higher than the intrinsic water solubility of free Rg3 (0.063 mg/mL).

3.3. TG and DSC Study. TG is used to analyze the relationship between the quality of sample and temperature change [36]. It can describe the thermal stability of NPs. As shown in Figure 5(a), the results depicted a slower degradation rate of the mPEG-Rg3-BSA NPs, indicating its improved stability compared to Rg3. The curves of Rg3 and mPEG-Rg3 had no significant difference, which showed the degradation of Rg3 and mPEG-Rg3 with respect to increasing temperature. Meanwhile, BSA and mPEG-Rg3-BSA NPs began to lose weight from 50°C to 200°C, which was attributed to water loss. When the temperature was 240°C, abrupt decrease in weight loss happened, which may be due to the loss of small molecules such as ammonia and carbon dioxide. For mPEG-Rg3-BSA NPs, the total ratio of weight loss was about 79.4%. It exhibited a higher weight loss, lower than that for BSA, which is consistent with an increase in organic content of the nanoparticles upon loading of Rg3. Moreover, the results also suggested that the stability of NPs was better than that of Rg3 and the products were successfully degraded at higher temperatures.

DSC is used to evaluate the status of the drug in the drug delivery system and to investigate the potential change of drug properties [37]. As shown in Figure 5(b), the Rg3 powder showed a significant sharp melting peak at 406.21°C, which was also recorded in the mPEG-Rg3 powder. Meanwhile, according to the TG curve, the peak indicated the crystalline state of Rg3. However, the peak disappeared in the thermogram of mPEG-Rg3-BSA NPs, revealing that Rg3 was not in the crystalline state after its presence in the nanoparticles, in accordance with the TG results. In addition, this result indicated that the obtained nanodrug delivery system was stable.

3.4. In Vitro Stability Study. Stability [38] is a very important factor that contributes to the accumulation of NPs at tumor sites. Whether nanoparticles were stable at the nanoscale is key for them to exhibit unique properties. The time-dependent stability of mPEG-Rg3-BSA NPs was determined using the particle size and zeta potential analysis, with respect to different time intervals over 18 days. As shown in Figure 6, there was no significant change in the size and zeta potential of mPEG-Rg3-BSA NPs at 37°C. The size and zeta potential fluctuated at approximately 165 nm and -35 mV, respectively. The results suggested that the stability of mPEG-Rg3-BSA NPs occurred for 18 days in an aqueous system at 37°C.

3.5. In Vitro Drug Release of mPEG-Rg3-BSA NPs. Drug release [39] from nanosized formulations determines the pharmacokinetic properties of a drug in the body after intravenous injection. A sustained drug release pattern is desirable for an injection formulation because of increased systemic exposure, enhanced therapeutic efficacy, and decreased dosing frequency. As shown in Figure 7, the release pattern of Rg3 from NPs was investigated in an in vitro model for 7 days. The initial fast release stage and slow release stage attributed to the continuous degradation of the BSA. The results confirmed that nanodrug delivery system can release

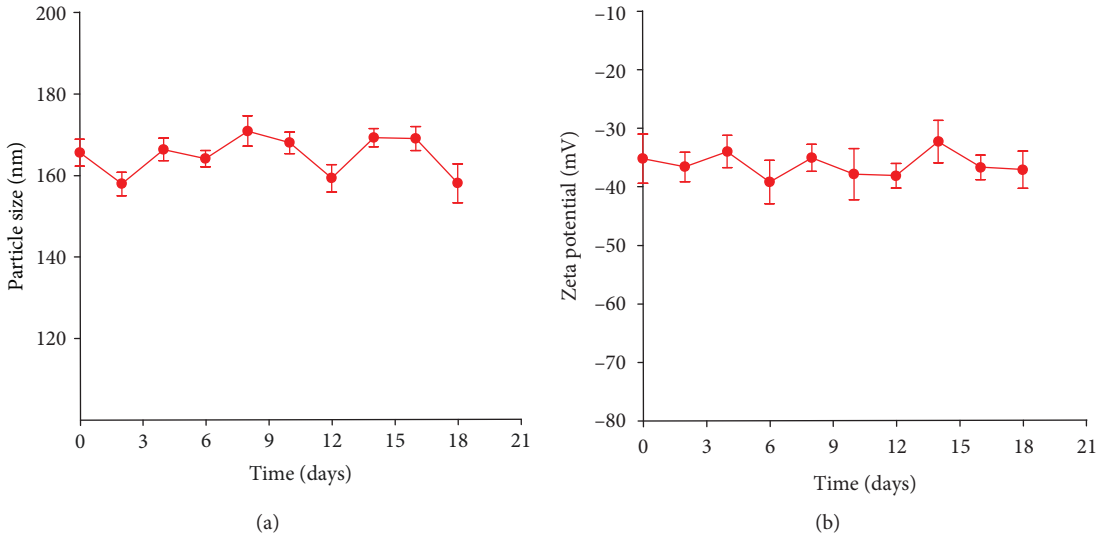

Figure 6: In vitro stability of mPEG-Rg3-BSA NPs at 37°C using particle size analysis (a) and zeta potential analysis (b), with respect to different time intervals. Values are reported as the mean ± SD for triplicate samples.

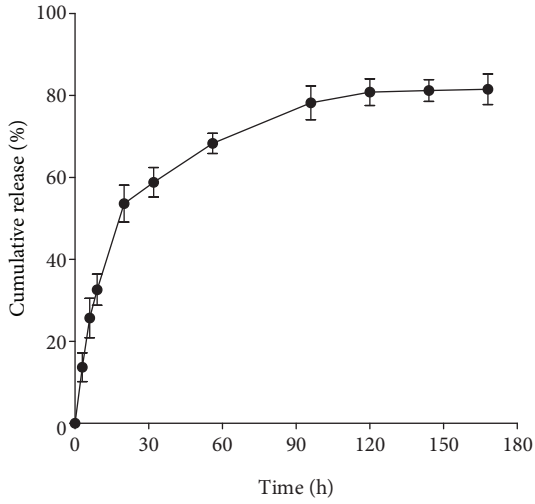

Figure 7: The ginsenoside Rg3 release kinetics from the mPEG-Rg3-BSA NPs in buffer at pH 7.4 and 37°C. Values are reported as the mean ± SD for triplicate samples.

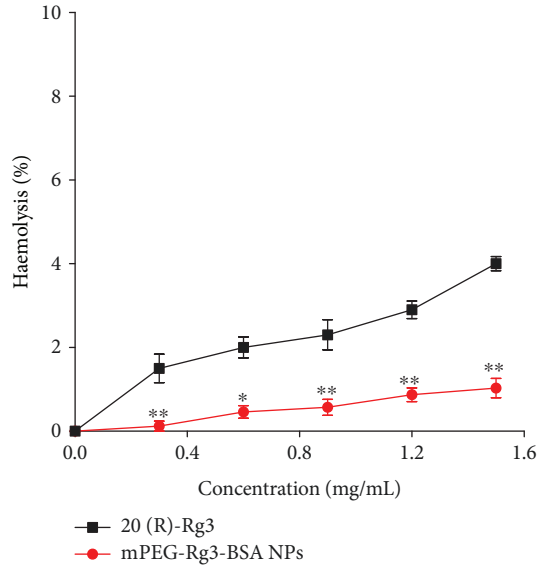

Figure 8: In vitro haemolysis assay of 20(R)-Rg3 and mPEG-Rg3-BSA NPs compared to ultrapure water and physiological saline measured at 545 nm. Values are reported as the mean ± SD for triplicate samples. ∗ represents $p < 0.05$; ∗∗ represents $p < 0.01$.

slowly. Meanwhile, the cumulative release was 59.7% and 85.8% at 32 h and 120 h, respectively. Moreover, the decrease of irregular release behavior may be achieved by long circulation time, thereby enhancing the bioavailability and reducing the cytotoxicity in normal tissues.

3.6. Haemolysis Study. Biocompatibility is a vital factor for in vivo bioapplications [40]. Haemolysis is an important index to evaluate the biocompatibility of nanocarriers, and the quantitative measurement of the haemoglobin released provides an indication of the potential damage to RBCs. In general, drug carriers can be administered by intravenous injection when the haemolysis ratio is less than 5%. As shown in Figure 8, the haemolysis percentages of free Rg3 and mPEG-Rg3-BSA NPs from 0.3 to 1.5 mg/mL were less than 5%. Moreover, the haemolysis of free Rg3 was much higher than those of mPEG-Rg3-BSA NPs, further confirming the safety of mPEG-Rg3-BSA NPs for intravenous injection. This was possibly due to the antihaemolytic properties of the raw material. Collectively, it was concluded that NPs were a kind of a safe tumor drug carrier.

3.7. In Vitro Cell Cytotoxicity. The cytotoxicity of mPEG-Rg3-BSA NPs and free Rg3 to HepG2 and A549 cells was determined by MTT assay [41] to assess the drug delivery efficiency and determine the cell inhibition rate and antiactivity in vitro. The cell inhibition rate was measured at 24 h,

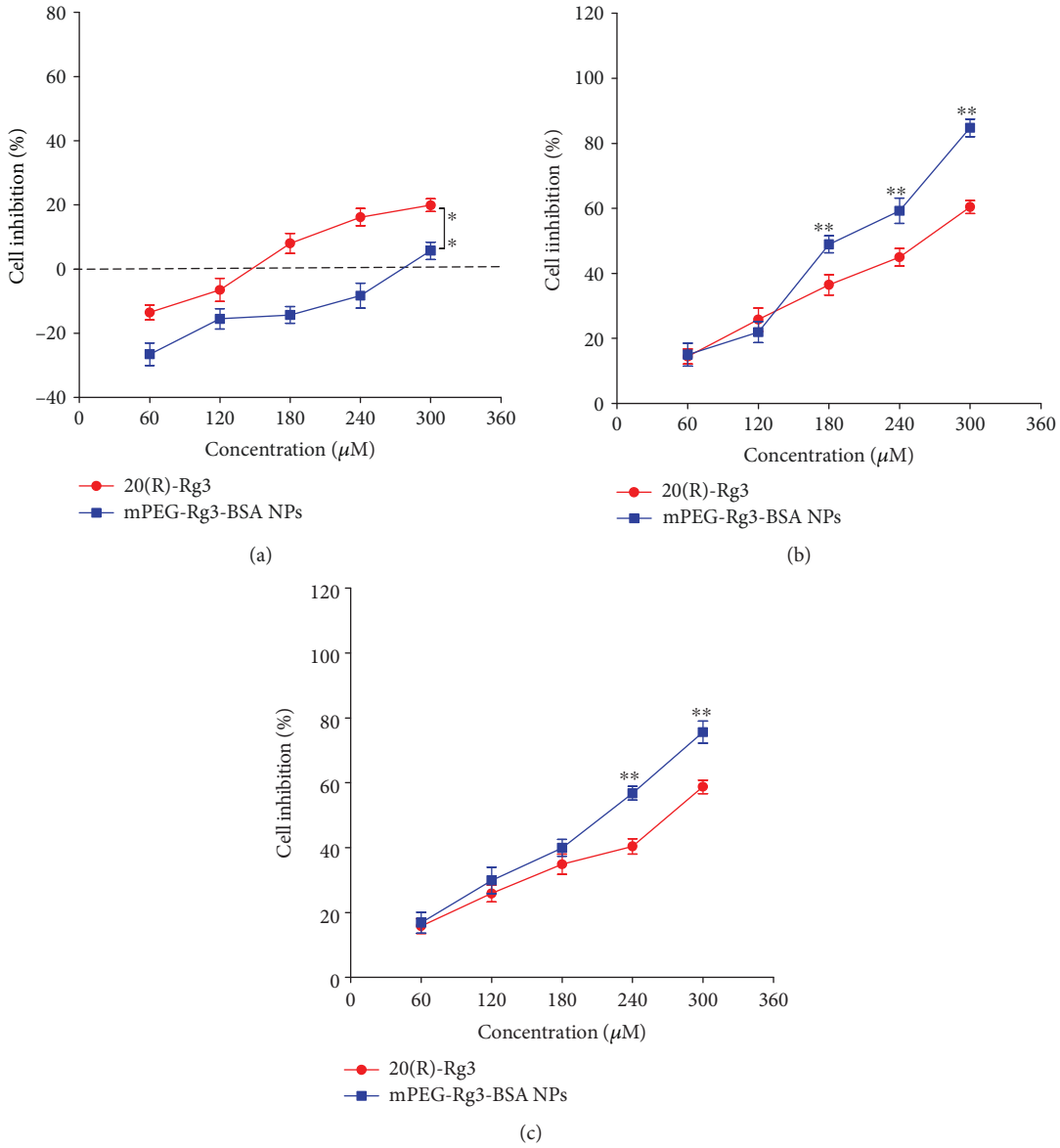

FIGURE 9: The cell viability of L929 cells (a) and HepG2 cells (b) and A549 cells (c) treated for 24 h measured using an MTT assay. Values are reported as the mean ± SD for triplicate samples. ∗ represents $p < 0.05$.

and the concentration of all samples was calculated based on the amount of Rg3 present in the nanoparticles. As shown in Figure 9(a), for the L929 cells, the inhibition rate of the free Rg3 and mPEG-Rg3-BSA NPs was increased with increasing Rg3 drug concentrations but mPEG-Rg3-BSA NPs more promoted cell proliferation than free Rg3 at 60~120 μM. As shown in Figure 9(b), for the HepG2 cells, the inhibition rate of the mPEG-Rg3-BSA NPs was increased with increasing drug concentrations and the cell cytotoxicity of mPEG-Rg3-BSA NPs was higher than that of free Rg3 at the same concentration. When the concentration of drug was 240 μM, the inhibition rates of the mPEG-Rg3-BSA NPs and free Rg3 were 59.20% and 40.08%, respectively, and the IC_{50} values of the mPEG-Rg3-BSA NP- and free Rg3-treated HepG2 cells were 195.3 μM and 252.88 μM, respectively. As shown in Figure 9(b), for the A549 cells, there was similar anticancer effect between mPEG-Rg3-BSANPs and free Rg3 at 24 h at the same concentration of Rg3. When the concentration of drug was 240 μM, the inhibition rates of the mPEG-Rg3-BSA NPs and free Rg3 were 56.75% and 40.38%, respectively, and the IC_{50} values of the mPEG-Rg3-BSA NP- and free Rg3-treated HepG2 cells were 207.51 μM and 266.76 μM, respectively. As a whole, the cell inhibition rate of HepG2 cells was higher than that of the A549 cells at 24 h. Therefore, these results suggested that our fabricated mPEG-Rg3-BSA NPs could be an efficient drug carrier for the targeted cancer therapy of HepG2 cells and the cytotoxicity of mPEG-Rg3-BSA NPs was higher than that of free Rg3 to cancer cells. Collectively, the nanodrug delivery system enhanced the anticancer activity of drug to cancer cells and decreased the cytotoxicity of Rg3 to normal cells.

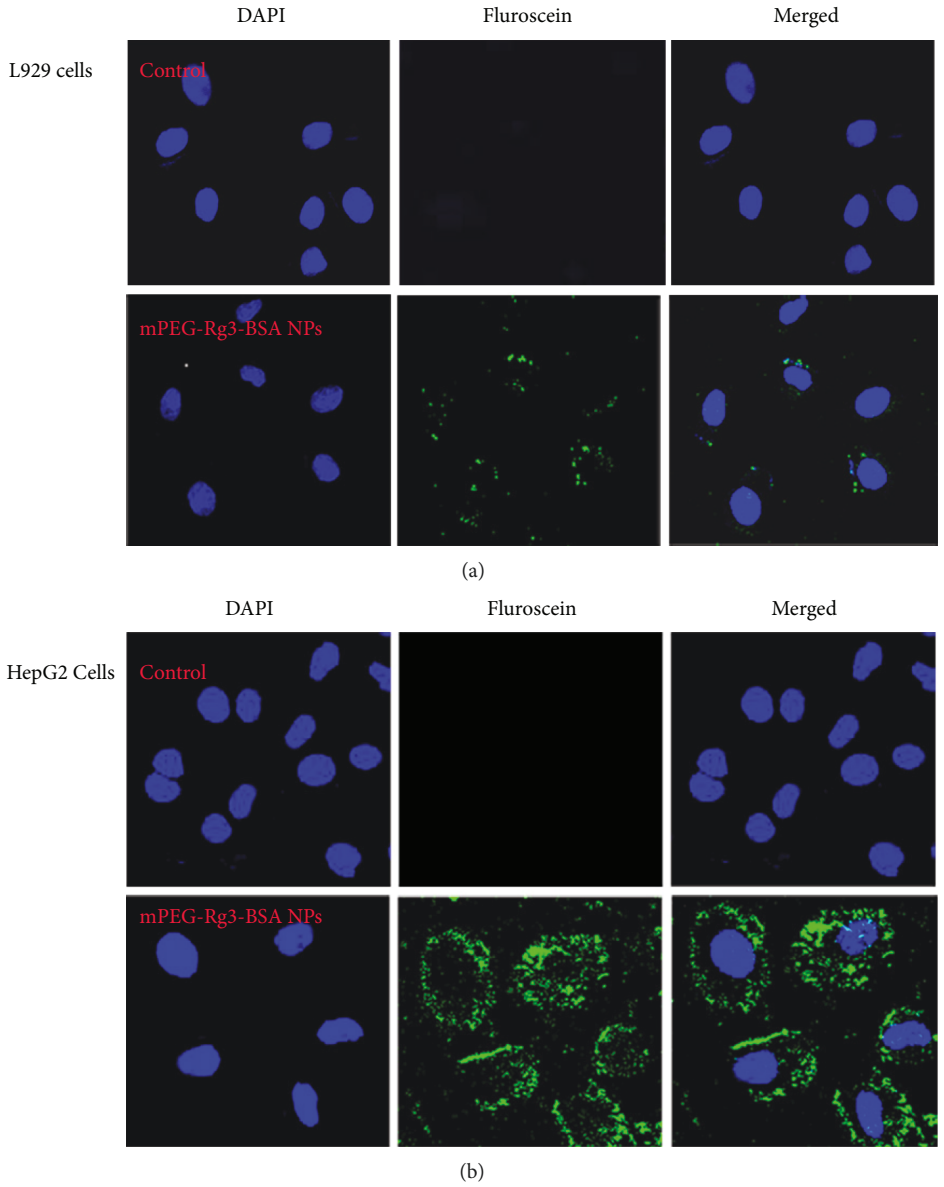

Figure 10: mPEG-Rg3-BSA NP uptake by cultured L929 and HepG2 cells. L929 and HepG2 cell monolayers were incubated with cell culture medium (control) and FITC-labelled nanoparticles (180 μM) for 4 h at 37°C. Magnification is ×800.

3.8. Cellular Uptake Assay. In general, free drug molecules entered the cytoplasm of the cell by passive diffusion. However, NPs were taken up by cells through an endocytic pathway and endocytic delivery using nanoparticles maintains a higher concentration in the cytoplasm for nanoparticles comparing with free drug. To study the effective drug delivery of NPs, L929 and HepG2 cell monolayers were incubated with FITC-labelled nanoparticles [42]. When the concentration of mPEG-Rg3-BSA NPs was 180 μM, the cell-associated fluorescence was evaluated using a fluorescence spectrophotometer. As shown in Figure 10, the green image demonstrated that the FITC-labelled mPEG-Rg3-BSANPs entered the cytoplasm of L929 cells and HepG2 cells and HepG2 cells contained higher fluorescence intensity than L929 cells. The results confirmed that nanoparticles were more efficiently taken up by tumor cells. In addition, the images also revealed the anticancer effect and apoptosis of cancer cells caused by mPEG-Rg3-BSA NPs.

3.9. Apoptosis Assay. HepG2 cell apoptosis caused by mPEG-Rg3-BSA NPs and free Rg3 was characterized by Hoechst 33342 staining [43]. In general, morphological changes, such as cell shrinkage and condensed and fragmented chromatin, are associated with apoptotic cell death. As shown in Figure 11, the Hoechst 33342 staining results were obtained using fluorescence microscopy and the control cells did not show any apoptotic bodies. Cells that were treated with increasing concentrations of mPEG-Rg3-BSA NPs and free Rg3 showed a progressive accumulation of condensed and fragmented chromatin. Furthermore, when the concentration of Rg3 was 300 μM, the apoptosis rate caused by mPEG-Rg3-BSA NPs was much higher than that by the free

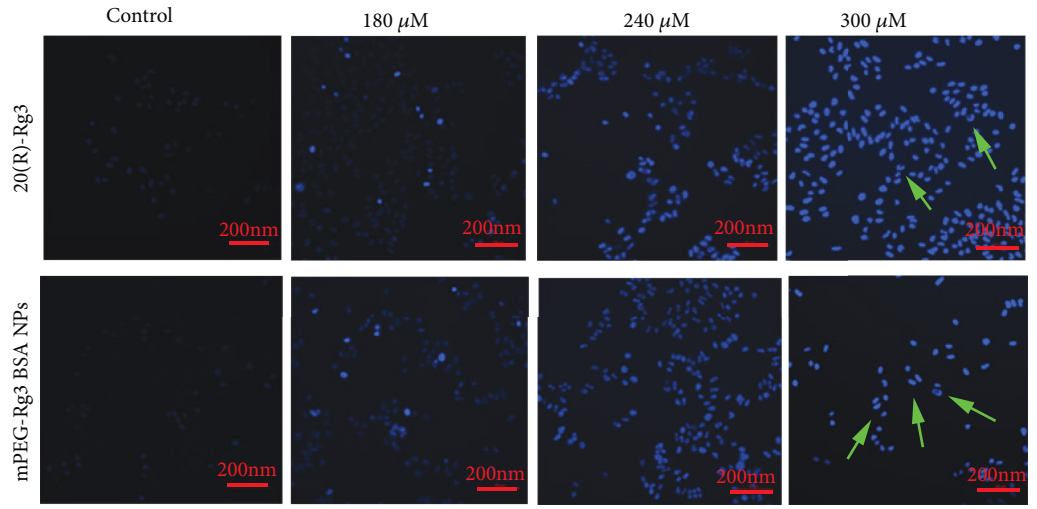

Figure 11: Apoptosis of HepG2 cells from 20(R)-Rg3 and mPEG-Rg3-BSA NPs evaluated by Hoechst 33342 staining. Magnification is ×100.

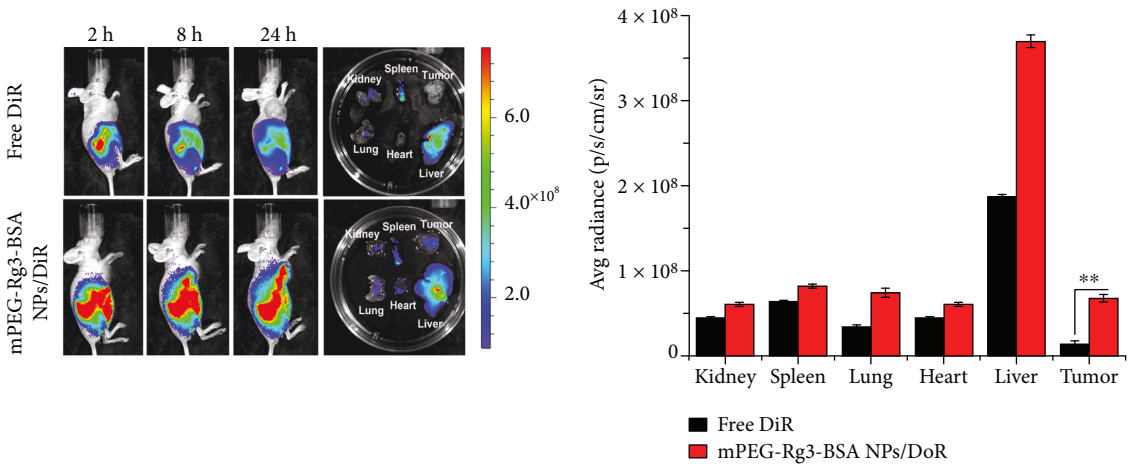

(a) (b)

Figure 12: (a) In vivo whole-animal imaging of mice bearing subcutaneous HepG2 tumors treated with free DiR and mPEG-Rg3-BSA NPs/DiR with different formulations at 2 h, 8 h, and 24 h and ex vivo fluorescence imaging of dissected organs after 24 h postinjection; (b) quantitative analysis of the fluorescence intensity of DiR in tumor tissue examined using the in vivo imaging system. Values are reported as the mean ± SD for triplicate samples. ∗∗ represents $p < 0.01$.

Rg3, and for the mPEG-Rg3-BSA NPs, the number of nuclei decreased. This demonstrated the apoptotic mechanism of cell death that occurred in cancer cells after exposure to mPEG-Rg3-BSA NPs and free Rg3. Moreover, the results also showed that the cytotoxicity for mPEG-Rg3-BSA NPs to cancer cells was higher than free Rg3.

3.10. Biodistribution of DiR-Loaded mPEG-Rg3-BSA NPs in Tumor-Bearing Mice. To estimate the in vivo biodistribution behavior of the mPEG-Rg3-BSA NPs, free DiR and DiR-labelled mPEG-Rg3-BSA NPs were injected into tumor-bearing mice. As shown in Figure 12, in the DiR-labelled mPEG-Rg3-BSA NP group, the fluorescence of DiR in the body of the mouse remained throughout the full experiment. However, the fluorescence of DiR quickly declined from 8 h postinjection for the free DiR group. Results confirmed that the fluorescence intensity appeared at the tumor site and was increasing as the time passes. DiR-labelled mPEG-Rg3-BSA NPs exhibited better accumulation than the free DiR group in the tumor; the fluorescence intensity at the tumor site was 5.4-fold higher than that of free DiR. Thus, we concluded that the hydrophilic corona preferable passive targeting ability of the NPs could significantly prolong drug blood circulation, which was beneficial for the mPEG-Rg3-BSA NPs to achieve an EPR effect.

4. Conclusions

In conclusion, this study used the mPEGylation method and selected BSA as the nanocarrier to prepare the nanodrug delivery system. This nanodrug delivery system improved the property of Rg3 and exhibited several attractive properties,

including good slow-release properties, good stability, the low cytotoxicity to the normal cells, and the selective ability to tumor cells. Furthermore, the mPEG-Rg3-BSA NPs enhanced the therapeutic effects compared to free Rg3. Therefore, it was a promising nanodrug delivery system for cancer therapy and the solubility and therapeutic effect of Rg3 could be better employed for future therapeutic applications by loading it in a BSA nanocarrier.

Data Availability

The data used to support the findings of this study are include within the article, which permits unrestricted use, distribution, and reproduction in any medium, provided that the original work is properly cited.

Conflicts of Interest

The authors declared no potential conflicts of interest with respect to the research, authorship, and/or publication of this article.

Acknowledgments

This study was financially supported by the National Natural Science Foundation of China (21676214, 21676215), Shaanxi Key Laboratory of Degradable Biomedical Materials Program (2014SZS07-K04, 2014SZS07-P05, js103, 2014SZS07-Z01, 2014SZS07-Z02, 2015SZSj-42, 2016SZSj-35, and 2014SZS07-K03), and Shaanxi R&D Center of Biomaterials and Fermentation Engineering Program (2015HBGC-04).

References

[1] T. T. Zuo, R. S. Zheng, H. M. Zeng, S. W. Zhang, and W. Q. Chen, "Female breast cancer incidence and mortality in China, 2013," *Thoracic Cancer*, vol. 8, no. 3, pp. 214–218, 2017.

[2] A. Stornetta, M. Zimmermann, G. D. Cimino, P. T. Henderson, and S. J. Sturla, "DNA adducts from anticancer drugs as candidate predictive markers for precision medicine," *Chemical Research in Toxicology*, vol. 30, no. 1, pp. 388–409, 2017.

[3] J. Upadhyaya, M. J. Kim, Y. H. Kim, S. R. Ko, H. W. Park, and M. K. Kim, "Enzymatic formation of compound-K from ginsenoside Rb1 by enzyme preparation from cultured mycelia of *Armillaria mellea*," *Journal of Ginseng Research*, vol. 40, no. 2, pp. 105–112, 2016.

[4] X. Zheng, W. Chen, H. Hou et al., "Ginsenoside 20(S)-Rg3 induced autophagy to inhibit migration and invasion of ovarian cancer," *Biomedicine & Pharmacotherapy*, vol. 85, pp. 620–626, 2017.

[5] Y. Zhang, Q. Z. Liu, S. P. Xing, and J. L. Zhang, "Inhibiting effect of Endostar combined with ginsenoside Rg3 on breast cancer tumor growth in tumor-bearing mice," *Asian Pacific Journal of Tropical Medicine*, vol. 9, no. 2, pp. 180–183, 2016.

[6] M. Mochizuki, Y. C. Yoo, K. Matsuzawa et al., "Inhibitory effect of tumor metastasis in mice by saponins, ginsenoside-Rb2, 20 (R)-and 20 (S)-ginsenoside-Rg3, of red ginseng," *Biological and Pharmaceutical Bulletin*, vol. 18, no. 9, pp. 1197–1202, 1995.

[7] I. H. Park, J. H. Sohn, S. B. Kim et al., "An open-label, randomized, parallel, phase III trial evaluating the efficacy and safety of polymeric micelle-formulated paclitaxel compared to conventional Cremophor EL-based paclitaxel for recurrent or metastatic HER2-negative breast cancer," *Cancer Research and Treatment*, vol. 49, no. 3, pp. 569–577, 2017.

[8] J. S. Suk, Q. Xu, N. Kim, J. Hanes, and L. M. Ensign, "PEGylation as a strategy for improving nanoparticle-based drug and gene delivery," *Advanced Drug Delivery Reviews*, vol. 99, Part A, pp. 28–51, 2016.

[9] I. A. Lázaro, S. Haddad, S. Sacca, C. Orellana-Tavra, D. Fairen-Jimenez, and R. S. Forgan, "Selective surface PEGylation of UiO-66 nanoparticles for enhanced stability, cell uptake, and pH-responsive drug delivery," *Chem*, vol. 2, no. 4, pp. 561–578, 2017.

[10] W. Li, P. Zhan, E. de Clercq, H. Lou, and X. Liu, "Current drug research on PEGylation with small molecular agents," *Progress in Polymer Science*, vol. 38, no. 3-4, pp. 421–444, 2013.

[11] H. Zhang, H. Hu, H. Zhang et al., "Effects of PEGylated paclitaxel nanocrystals on breast cancer and its lung metastasis," *Nanoscale*, vol. 7, no. 24, pp. 10790–10800, 2015.

[12] L. O. F. Monteiro, R. S. Fernandes, C. M. R. Oda et al., "Paclitaxel-loaded folate-coated long circulating and pH-sensitive liposomes as a potential drug delivery system: a biodistribution study," *Biomedicine & Pharmacotherapy*, vol. 97, pp. 489–495, 2018.

[13] C. Menzel, T. Holzeisen, F. Laffleur et al., "In vivo evaluation of an oral self-emulsifying drug delivery system (SEDDS) for exenatide," *Journal of Controlled Release*, vol. 277, pp. 165–172, 2018.

[14] A. A. Natfji, D. Ravishankar, H. M. I. Osborn, and F. Greco, "Parameters affecting the enhanced permeability and retention effect: the need for patient selection," *Journal of Pharmaceutical Sciences*, vol. 106, no. 11, pp. 3179–3187, 2017.

[15] J. Loureiro, S. Andrade, A. Duarte et al., "Resveratrol and grape extract-loaded solid lipid nanoparticles for the treatment of Alzheimer's disease," *Molecules*, vol. 22, no. 2, p. 277, 2017.

[16] H. Nosrati, M. Adibtabar, A. Sharafi, H. Danafar, and M. Hamidreza Kheiri, "PAMAM-modified citric acid-coated magnetic nanoparticles as pH sensitive biocompatible carrier against human breast cancer cells," *Drug Development and Industrial Pharmacy*, vol. 44, no. 8, pp. 1377–1384, 2018.

[17] H. Nosrati, E. Javani, M. Salehiabar, H. Kheiri Manjili, S. Davaran, and H. Danafar, "Biocompatibility and anticancer activity of L-phenyl alanine-coated iron oxide magnetic nanoparticles as potential chrysin delivery system," *Journal of Materials Research*, vol. 33, no. 11, pp. 1602–1611, 2018.

[18] M. Salehiabar, H. Nosrati, E. Javani et al., "Production of biological nanoparticles from bovine serum albumin as controlled release carrier for curcumin delivery," *International Journal of Biological Macromolecules*, vol. 115, pp. 83–89, 2018.

[19] H. Nosrati, R. Abbasi, J. Charmi et al., "Folic acid conjugated bovine serum albumin: an efficient smart and tumor targeted biomacromolecule for inhibition folate receptor positive cancer cells," *International Journal of Biological Macromolecules*, vol. 117, pp. 1125–1132, 2018.

[20] H. Nosrati, A. Rakhshbahar, M. Salehiabar et al., "Bovine serum albumin: an efficient biomacromolecule nanocarrier for improving the therapeutic efficacy of chrysin," *Journal of Molecular Liquids*, vol. 271, pp. 639–646, 2018.

[21] L. Roufegarinejad, A. Jahanban-Esfahlan, S. Sajed-Amin, V. Panahi-Azar, and M. Tabibiazar, "Molecular interactions of thymol with bovine serum albumin: spectroscopic and

molecular docking studies," *Journal of Molecular Recognition*, vol. 31, no. 7, article e2704, 2018.

[22] S. M. H. AL-Jawad, A. A. Taha, M. M. F. Al-Halbosiy, and L. F. A. AL-Barram, "Synthesis and characterization of small-sized gold nanoparticles coated by bovine serum albumin (BSA) for cancer photothermal therapy," *Photodiagnosis and Photodynamic Therapy*, vol. 21, pp. 201–210, 2018.

[23] B. White, A. Evison, E. Dombi, and H. E. Townley, "Improved delivery of the anticancer agent citral using BSA nanoparticles and polymeric wafers," *Nanotechnology, Science and Applications*, vol. 10, pp. 163–175, 2017.

[24] S. Thakur, N. Hashim, S. Neogi, and A. K. Ray, "Size-dependent adsorption and conformational changes induced in bovine serum albumin (BSA) on exposure to titanium dioxide (TiO_2) nanoparticles," *Journal of Separation Science*, vol. 52, no. 3, pp. 421–434, 2017.

[25] Y. Wen, H. Dong, Y. Li, A. Shen, and Y. Li, "Nano-assembly of bovine serum albumin driven by rare-earth-ion (Gd) biomineralization for highly efficient photodynamic therapy and tumor imaging," *Journal of Materials Chemistry B*, vol. 4, no. 4, pp. 743–751, 2016.

[26] P. Singh, Y. J. Kim, H. Singh, S. Ahn, V. Castro-Aceituno, and D. C. Yang, "In situ preparation of water-soluble ginsenoside Rh2-entrapped bovine serum albumin nanoparticles: in vitro cytocompatibility studies," *International Journal of Nanomedicine*, vol. 12, pp. 4073–4084, 2017.

[27] P. Singh, H. Singh, V. Castro-Aceituno, S. Ahn, Y. J. Kim, and D. C. Yang, "Bovine serum albumin as a nanocarrier for the efficient delivery of ginsenoside compound K: preparation, physicochemical characterizations and in vitro biological studies," *RSC Advances*, vol. 7, no. 25, pp. 15397–15407, 2017.

[28] H. Y. Cheung and Q. F. Zhang, "Enhanced analysis of triterpenes, flavonoids and phenolic compounds in *Prunella vulgaris* L. by capillary zone electrophoresis with the addition of running buffer modifiers," *Journal of Chromatography A*, vol. 1213, no. 2, pp. 231–238, 2008.

[29] J. Li and Y. Guo, "Basic evaluation of typical nanoporous silica nanoparticles in being drug carrier: structure, wettability and hemolysis," *Materials Science and Engineering: C*, vol. 73, pp. 670–673, 2017.

[30] L. Q. Thao, C. Lee, B. Kim et al., "Doxorubicin and paclitaxel co-bound lactosylated albumin nanoparticles having targetability to hepatocellular carcinoma," *Colloids and Surfaces B: Biointerfaces*, vol. 152, pp. 183–191, 2017.

[31] R. Yang, D. Chen, M. Li, F. Miao, P. Liu, and Q. Tang, "20(s)-ginsenoside Rg3-loaded magnetic human serum albumin nanospheres applied to HeLa cervical cancer cells in vitro," *Bio-Medical Materials and Engineering*, vol. 24, no. 6, pp. 1991–1998, 2014.

[32] X. Zheng, Z. Li, L. Chen, Z. Xie, and X. Jing, "Self-assembly of porphyrin–paclitaxel conjugates into nanomedicines: enhanced cytotoxicity due to endosomal escape," *Chemistry - An Asian Journal*, vol. 11, no. 12, pp. 1780–1784, 2016.

[33] I. S. Choi, C. M. Kim, and S. J. Jang, "Screening antibiotics using an Hoechst 33342 dye-accumulation assay to detect efflux activity in *Acinetobacter baumannii* clinical isolates," *Asian Biomedicine*, vol. 11, no. 4, pp. 371–378, 2018.

[34] Z. Yang, N. Sun, R. Cheng, C. Zhao, J. Liu, and Z. Tian, "Hybrid nanoparticles coated with hyaluronic acid lipoid for targeted co-delivery of paclitaxel and curcumin to synergistically eliminate breast cancer stem cells," *Journal of Materials Chemistry B*, vol. 5, no. 33, pp. 6762–6775, 2017.

[35] C. Tang, Y. Wang, Y. Long, X. An, J. Shen, and Y. Ni, "Anchoring 20(R)-ginsenoside Rg3 onto cellulose nanocrystals to increase the hydroxyl radical scavenging activity," *ACS Sustainable Chemistry & Engineering*, vol. 5, no. 9, pp. 7507–7513, 2017.

[36] R. Mathiyalagan, S. Subramaniyam, Y. J. Kim et al., "Synthesis and pharmacokinetic characterization of a pH-sensitive polyethylene glycol ginsenoside CK (PEG-CK) conjugate," *Bioscience Biotechnology and Biochemistry*, vol. 78, no. 3, pp. 466–468, 2014.

[37] A. Jahanban-Esfahlan, S. Dastmalchi, and S. Davaran, "A simple improved desolvation method for the rapid preparation of albumin nanoparticles," *International Journal of Biological Macromolecules*, vol. 91, pp. 703–709, 2016.

[38] H. Nosrati, M. Salehiabar, H. K. Manjili, H. Danafar, and S. Davaran, "Preparation of magnetic albumin nanoparticles via a simple and one-pot desolvation and co-precipitation method for medical and pharmaceutical applications," *International Journal of Biological Macromolecules*, vol. 108, pp. 909–915, 2018.

[39] S. Emami, H. Valizadeh, Z. Islambulchilar, and P. Zakeri-Milani, "Development and physicochemical characterization of sirolimus solid dispersions prepared by solvent evaporation method," *Advanced Pharmaceutical Bulletin*, vol. 4, no. 4, pp. 369–374, 2014.

[40] P. Singh, H. Singh, V. Castro-Aceituno et al., "Engineering of mesoporous silica nanoparticles for release of ginsenoside CK and Rh2 to enhance their anticancer and anti-inflammatory efficacy: in vitro studies," *Journal of Nanoparticle Research*, vol. 19, no. 7, p. 257, 2017.

[41] G. Kabay, C. Demirci, G. Kaleli Can, A. E. Meydan, B. G. Daşan, and M. Mutlu, "A comparative study of single-needle and coaxial electrospun amyloid-like protein nanofibers to investigate hydrophilic drug release behavior," *International Journal of Biological Macromolecules*, vol. 114, pp. 989–997, 2018.

[42] Y. Zu, L. Meng, X. Zhao et al., "Preparation of 10-hydroxycamptothecin-loaded glycyrrhizic acid-conjugated bovine serum albumin nanoparticles for hepatocellular carcinoma - targeted drug delivery," *International Journal of Nanomedicine*, vol. 8, pp. 1207–1222, 2013.

[43] N. B. N. N. Tran, F. Knorr, W. C. Mak et al., "Gradient-dependent release of the model drug TRITC-dextran from FITC-labeled BSA hydrogel nanocarriers in the hair follicles of porcine ear skin," *European Journal of Pharmaceutics and Biopharmaceutics*, vol. 116, pp. 12–16, 2017.

Hindawi
Journal of Nanomaterials
Volume 2019, Article ID 9486745, 9 pages
https://doi.org/10.1155/2019/9486745

Research Article

Structural Evolution and Photoluminescence of SiO_2 Layers with Sn Nanoclusters Formed by Ion Implantation

I. Romanov,[1] F. Komarov,[2] O. Milchanin,[2] L. Vlasukova,[1] I. Parkhomenko,[1] M. Makhavikou,[2] E. Wendler,[3] A. Mudryi,[4] and A. Togambayeva[5]

[1]*Belarusian State University, 4 Nezavisimosti Ave, Minsk 220030, Belarus*
[2]*A.N. Sevchenko Research Institute of Applied Physical Problems, Belarusian State University, 7 Kurchatova St., Minsk 220045, Belarus*
[3]*Institut für Festkörperphysik, Friedrich-Schiller-Universität Jena, Max-Wien-Platz 1, D-07743 Jena, Germany*
[4]*Scientific and Practical Materials Research Center, National Academy of Sciences of Belarus, P. Brovki Str. 17, 220072 Minsk, Belarus*
[5]*Al-Farabi Kazakh National University, Al-Farabi Ave. 71, Almaty 050040, Kazakhstan*

Correspondence should be addressed to F. Komarov; komarovf@bsu.by

Received 18 July 2018; Revised 28 November 2018; Accepted 9 December 2018; Published 26 March 2019

Guest Editor: Bathula Babu

Samples of SiO_2 (600 nm)/Si have been implanted with Sn ions (200 keV, 5×10^{16} cm^{-2} and 1×10^{17} cm^{-2}) at room temperature and afterwards annealed at 800 and 900°C for 60 minutes in ambient air. The structural and light emission properties of "SiO_2 +Sn-based nanocluster" composites have been studied using Rutherford backscattering spectroscopy, transmission electron microscopy in cross section and plan-view geometry, electron microdiffraction, and photoluminescence (PL). A strict correspondence of Sn concentration profiles and depth particle distributions has been found. In the case of 1×10^{17} cm^{-2} fluence, the impurity accumulation in the subsurface zone during the thermal treatment leads to swelling and to the formation of dendrites composed of large and coalesced nanoparticles of grey contrast. The appearance of dendrites is most probably due to the SnO_2 phase formation. The as-implanted samples are characterized by a weak emission with maximum at the blue range (2.9 eV). The PL intensity increases by an order of magnitude after annealing in an oxidizing atmosphere. The narrowest and most intense PL band has maximum at 3.1 eV. Its intensity increases with increasing fluence and annealing temperature. This emission can be attributed to the formation of the SnO_2 phase (in the form of separate clusters or shells of Sn clusters) in the subsurface region of the SiO_2 matrix.

1. Introduction

Silicon dioxide layers are the most common material in optical fiber manufacturing and microelectronics as a thin electric isolator in a metal-oxide-semiconductor (MOS) transistor and a diffusion barrier. At present, adding optical functionality to a silicon microelectronic chip is one of the most challenging problems of materials research. Thereby, considerable efforts have been focused on the enhancement of UV and visible emission from silica to create an active light-emitting element in next-generation miniature optoelectronic devices [1–12]. In spite of typical optoelectronic's operation in IR range, the creation of such silica-based emitters operating in both the visible and UV-violet spectral ranges is a perspective for creating a microminiature MOS light-emitting diode (LED), Bragg reflectors, waveguide lasers, and optocouplers as well as optical switchers in color microdisplay devices. To fabricate a low-cost effective silica-based LED, the ion implantation approach seems quite promising because of well-controlled impurity atom distribution and/or impurity-based nanocrystal formation, good passivation from ambient condition, and excellent compatibility with Si MOS processes [1–4, 10–12].

It is reported that Si-, Ge-, and Sn-implanted SiO_2 films exhibit strong blue-violet (UV) photoluminescence (PL) [1–4]. According to Ref. [1], the Sn-rich silica films exhibit

the strongest photoluminescence (PL) intensity among these composites. Motivated by this result, we devote the present article to Sn-implanted silicon oxide films.

Although the modification of the SiO_2 matrix by means of ion implantation for a light emission increase is developed sufficiently, the unsolved problems still remain. Among them, the main one is a mechanism of radiative recombination. On the one hand, ion implantation results in modification of the silica matrix. So, high-fluence Sn implantation results in the formation of optical active oxygen divacancies (twofold coordinated Sn atom bonded to the rest of the silica network via two oxygen atoms). Such Sn-related color centers emit PL at 3.15 eV due to a triplet-singlet transition [1, 5, 13]. On the other hand, high-fluence ion implantation results in the formation of nanoclusters in the silica matrix. Namely, Sn implantation followed by heat treatment can result in the formation of different Sn-based phases depending on the annealing regime and environment. Namely, the formation of metallic β-Sn precipitates as well as SnO_x nanoparticles can take place after annealing in vacuum or N_2 ambient condition in the range of 600–1100°C [3, 4]. In some cases, Sn cores with SnO_{2-x} shells were found [3]. On the contrary, the formation of SnO_2 nanoparticles also took place after annealing in an oxidizing atmosphere (air or pure oxygen) in the temperature range of 400–1000°C [10, 11, 14]. Tin dioxide is known as a semiconductor with a wide direct bandgap of 3.6 eV, which is dipole forbidden. But direct gap luminescence can be allowed in SnO_2 nanocrystals (NCs). Indeed, nanocrystalline SnO_2 thin films [15, 16] and nanoparticles [17] exhibit strong UV and visible luminescence, which is dependent on surface states and deep-level defects. Thus, it is important to clarify what processes (modification of the silica matrix itself or creation of a new phase in the form of nanoclusters) play a crucial role in a radiative recombination mechanism in Sn-implanted silica.

Considering the complicated phase composition as well as the presence of different radiative and nonradiative centers in Sn-implanted films, the deep analysis of structural and luminescence properties depending on the regime of implantation and subsequent annealing is needed. In spite of a number of publications devoted to silicon oxide films implanted with Sn ions [1–4, 10–12], the influence of implantation fluence on their structure and luminescence was studied insufficiently. In this paper, we report the structural and light-emitting properties of "SiO_2+Sn-based NC" composites created by means of Sn^+ implantation with two different fluences into SiO_2 on Si followed by oxidation in ambient air. We have tried to find out a correlation between Sn concentration depth profiles, Sn-based precipitate distributions in the SiO_2 layers, and photoluminescence of composites under investigation.

2. Experiment

The initial samples (2×2 cm^2) of SiO_2/Si structures were cut from the thermally oxidized Si substrates. The thickness of the SiO_2 layer as measured by transmission electron microscopy in cross section geometry (XTEM) was 600 nm. These samples were implanted at room temperature with 200 keV Sn ions to fluences of 5×10^{16} and 1×10^{17} cm^{-2}. Computer simulation (SRIM) gave Gaussian-type Sn concentration-depth profiles with the peak concentrations of about 11 at.% (for 5×10^{16} cm^{-2}) and of about 22 at.% (for 1×10^{17} cm^{-2}) formed at the depth of 100 nm in the oxide matrix. Afterwards, a part of the samples was annealed at 800 or 900°C for 60 min in ambient air.

The Sn distribution profiles of the implanted and annealed samples were analyzed by Rutherford backscattering spectroscopy (RBS), using 1.5 MeV He^+ ions. Fitting of experimental RBS spectra to the simulated ones was carried out using the SIMNRA code. In the calculated concentration profiles of tin atoms, the transition of the depth scale from the laboratory coordinate system to the metric one was carried out on the basis of the thickness of the oxide layer of the samples measured by transmission electron microscopy (TEM).

The structural investigations and phase analysis in the samples were carried out using TEM in "plan-view" and "cross section" geometry as well as electron microdiffraction. A Hitachi H-800 analytical electron microscope operating at 200 keV was used for these studies. Samples for TEM research in both geometries ("plan-view" and "cross-section") were prepared by the conventional technique that included precision cutting, cutting wheels, grinding, polishing, and Ar^+ ion polishing using Gatan equipment. In the finishing treatment, low energies of ion beams (3-5 keV) and sliding etching angles (3-5°) were used, which ensured the nonintroduction of structural defects into the samples during their preparation.

Photoluminescence spectra were recorded at room temperature in the energy range of 1.77–3.54 eV using a diffraction monochromator with a focal distance of 0.6 m. The 3.81 eV (325 nm) emission line of a continuous wave He-Cd laser was used for excitation. The emission bandwidth of equipment was chosen to be 1 nm. Additionally, PL excitation (PLE) spectra were registered.

One of the samples implanted to the fluence of 1×10^{17} cm^{-2} and annealed at 900°C was additionally treated in a 4% hydrofluoric acid (HF) aqueous solution at room temperature. A part of this sample was protected during the chemical treatment. The thickness of the etched layer was estimated via the comparison of the SiO_2 film color between the protected and unprotected regions of the etched sample. It is known that slight changes in the thickness of dielectric films create major shifts in their perceived color. One can estimate the thickness of the film simply by observing its color and comparing it with color charts (see, for example, Ref. [18]). In the case of SiO_2 films, a thickness variation of about 50 nm can be noticed via its color change [19].

3. Results and Discussion

3.1. Composition and Structure of "SiO_2+Sn-Based NC" Composites. Figures 1–3 display the cross-sectional TEM images of the Sn nanocluster distribution in as-implanted and annealed samples. The solid white lines in the right side of every TEM image give the depth distribution of Sn atoms as detected by RBS spectral simulations.

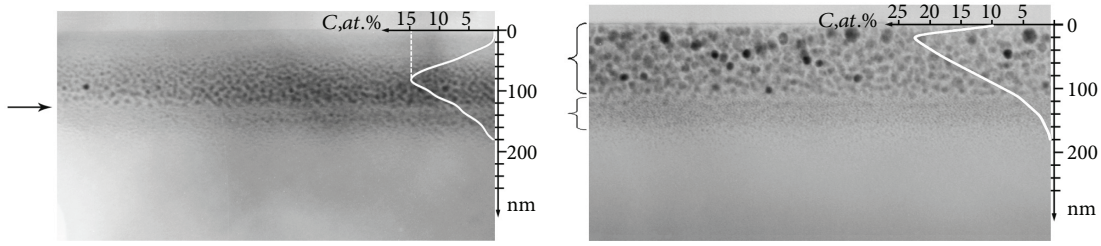

(a) (b)

FIGURE 1: XTEM images of SiO_2 (600 nm)/Si samples implanted with 200 keV Sn^+ to a fluence of 5×10^{16} cm^{-2} (a) and 1×10^{17} cm^{-2} (b). In the right of each XTEM image, the depth distribution of Sn (given in at.%) is shown as detected by RBS.

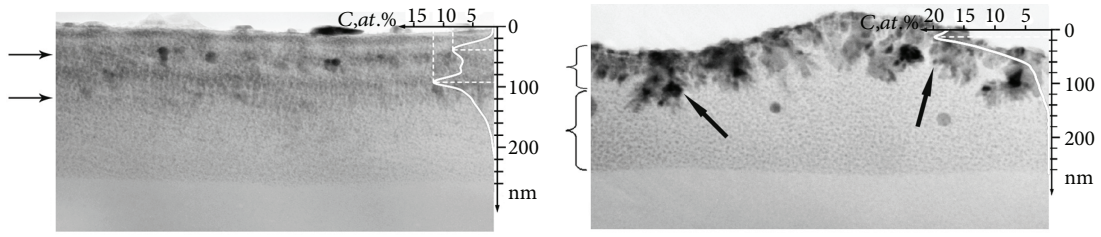

(a) (b)

FIGURE 2: XTEM images of SiO_2 (600 nm)/Si samples implanted with 200 keV Sn^+ to a fluence of 5×10^{16} cm^{-2} (a) and 1×10^{17} cm^{-2} (b) and annealed for 60 minutes at 800°C. In the right of each XTEM image, the depth distribution of Sn (given in at.%) is shown as detected by RBS. The arrows in (a) and braces in (b) are there to guide the eyes.

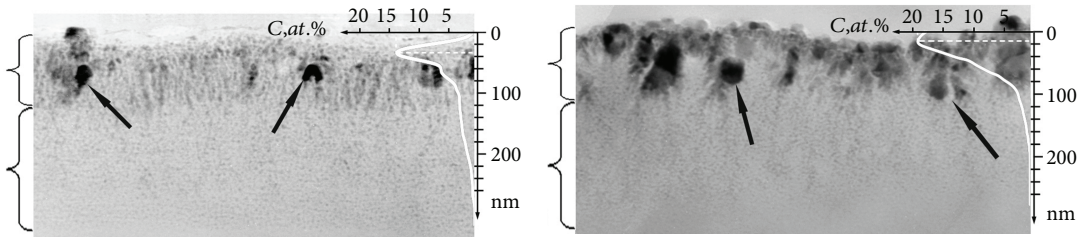

(a) (b)

FIGURE 3: XTEM images of SiO_2 (600 nm)/Si samples implanted with 200 keV Sn^+ to a fluence of 5×10^{16} cm^{-2} (a) and 1×10^{17} cm^{-2} (b) and annealed in an air atmosphere for 60 minutes at 900°C. In the right of each XTEM image, the depth distribution of Sn (given in at.%) is shown as detected by RBS. The braces are there to guide the eyes.

For the sample implanted to a fluence of 5×10^{16} cm^{-2} (Figure 1(a)), a band with small precipitates is observed at the depth of 40–180 nm. The average size of precipitates is ~5 nm. This sample is characterized by a Gaussian-like depth profile of Sn with a slight bend at the depth of 130 nm. This bend position coincides with a region depleted with Sn nanoclusters as seen in the corresponding TEM image into 120-130 nm from the surface (indicated by the arrow in Figure 1(a)).

For the sample implanted to a fluence of 1×10^{17} cm^{-2} (Figure 1(b)), a region of precipitates is located substantially closer to the surface and includes two layers differing in precipitate size. The first layer with a high density of large clusters (from 5 and up to 20 nm) is located in the depth range from the surface up to 100 nm. The second layer of small clusters (up to 2-3 nm) is observed at the depths of 130–180 nm. For the fluence of 1×10^{17} cm^{-2}, the depth of maximum impurity concentration shifts to the surface noticeably. This result is in a good agreement with the corresponding TEM image and can be caused by radiation-enhanced diffusion during high-fluence implantation. Though, even in the case of such high fluence, a comparison of the calculated Sn profile with the simulated one by SRIM (not shown here) reveals that there is no significant loss of tin in the sample.

The substantial broadening of the Sn concentration profile up to the depth of ~200 nm should be noted. Similar results of XTEM investigations of silica glasses implanted with a high fluence of Sn ions are reported in Ref. [11]. The authors of Ref. [11] have observed two layers of Sn precipitates in the as-implanted samples: a layer with large precipitates in the subsurface region and a layer with smaller clusters deeper in the sample. Precipitates (with an average size of ~9 nm) in the subsurface region (~100 nm) have been identified as metal β-Sn clusters by means of HRTEM image analysis and X-ray diffraction data. Taking this into account, we can assume that the dark contrast inclusions in the TEM

images of the as-implanted samples (Figures 1(a) and 1(b)) are precipitates of metallic β-Sn.

Heat treatment at 800°C (Figures 2(a) and 2(b)) results in a noticeable structural transformation of the implanted SiO_2 matrix as well as a substantial redistribution of the embedded impurity. For the fluence of 5×10^{16} cm^{-2} (Figure 2(a)), two layers with large Sn clusters (20-25 nm) are formed in the annealed sample at depths of 40 and 100 nm.

Simultaneously, the formation of two concentration peaks (8 and 12 at.% at the depths of ~40 and ~95 nm, respectively) in the impurity profile is observed in the same depth range. One can notice the dark particles of metal β-Sn on the sample surface. Evidently, these particles are formed due to impurity "squeezing" through the surface. For the fluence of 1×10^{17} cm^{-2} (Figure 2(b)), the thermal oxidation changes drastically the impurity depth distribution, the morphology of the subsurface region, and the distribution of nanoparticles. It is observed that a preferential impurity migration towards the surface results in the increase in Sn concentration to ~18-20 at.% within a thin subsurface layer of ~20 nm. The TEM image of this sample reveals that Sn accumulation in the subsurface zone leads to swelling and, accordingly, to a strong deformation of the subsurface region: the before-flat surface of the sample becomes irregular (wave-like) with depth differences up to 50 nm (Figure 2(b)). In addition, the formation of well-defined dendrites of large and coalesced nanoparticles of grey contrast is observed (shown by the arrows in the XTEM image of Figure 2(b)). Part of these dendrites includes dark contrast clusters surrounded with grey contrast shells. The dendrites exhibit an elongated shape, and they are oriented normally to the surface. The region of dendrites extends from the surface up to a depth of 100 nm. Beneath the dendrite region, smaller precipitates with a size of 2–4 nm are present up to a depth of 260 nm from the surface.

In order to explain the appearance of dendrites, let us discuss the possible structural rearrangements in the SiO_2 matrix with a high concentration of embedded Sn that occurs at high temperatures. The system SnO–SiO_2 was studied in Refs. [20, 21]. SnO was noted to be highly soluble (up to 70%) in the amorphous SiO_2 matrix. However, SnO is metastable and decomposes into a metallic phase (β-Sn) and SnO_2 upon heating above 550°C. The metastable silicate $SiSnO_3$ can also form. In turn, this compound decomposes at $T >$ 700°C with the formation of β-Sn, SnO_2, and SiO_2. SnO_2 has a very low solubility in SiO_2. For example, only 0.2–2.0 vol% SnO_2 can be dissolved in quartz [22]. The low solubility of SnO_2 in SiO_2 was explained by the different bond strengths of Sn and Si to O. Furthermore, tetravalent tin (Sn^{4+}) forms with O atoms, a 6-coordinate polyhedral structure, in contrast with SiO_4 groups in SiO_2 [22]. SnO_2 at a high concentration in SiO_2 can form its own random layered network of polyhedral units (based on the asymmetric building block $(SnO_4)^{6-}$), thereby destroying the three-dimensional tetrahedral structure of the SiO_2 network. Taking the above into account, we can conclude that in our experiments the existence of dendrites in the subsurface region is most probably related to the formation of the SnO_2 phase. It is worth adding that similar TEM images were reported for SiO_2 implanted with Sn ions in Ref. [11]. According to Ref. [11], a thin (~8 nm) dense SnO_2 layer was formed in the subsurface region of the implanted sample. In addition, SnO_2 nanoclusters were created all over the implanted SiO_2 layer. These clusters were visible in XTEM by Moire contrast and identified as SnO_2 nanocrystals by X-ray diffraction measurements.

An increase in the oxidation temperature to 900°C results in substantial changes of the depth impurity profile for the sample implanted to the fluence of 5×10^{16} cm^{-2} (Figure 3(a)). Tin concentration at the subsurface impurity peak at the depth of ~40 nm increases to 11 at.% while the second impurity peak at 100 nm transforms into a diffusion tail into the depth of the sample ranging up to 300 nm. Tin concentration in this region does not exceed 5 at.%. As can be seen from the corresponding TEM image, a structural rearrangement of the subsurface zone takes place. Instead of two layers with precipitates as shown in Figure 2(a), a dense layer of precipitates with embedded large dark particles is formed in the subsurface region (shown by the arrows in the XTEM image of Figure 3(a)). The thickness of this layer is ~120 nm. For the sample implanted to the fluence of 1×10^{17} cm^{-2} and annealed at 900°C, there is no noticeable change in the Sn concentration profile in comparison with that obtained after oxidation at 800°C (Figure 3(b)). The TEM image of that sample does not show any noticeable structural transformations, too. It is worth mentioning the interesting feature in the TEM images of the samples implanted to both fluences and heated at 900°C, namely, the existence of the uniform distribution of nanoclusters with a size of several nanometers at depths from 100 to 300 nm (Figures 3(a) and 3(b)). This depth region is depleted with impurity in comparison with the subsurface SiO_2 layer and is characterized with Sn concentration < 5 at.%. Probably, when the impurity concentration is low, Sn atom diffusion to the SiO_2/Si interface begins to prevail over Sn precipitation. That is why, small Sn-based clusters can be formed deeper in the SiO_2 layer than one expects from the analysis of the initial as-implanted Sn concentration profiles. A similar effect was reported in Ref. [3] devoted to the study of Sn precipitation in the SiO_2 matrix with relatively low concentration of embedded Sn atoms. The SiO_2 (180 nm)/Si samples were implanted with tin ions (200 keV, 1.5×10^{16} cm^{-2}) corresponding to the Gaussian-type Sn concentration-depth profile with peak concentrations ≈ 3 at.% formed at the depth of 90 nm in the SiO_2 matrix. According to the TEM data, Sn nanoclusters with the average size of 2.2 nm were formed in the SiO_2 layer after annealing at 900°C in vacuum. These precipitates were distributed uniformly in the volume of the SiO_2 matrix. The authors of Ref. [3] concluded that such distribution arises probably due to the absence of trapping centers, allowing the Sn diffusion from the original as-implanted Gaussian-type profile towards the surface and to the SiO_2/Si interface. As a consequence, the formation of large Sn clusters and SnO_x shells around them was not observed.

To study the phase composition of the annealed samples, "plan-view" TEM and electron microdiffraction investigations were carried out (Figure 4). Annealing of samples at 800°C results in the formation of precipitates with sizes ranging from 2 to 30 nm (Figure 4(a)). Besides, specific contrast

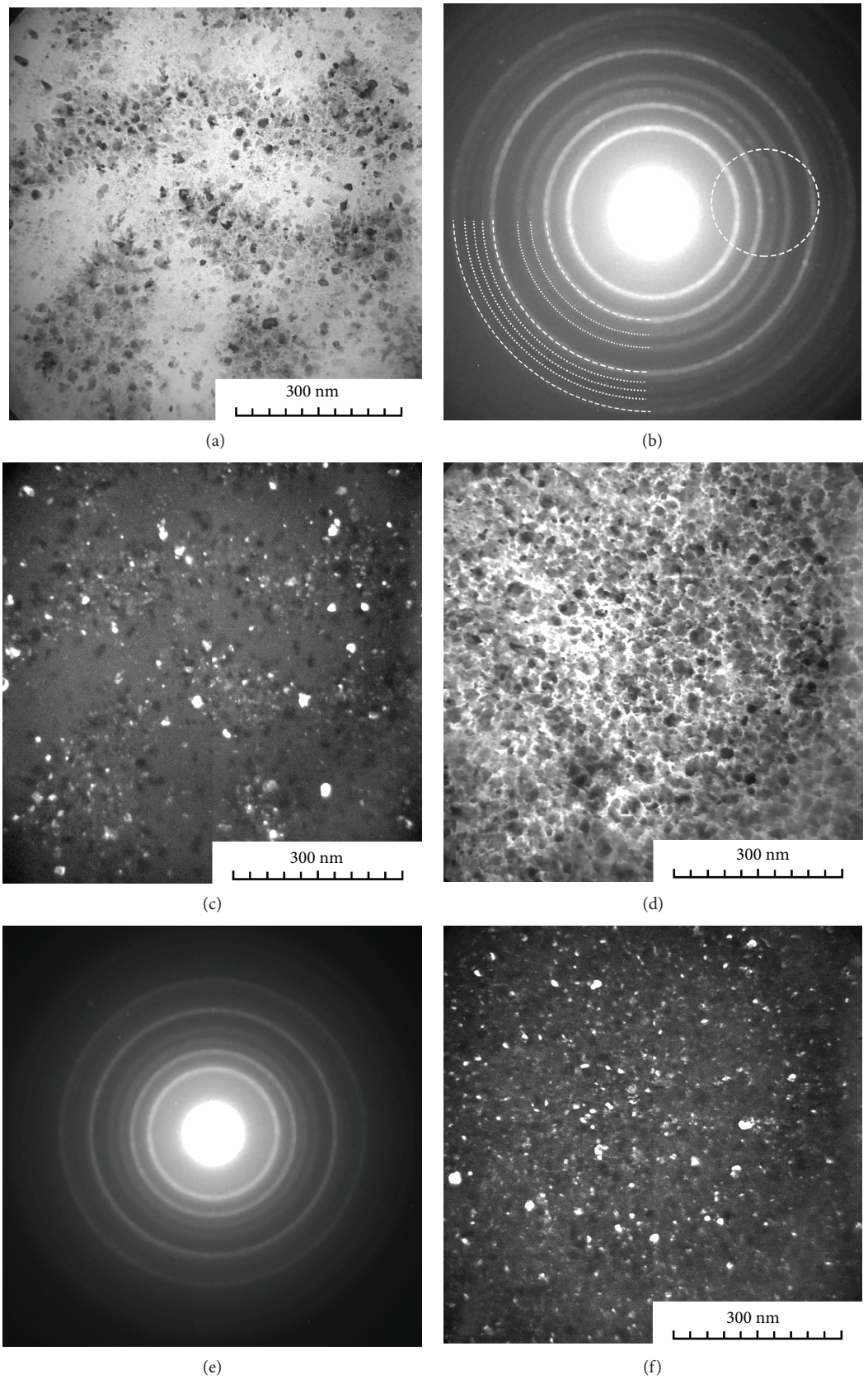

FIGURE 4: Bright-field (a, d) and dark-field TEM images (c, f) and electron diffraction patterns (b, e) of SiO_2 (600 nm)/Si samples implanted with 200 keV Sn^+ to a fluence of 1×10^{17} cm^{-2} and annealed at 800 (a, b, c) and 900°C (d, e, f).

(alternating curved light and dark stripes) is observed in the images. An annealing temperature increase (up to 900°C) results in the reduction of this contrast and cluster size increase (up to 50 nm) (Figure 4(d)). The crystal structure of the clusters is confirmed by the presence of narrow rings in diffraction patterns (Figures 4(b) and 4(e)) and their "light-up" on dark-field TEM micrographs (Figures 4(c) and 4(f)). These dark-field images were formed by the diffracted beams from the area shown in Figure 4(b). The values of interplanar spacing obtained from electron microdiffraction patterns were compared with the American X-ray ICDD PDF-2 database [23]. We do not exclude the formation of various tin phases (β-Sn, SnO, and $SiSnO_3$). However, the electron diffraction data have shown that the SnO_2 phase is the most probable (see Table 1).

3.2. Photoluminescence of "SiO_2+Sn-Based NC" Composites. Figure 5 depicts the PL spectra of the as-implanted samples and the spectra of implanted samples after annealing at 800°C and 900°C. The spectra of the as-implanted samples are characterized by a weak emission with maximum at the blue range (2.9 eV). The PL intensity significantly increases after thermal oxidation. A broad band of complicated shape dominates in all spectra. For the annealed samples, the narrowest and most intense band is located at the violet spectral range (~ 3.1 eV). There are other broad weak bands in the green-orange spectral range of 1.8–2.9 eV. It should be noted that the intensity of violet band with respect to the intensity of emission in the green-orange range increases with increasing ion fluence and annealing temperature.

Obviously, the complicated shape of the PL bands of Sn-implanted SiO_2/Si samples is due to a number of radiative centers. The nature of the narrow band in the violet spectral range (~3.1 eV) is the most intriguing one. It was mentioned above that the appearance of the strong PL at 3.18–2.97 eV is characteristic of bulk and nanostructured SnO_2 [11, 24–27]. The energy gap of bulk SnO_2 is 3.6 eV, and the Bohr radius of an exciton for SnO_2 amounts to 2.7 nm. This value (2.7 nm) is significantly lower than the size of the precipitates created in SiO_2 in our experiment. Hence, it is doubtful to expect the quantum confinement displayed in the PL spectra. At the same time, the energy of the exciting laser light (3.81 eV) used for PL recording in our experiment is quite enough to excite the band edge emission of SnO_2. Moreover, for the understanding of the observed PL spectra, one has to take the existence of a high concentration of oxygen vacancies in SnO_2 into account. This defect is the most common defect in nanostructured SnO_2 and in fact defines its electrical (n-type of conductivity) and optical properties. The oxygen vacancy in SnO_2 forms a donor defect level below the conduction band edge [11, 28]. Therefore, the origin of the emission at ~3.1 eV from SnO_2-based composites can be considered the edge band emission broadened due to excitons bounded to neutral donors [25] as well as a recombination of electrons located at the oxygen vacancies with a hole from the valence band [11, 24–27]. As noted in Ref. [29], a high oxygen vacancy concentration is a characteristic feature for Sn nanospheres coated with SnO_2 shells. Taking this into account, we can ascribe the observed intense PL peak at

Table 1: Comparison of the interplanar distances (d_{hkl}) of β-Sn and SnO_2 and the calculated ones from the electron diffraction pattern.

No. of diffraction rings	Calculated interplanar distances from electron diffraction data, Å	Interplanar distances and Miller indices, Å (hkl) [23]	
		β-Sn	SnO_2
1	3.318	—	3.349 (110)
2	2.632	2.608 (210)	2.643 (101)
3	2.306	—	2.308 (111)
4	2.086	2.062 (220)	2.118 (210)
5	1.755	1.730 (221)	1.764 (211)
6	1.673	1.659 (301)	1.675 (220)
7	1.577	1.590 (002)	1.579 (300)
8	1.488	1.484 (112)	1.482 (221)
9	1.410	—	1.415 (301)

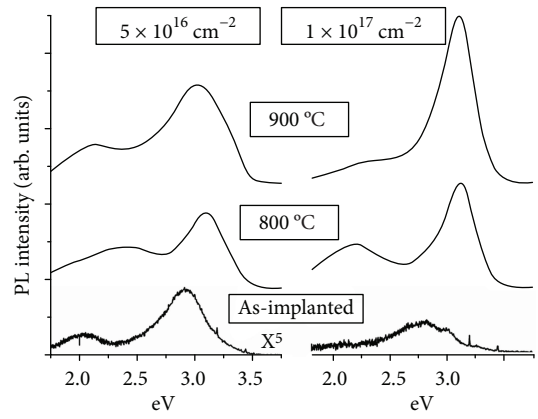

Figure 5: PL spectra of the implanted samples of SiO_2 (600 nm)/Si before and after annealing.

~3.1 eV to the formation of SnO_2 precipitates and/or SnO_2 shells surrounding Sn nanoclusters.

However, an alternative explanation of the origin of the "violet" band is possible. This feature can originate from molecular-like centers [1–3, 5, 30] corresponding to Sn-related oxygen-deficient centers (ODC) in the SiO_2 matrix itself. According to Ref. [5], the PL band at 3.15 eV in Sn-doped silica samples can be excited by light in the near ultraviolet region (like in our experiment) and caused by intercombination transition ($T_1 \rightarrow S_0$). Nevertheless, attribution of the violet band to Sn-ODC in the case of our samples is illegitimate. Firstly, it has been found that high-temperature annealing for an hour results in a significant violet PL increase. If the nature of such PL increase is related to twofold coordinated Sn atoms, we should suppose the increase in concentration of twofold coordinated Sn atoms dissolved in the silica matrix after annealing. However, in conditions of our experiment, it is unlikely. Secondly, the registered PLE spectrum at PL maximum (Figure 6) exhibits one band with maximum at 3.4 eV. It does not coincide with the maximum of excitation spectra at 3.7 eV in near UV and does not exhibit band in middle UV as observed in the PLE spectrum

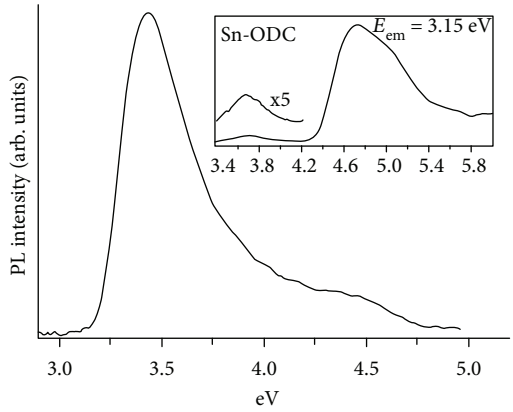

FIGURE 6: PLE spectrum of the SiO_2 (600 nm)/Si samples implanted with 200 keV Sn^+ to a fluence of 1×10^{17} cm^{-2} and annealed in an air atmosphere for 60 minutes at 900°C. The inset shows the PLE spectrum for the emission at 3.15 eV ($T_1 \rightarrow S_0$) attributed to twofold coordinated Sn atoms in SiO_2 from Ref. [5].

for violet band (3.15 eV) attributed to Sn-ODC [5] (inset in Figure 6). Thus, the violet band at 3.1 eV can be attributed to the SnO_2 phase (in the form of separate clusters or Sn cluster shells). It should be noted that the excitation band is at 3.4 eV (lower than the SnO_2 band edge, 3.6 eV) and its edge on the low-energy side is not steep enough. It is additionally proven that effective energy gap contraction is probably due to structural imperfection of synthesized nanocrystals.

There is a still open question asking which synthesized nanoclusters (large ones and dendrites near the surface or small regular nanoprecipitates in more deep regions of the SiO_2 film) play a crucial role in violet PL. In order to shed more light on this question, we have carried out an additional etching experiment for the sample implanted to the fluence of 1×10^{17} cm^{-2} and subsequently annealed at 900°C. The aim of this experiment was to remove a thin subsurface layer of nearly 50 nm. Figure 7 shows the PL spectra of the unetched sample and the sample with the upper layer being etched away. As can be seen from Figure 7, the etch procedure results in the decrease in intensity of violet band at 3.1 eV. Therefore, the large clusters formed in the subsurface layer with high Sn concentration (~20%) are more responsible for the emission in the violet spectral range. Simultaneously, one can see an increase in the intensity in the spectral range of 1.8–2.9 eV. Most probably, the weak and broad band in this spectral range originates from defects in both SnO_2 (Sn and O interstitials, dangling bonds, or oxygen vacancies) [5, 9, 24, 25, 27, 31] and SiO_2 matrix [24, 30, 32, 33] and also from the formation of the SnO_x phase [34]. It is noncontradictory, and the contribution of defects in the SiO_2 matrix and SnO_x phase in emission would be higher from the more deep layers due to lower concentration of Sn atoms and oxygen atoms diffused from air.

Interestingly, for both fluences, the ratio of the emission intensity in the range of 1.8–2.9 eV to the emission intensity at 3.1 eV decreases when increasing the oxidation temperature from 800°C to 900°C. It can be explained by improving

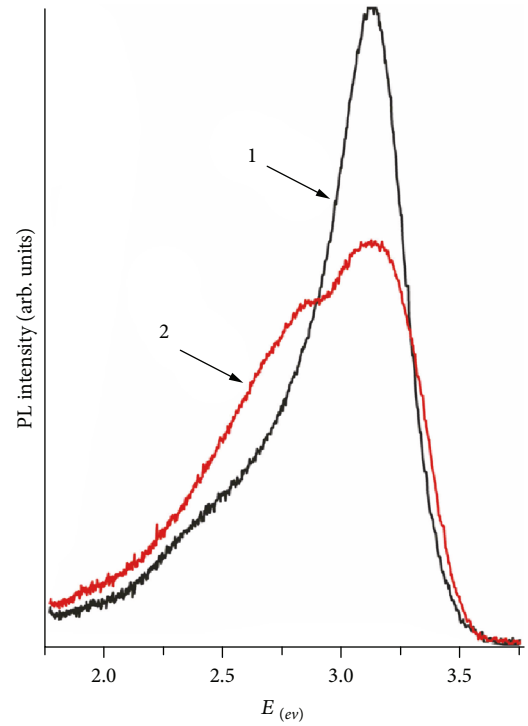

FIGURE 7: PL spectra of the SiO_2 samples implanted with Sn ion (1×10^{17} cm^{-2}) and annealed at 900°C before (1) and after (2) etching of the upper layer.

the crystallinity of the tin oxide nanoparticles and reducing the intrinsic defect concentration.

There is one peculiarity which additionally proves the formation of the SnO_2 phase. Earlier, we estimated that the etch velocity of SiO_2 layers thermally grown on Si substrates amounted to ≈18 nm/min [35]. Hence, one could expect that the thickness of the SiO_2 layer removed during 3 min etching should be about 50 nm, and it could be noticed via the film color change between the protected and unprotected regions of the etched sample. However, we have noticed the film color change only after additional fourfold repetition of the 3 min treatment in 4% HF (the etching total duration was 15 min). At the same time, it is known that SnO_2 films practically do not dissolve in HF solutions (see, for example, [36]). Hence, we can suggest the existence of the subsurface layer of the low-soluble SnO_2 phase also from the low etching rate.

4. Conclusions

The embedded impurity distribution, structural and light emission properties of "SiO_2+Sn-based NC" composites created via high-fluence tin ion implantation, and thermal oxidation in air were studied using RBS, XTEM, and PL. A strict correspondence of Sn concentration profiles and tin-based particle distribution in the SiO_2 layer has been found. Nanoclusters of β-Sn (diameter ranging from 2 to 10 nm) are formed in a 180 nm thick layer of the SiO_2 layer after ion implantation. Upon heat treatment, the diffusion of

embedded tin impurity to the surface and into the depth of the SiO_2 layer is observed. For the sample implanted to a fluence of 1×10^{17} cm^{-2} and heated at 800°C, the impurity accumulation in the subsurface zone leads to swelling and strong deformation: the originally flat surface of the sample becomes irregular (wave-like). The dendrites composed of large and coalesced nanoparticles of grey contrast are created in the subsurface region of the implanted SiO_2 matrix. The appearance of dendrites is most probably due to the formation of the SnO_2 phase. For the samples implanted to both fluences and heated at 900°C, beneath the layer of big dark particles surrounded by grey contrast shells, a uniform distribution of nanoclusters with a size of several nanometers at the depths from 100 to 300 nm is observed. This depth region is depleted with impurity in comparison with the subsurface SiO_2 layer (Sn concentration < 5 at.%). The formation of the SnO_2 phase in annealed films was proven by diffraction patterns.

The PL spectra of the as-implanted samples are characterized by a weak emission with maximum at the blue range (2.9 eV). The PL intensity significantly increases after the thermal oxidation. The narrowest and most intense PL band has a maximum at ~3.1 eV. Its intensity increases with increasing fluence and annealing temperature. We conclude that this emission can be assigned to the formation of the SnO_2 phase (in the form of separate clusters or shells of Sn clusters) in the subsurface region of the implanted SiO_2 matrix.

Data Availability

The data used to support the findings of this study are available from the corresponding author upon request.

Conflicts of Interest

The authors declare that they have no conflicts of interest.

Acknowledgments

This work was partly supported by the Belarusian Republican Foundation for Fundamental Research (Grant F17KIG-005).

References

[1] L. Rebohle, J. von Borany, H. Fröb, and W. Skorupa, "Blue photo- and electroluminescence of silicon dioxide layers ion-implanted with group IV elements," *Applied Physics B: Lasers and Optics*, vol. 71, no. 2, pp. 131–151, 2000.

[2] S. Spiga, R. Mantovan, M. Fanciulli et al., "Local structure of Sn implanted in thinSiO2films," *Physical Review B*, vol. 68, no. 20, article 205419, 2003.

[3] J. M. J. Lopes, F. C. Zawislak, P. F. P. Fichtner, F. C. Lovey, and A. M. Condo, "Effect of annealing atmosphere on the structure and luminescence of Sn-implanted SiO2 layers," *Applied Physics Letters*, vol. 86, no. 2, article 23101, 2005.

[4] J. M. J. Lopes, F. Kremer, P. F. P. Fichtner, and F. C. Zawislak, "Correlation between structural evolution and photoluminescence of Sn nanoclusters in SiO_2 layers," *Nuclear Instruments and Methods in Physics Research Section B: Beam Interactions with Materials and Atoms*, vol. 242, no. 1-2, pp. 157–160, 2006.

[5] L. Skuja, "Isoelectronic series of twofold coordinated Si, Ge, and Sn atoms in glassy SiO2: a luminescence study," *Journal of Non-Crystalline Solids*, vol. 149, no. 1-2, pp. 77–95, 1992.

[6] H.-J. Fitting, "How to make silica luminescent?," *Journal of Luminescence*, vol. 129, no. 12, pp. 1488–1492, 2009.

[7] Y. Wang, J. He, P. Barua et al., "Ultraviolet photoluminescence in Gd-doped silica and phosphosilicate fibers," *APL Photonics*, vol. 2, no. 4, 2017.

[8] O. V. Laguta, H. E. Hamzaoui, M. Bouazaoui, V. B. Arion, and I. M. Razdobreev, "On the nature of photoluminescence in bismuth-doped silica glass," *Scientific Reports*, vol. 7, no. 1, p. 3178, 2017.

[9] X. Zhang, R. Chen, P. Wang et al., "A soft chemistry-based route to enhanced photoluminescence of terbium ions and tin oxide nanocrystals codoped silica thin films," *Applied Surface Science*, vol. 452, pp. 96–101, 2018.

[10] X. Xiang, X. T. Zu, S. Zhu et al., "Photoluminescence of SnO_2 nanoparticles embedded in Al2O3," *Journal of Physics D: Applied Physics*, vol. 41, no. 22, article 225102, 2008.

[11] M. A. Tagliente, V. Bello, G. Pellegrini, G. Mattei, P. Mazzoldi, and M. Massaro, "SnO2 nanoparticles embedded in silica by ion implantation followed by thermal oxidation," *Journal of Applied Physics*, vol. 106, no. 10, article 104304, 2009.

[12] D. A. Zatsepin, A. F. Zatsepin, D. W. Boukhvalov, E. Z. Kurmaev, and N. V. Gavrilov, "Sn-loss effect in a Sn-implanted a -SiO 2 host-matrix after thermal annealing: a combined XPS, PL, and DFT study," *Applied Surface Science*, vol. 367, pp. 320–326, 2016.

[13] C. Gu, J. Huang, N. Ni, M. Li, and J. Liu, "Detection of DNA hybridization based on SnO_2 nanomaterial enhanced fluorescence," *Journal of Physics D: Applied Physics*, vol. 41, no. 17, article 175103, 2008.

[14] P. K. Kuiri, H. P. Lenka, J. Ghatak, G. Sahu, B. Joseph, and D. P. Mahapatra, "Formation and growth of SnO_2 nanoparticles in silica glass by Sn implantation and annealing," *Journal of Applied Physics*, vol. 102, no. 2, article 24315, 2007.

[15] T. W. Kim, D. U. Lee, and Y. S. Yoon, "Microstructural, electrical, and optical properties of SnO2 nanocrystalline thin films grown on InP (100) substrates for applications as gas sensor devices," *Journal of Applied Physics*, vol. 88, no. 6, pp. 3759–3761, 2000.

[16] J. Jeong, S.-P. Choi, C. I. Chang et al., "Photoluminescence properties of SnO_2 thin films grown by thermal CVD," *Solid State Communications*, vol. 127, no. 9-10, pp. 595–597, 2003.

[17] L. Z. Liu, X. L. Wu, J. Q. Xu, T. H. Li, J. C. Shen, and P. K. Chu, "Oxygen-vacancy and depth-dependent violet double-peak photoluminescence from ultrathin cuboid SnO_2 nanocrystals," *Applied Physics Letters*, vol. 100, no. 12, article 121903, 2012.

[18] J. Henrie, S. Kellis, S. M. Schultz, and A. Hawkins, "Electronic color charts for dielectric films on silicon," *Optics Express*, vol. 12, no. 7, p. 1464, 2004.

[19] S. M. Sze, *Physics of Semiconductor Devices*, J. Wiley & Sons, Ann Arbor, Michigan, 1981.

[20] M. M. Karim and D. Holland, "Physical properties of glasses in the system SnO-SiO_2," *Physics and Chemistry of Glasses*, vol. 36, p. 206, 1995.

[21] J. F. Bent, A. C. Hannon, D. Holland, and M. M. A. Karim, "The structure of tin silicate glasses," *Journal of Non-Crystalline Solids*, vol. 232-234, pp. 300–308, 1998.

[22] M. B. Volf, *Chemical Approach to Glass*, Elsevier, Oxford, UK, 1984.

[23] ICDD PDF-2 (Database), *American Society for Testing and Materials (ASTM)*, Soorya Kabekkodu, Ed., International Centre for Diffraction Data, Newtown Square, PA, USA, 1997.

[24] T.-Y. Wei, S.-Y. Lu, and Y.-C. Chang, "Rich photoluminescence emission of SnO_2–SiO_2 composite aerogels prepared with a co-fed precursor sol–gel process," *Journal of the Chinese Institute of Chemical Engineers*, vol. 38, no. 5-6, pp. 477–481, 2007.

[25] R. Chen, G. Z. Xing, J. Gao, Z. Zhang, T. Wu, and H. D. Sun, "Characteristics of ultraviolet photoluminescence from high quality tin oxide nanowires," *Applied Physics Letters*, vol. 95, no. 6, article 61908, 2009.

[26] L. C. Nehru, V. Swaminathan, and C. Sanjeeviraja, "Photoluminescence studies on nanocrystalline tin oxide powder for optoelectronic devices," *American Journal of Materials Science*, vol. 2, no. 2, pp. 6–10, 2012.

[27] A. R. Babar, S. S. Shinde, A. V. Moholkar, C. H. Bhosale, J. H. Kim, and K. Y. Rajpure, "Physical properties of sprayed antimony doped tin oxide thin films: the role of thickness," *Journal of Semiconductors*, vol. 32, no. 5, article 53001, 2011.

[28] S.-S. Chang and D. K. Park, "Novel Sn powder preparation by spark processing and luminescence properties," *Materials Science and Engineering B*, vol. 95, no. 1, pp. 55–60, 2002.

[29] S. Li, X. Zhong, Y. Song et al., "Controlled hybridization of Sn–SnO_2 nanoparticles via simple-programmed microfluidic processes for tunable ultraviolet and blue emissions," *Journal of Materials Chemistry C*, vol. 2, no. 36, pp. 7687–7694, 2014.

[30] A. Cannizzo, S. Agnello, M. Cannas, N. Chiodini, M. Leone, and A. Paleari, "Temperature dependence of luminescence decay in Sn-doped silica," *Journal of Non-Crystalline Solids*, vol. 351, no. 21-23, pp. 1937–1940, 2005.

[31] N. F. Santos, J. Rodrigues, T. Holz et al., "Luminescence studies on $SnO_2$and SnO_2:Eu nanocrystals grown by laser assisted flow deposition," *Physical Chemistry Chemical Physics*, vol. 17, no. 20, pp. 13512–13519, 2015.

[32] L.-S. Liao, X.-M. Bao, N.-S. Li, X.-Q. Zheng, and N.-B. Min, "Blue-, green-, and red-light emission from Si+-implanted thermal SiO2 films on crystalline silicon," *Journal of Luminescence*, vol. 68, no. 2-4, pp. 199–204, 1996.

[33] R. Tohmon, Y. Shimogaichi, H. Mizuno, Y. Ohki, K. Nagasawa, and Y. Hama, "2.7-eV luminescence in as-manufactured high-purity silica glass," *Physical Review Letters*, vol. 62, no. 12, pp. 1388–1391, 1989.

[34] H. H. An, S. J. Lee, S. H. Baek et al., "Effect of plasma etching on photoluminescence of SnO_x/Sn nanoparticles deposited on DOPC lipid membrane," *Journal of Colloid and Interface Science*, vol. 368, no. 1, pp. 257–262, 2012.

[35] L. A. Vlasukova, F. F. Komarov, V. N. Yuvchenko et al., "Threshold and criterion for ion track etching in SiO_2 layers grown on Si," *Vacuum*, vol. 105, pp. 107–110, 2014.

[36] C. E. Morosanu, *Thin Films by Chemical Vapour Deposition*, Elsevier, Oxford, 1990.

Hindawi
Journal of Nanomaterials
Volume 2019, Article ID 4184351, 8 pages
https://doi.org/10.1155/2019/4184351

Research Article

Characterization of Nanosilica/Low-Density Polyethylene Nanocomposite Materials

Malek Alghdeir, Khaled Mayya, and Mohamed Dib

Applied Physics Department, Higher Institute for Applied Sciences and Technology, Damascus, Syria

Correspondence should be addressed to Malek Alghdeir; malekghdeir@yahoo.com

Received 2 October 2018; Revised 22 November 2018; Accepted 19 December 2018; Published 20 March 2019

Guest Editor: Chandragiri V. Reddy

Six ratios of nanosilica particles were employed to fabricate low-density polyethylene (LDPE) composites using melt mixing and hot molding methods. Several composite films with different ratios (0.5, 1, 2.5, 5, 7.5, and 10 wt%) of SiO_2 were prepared. The obtained composite films were identified and characterized by Fourier-transform infrared spectroscopy (FTIR) and ultraviolet-visible spectroscopy (UV-VIS). At a specific mixing ratio, far infrared radiation transmittance was prohibited while the ultraviolet-visible transmittance is allowed; this will be explained in detail. Optical measurements show that the composite films prevent the transmission of IR radiation near 9 μm and allow UV-VIS transmission during sun-shining time. The mechanical behaviour of a nanosilica-reinforced LDPE composite was studied using tensile tests. The addition of 1 wt% nanosilica has successfully enhanced the mechanical properties of the LDPE material.

1. Introduction

Polymeric materials are widely used in food packaging and in greenhouses. Typical examples of such materials are polypropylene (PP), polyethylene (PE), and polyethylene terephthalate (PET) [1, 2].

During the past years, much effort has been devoted to polymer nanocomposites [3]. Polymer nanocomposites often show excellent mechanical properties compared to the traditional composites at a lower loading of the nanoparticles [4]. So far, a few researches have studied the effects of different nanoparticles on the performances of composite materials such as nanosilica [3]. The excellent performance of silica film has attracted attention in academia and industry due to its antiresistance, hardness, corrosion resistance [5], dielectric properties [6], optical transparency, etc. [7]. Silica as a thin film is widely used to improve the surface properties of materials. This is why silica thin films are used in many fields as in antireflection coating film field [8]. In the packaging industry, silica films are used as barrier layers in polymer packaging materials. Most of the modern packaging materials do not provide an efficient barrier against the permeation of gases. This leads to food and drinks getting rotten quickly. Because of this, a silica film deposited on the surface of the polymer packaging becomes popular and indispensable. Besides, silica films can be also used as corrosion protective layers of metals. Because of the universal application of silicon dioxide films in various fields, the preparation of silica with high quality is always an important aim of scientific research [9].

Lately, a number of different barrier technologies were being developed. Theoretically, a barrier function can be inserted into a plastic-based material via two different means: either by mixing a barrier material into the base polymer or by coating a layer of the barrier material on the polymer surface [10, 11].

The traditional method of preparing polymer/silica composites was direct mixing of the silica into the polymer. The mixing could be done by melt blending and solution blending. The main difficulty in the mixing process is the effective dispersion of the silica nanoparticles in the polymer matrix, because they usually tend to agglomerate [12].

This work represents the results of optical and thermal experiments on LDPE mixed with nanosilica particles at different ratios (0.5, 1, 2.5, 5, 7.5, and 10 wt%). The aim is to achieve a nanocomposite that prevents the transmittance

of IR radiation and allows the transmittance of UV-VIS, so that most of the thermal radiation of the ground and plants in the greenhouse is conserved. The mechanical properties of the nanocomposite, such as the tensile strength, the elongation at break, and Young's modulus, were also evaluated and discussed.

By studying the blackbody thermal radiation, all objects with a temperature above absolute zero were shown to emit energy in the form of electromagnetic radiation. A blackbody is a theoretical or model body which absorbs all radiation falling on it. It is a hypothetical object which is a "perfect" absorber and a "perfect" emitter of radiation. The electromagnetic radiation emitted by a blackbody has a specific spectrum and intensity that depends only on the body's temperature; the thermal radiation spontaneously emitted by ordinary objects, land, and plants, for example, can be approximated as blackbody radiation. Figure 1 shows the blackbody radiation spectrum at 273, 293, 313, 333, 373, 393, 413, 433, and 453 K. We are interested in the vicinity of 10 μm (9 to 11), because at the temperatures near 0°C, (273 K) the thermal radiation from the ground is the maximum at 10 μm, while at the temperature of 30°C (303 K), the thermal radiation from the ground is the maximum at 9.5 μm [9].

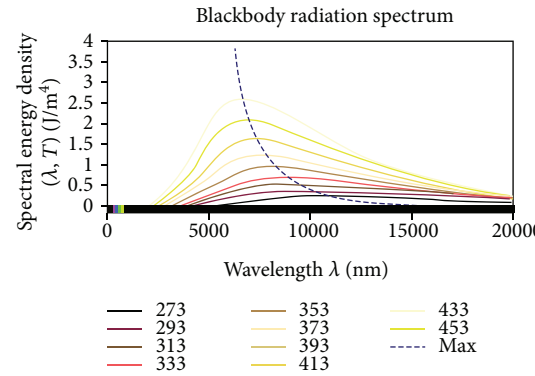

Figure 1: Blackbody radiation spectra at 273, 293, 313, 333, 373, 393, 413, 433, and 453 K. This figure was reproduced from Alghdeir et al. [9] (under the Creative Commons Attribution License/public domain).

2. Material and Methods

2.1. Materials. Low-density polyethylene (LDPE), a thermoplastic made from an ethylene monomer with a density of 0.922 g/cm^3, was purchased from Saudi Basic Industries Corporation (SABIC). High-purity fumed nanosilica (purity > 99%) with an average particle size of ~12 nm and the trademark of A200 was obtained from Evonik Degussa AG (Germany). Table 1 shows the basic physical and chemical properties of the fumed nanosilica used in the present work.

Table 1: Basic physical and chemical properties of fumed nanosilica.

Properties	Value
Physical state	Solid
Color	White
Form	Powder
pH	3.7-4.5
Surface area	200 ± 25 (m^2/g)
Melting point/range	Approx. 1700°C
Density	Approx. 2.2 g/cm^3
Water solubility	>1 mg/l
Thermal decomposition	>2000°C
Loss on drying	≤1.5% (2 hours at 105°C)
SiO_2 content based on ignited material	>99.8%

2.2. Sample Preparation. Samples were prepared by blending LDPE and silica with different ratios (0.5, 1, 2.5, 5, 7.5, and 10 wt%). The different nanosilica ratios were mechanically mixed with the LDPE granules at a processing temperature of 130°C and a speed of 50 rpm for 10 min using the internal mixer (Brabender Plasti-Corder PL-2200, W50, Germany). Films with dimensions of 10 cm × 10 cm × 120 μm of the neat LDPE and nanocomposites were obtained by a hot-press method at 140°C and under 50 bar. For the mechanical behaviour tests of the composite, other plates were prepared using the abovementioned procedure with a thickness of 1.8 ± 0.1 mm.

Table 2: Dimensions of samples for tensile test.

Specifications	Dimensions (mm)
Sample length	75
Display ends	12.5 ± 1
Length of the active part	25 ± 1
Display the effective part	4 ± 0.1
External radius	8 ± 0.5
Internal radius	12.5 ± 1

3. Results and Discussion

3.1. Study of Mechanical Properties. For the studies of mechanical properties, the test specimens were molded and cut according to the dimensions specified in Table 2.

The tensile test was achieved using a traction-compression machine (Adamel Lhomargy DY34) under atmospheric conditions. For each ratio, including the neat LDPE (the control sample), five samples were tested and their values were averaged. The tensile tests were carried at a speed of 5 mm/min. Table 3 shows a summary of the tensile data for the control sample and the samples of six composites.

Stress-strain curves from tensile tests for LDPE/silica nanocomposites are shown in Figure 2. It can be noticed that the stress at break gradually increases with the increase of up to 1 wt% of the silica ratio. This result suggests that the nanosilica particles would reinforce stress and cause the increase of the tensile strength of the nanocomposite.

Table 3: Summary of tensile data for the control sample and six composites of LDPE.

Material	Property	Sample no. 1	Sample no. 2	Sample no. 3	Sample no. 4	Sample no. 5	Average	Std. Dev.
Neat LDPE (control sample)	Maximum load (*N*)	60	60	50	60	60	58	4.47
	Tensile strength (MPa)	8.40	8.42	7.13	8.67	8.28	8.18	0.60
	% elongation at break	190	230	323	258	248	250	48
	Modulus of elasticity (MPa)	66.64	56.73	67.53	69.45	62.01	64.47	5.1
LDPE 0.5 wt% SiO_2	Maximum load (N)	60	60	60	60	60	60	0
	Tensile strength (MPa)	8.13	8.39	8.24	8.28	8.35	8.27	0.1
	% elongation at break	263	394	276	311	293	307	52
	Modulus of elasticity (MPa)	104	102	98	81	92	95.4	9.2
LDPE 1 wt% SiO_2	Maximum load (N)	60	60	60	60	60	60	0
	Tensile strength (MPa)	8.83	8.75	8.82	8.65	8.89	8.78	0.09
	% elongation at break	410	355	377	410	318	374	40
	Modulus of elasticity (MPa)	95	90	93	96	68	88.4	12
LDPE 2.5 wt% SiO_2	Maximum load (N)	60	60	60	60	60	60	0
	Tensile strength (MPa)	8.46	8.67	8.82	8.48	8.80	8.64	0.17
	% elongation at break	260	444	273	456	379	362	92
	Modulus of elasticity (MPa)	99	96	94	99	92	96	3.5
LDPE 5 wt% SiO_2	Maximum load (N)	60	60	60	60	60	60	0
	Tensile strength (MPa)	8.34	8.17	8.39	8.32	8.16	8.27	0.10
	% elongation at break	142	201	229	338	247	231	71
	Modulus of elasticity (MPa)	105	118	135	124	128	122	11
LDPE 7.5 wt% SiO_2	Maximum load (N)	60	60	60	60	60	60	0
	Tensile strength (MPa)	8.37	8.43	8.36	8.24	8.38	8.35	0.07
	% elongation at break	242	231	222	300	270	253	31
	Modulus of elasticity (MPa)	106	139	110	109	96	112	16
LDPE 10 wt% SiO_2	Maximum load (N)	60	60	60	60	60	60	0
	Tensile strength (MPa)	8.43	8.04	8.51	8.48	8.47	8.38	0.19
	% elongation at break	139	126	95	116	114	118	16
	Modulus of elasticity (MPa)	104	129	95	141	141	122	21

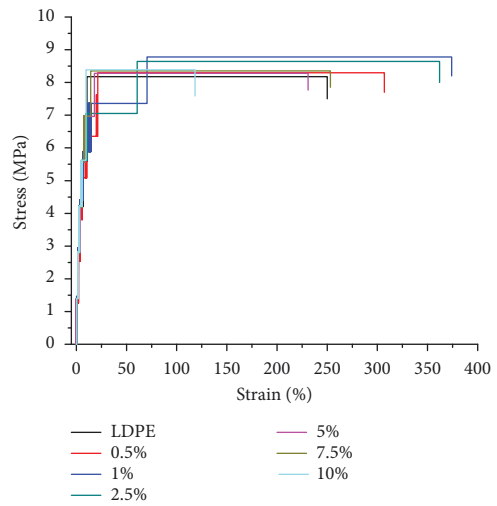

Figure 2: Typical stress-strain curves of neat LDPE and LDPE/silica nanocomposites.

Figure 2 also shows that the elongation at break values of the nanocomposite greatly increases with the nanosilica particle ratio that is also up to 1 wt%. This can be explained by the increase in the surface bonding between the molecules of the polymer, when the nanosilica particles are added to it. Similar results have been obtained with other oxides [13].

Beyond 1 wt%, it can be noticed from Figure 2 that the values of both the tensile strength and elongation at break of the nanocomposite decrease with the increase in the nanosilica particle ratio incorporated. This result can be explained by the agglomeration of the nanosilica particles within the polymer matrix. This agglomeration can even be seen with the naked eye in the form of white spots within the samples (see Figure 3).

Figure 4 shows the variations in Young's modulus of the nanocomposite with the nanosilica particle ratios. The elongation at break was also added to the figure. It can be noticed that Young's modulus increases with the nanosilica particle ratios of up to 5 wt%. Beyond this value, we notice that the values of Young's modulus remain practically

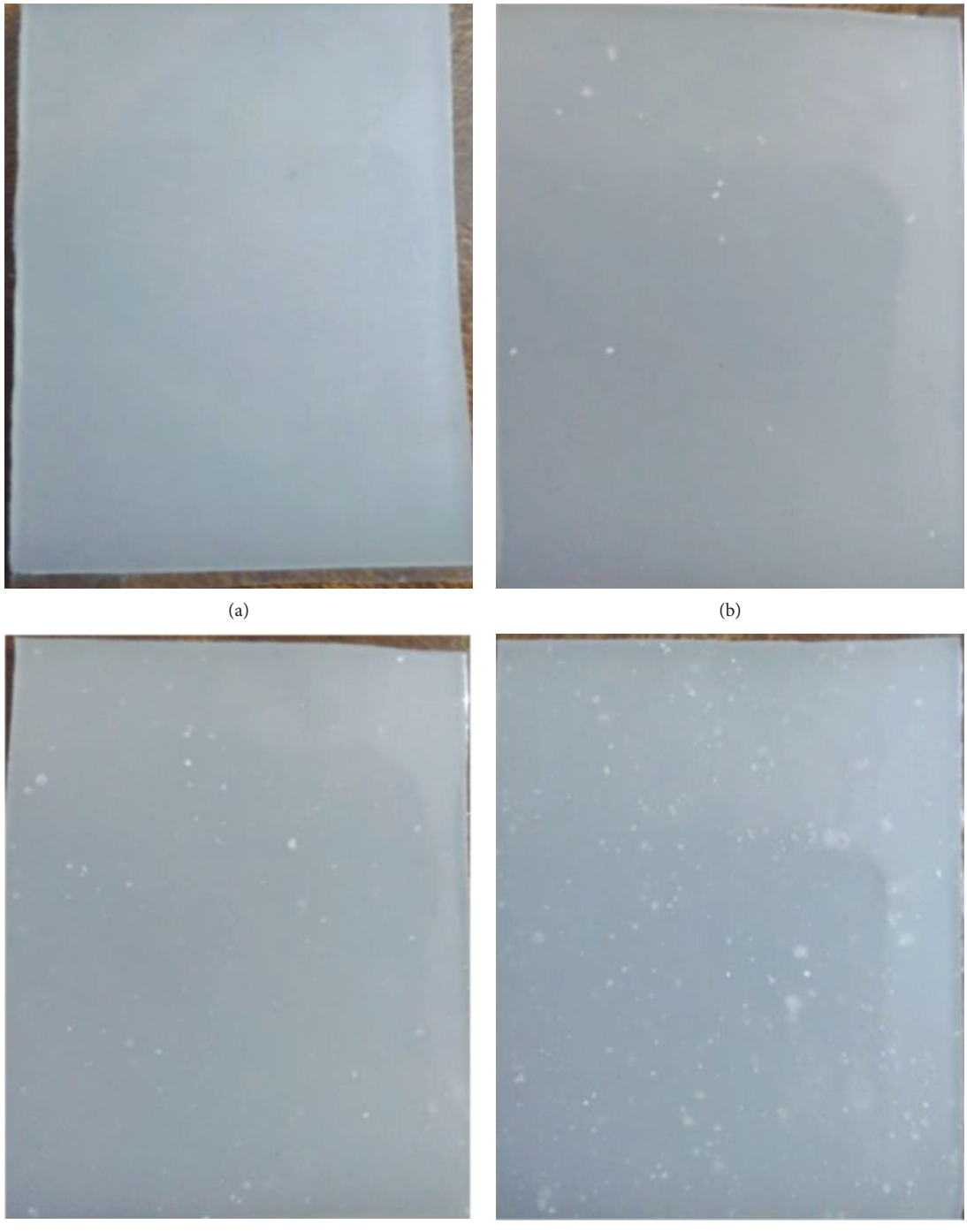

(a) (b) (c) (d)

Figure 3: Images of the surface of the LDPE/silica composites containing (a) 0 wt%, (b) 1 wt%, (c) 5 wt%, and 10 wt% of nanosilica particles.

constant (up to the uncertainties). The already mentioned decrease in the elongation at break is explained by the agglomeration of the nanosilica particles within the polymer matrix, as already mentioned.

3.2. Optical Study

3.2.1. Infrared Spectroscopic Study. The transmittance of samples was examined by Fourier-transform infrared spectroscopy (FTIR) (VERTEX 70/70v FT-IR spectrometer from Bruker™ Optics) in the wavelength range of 1-25 μm. Figure 5 shows the transmittance spectra of the SiO_2/LDPE films with different ratios. Different absorption peaks could be identified in the MIR range. The first one at ~3 μm is caused by the OH group; other peaks at ~9 μm, ~12 μm, and ~21 μm are due to the Si-O-Si resonance mode of vibrations [14]. Some of these peaks also involve the LDPE substrate in the IR absorption spectra. The peak at 9 μm gives

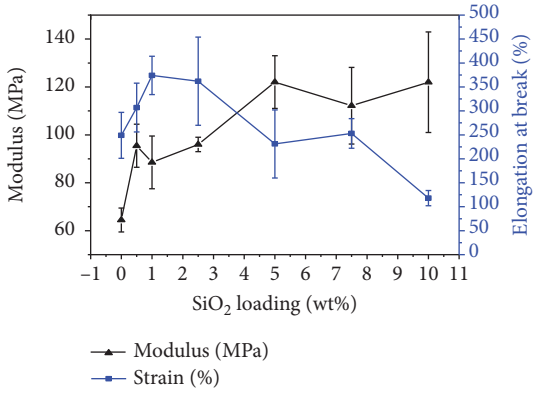

Figure 4: Elongation at break and modulus of elasticity (averaged values) as a function of different ratios of SiO_2.

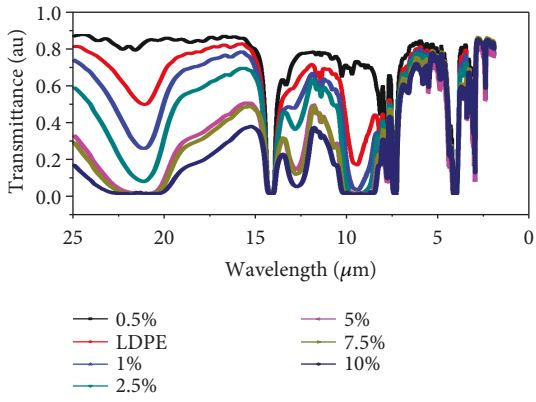

Figure 5: FTIR spectra for different ratios of LDPE/silica nanocomposite films.

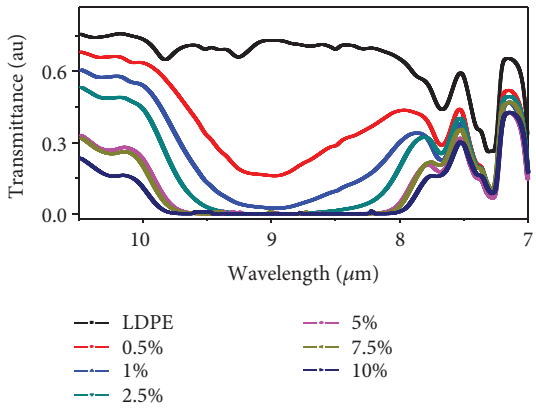

Figure 6: FTIR spectra in the range 7-10.5 μm.

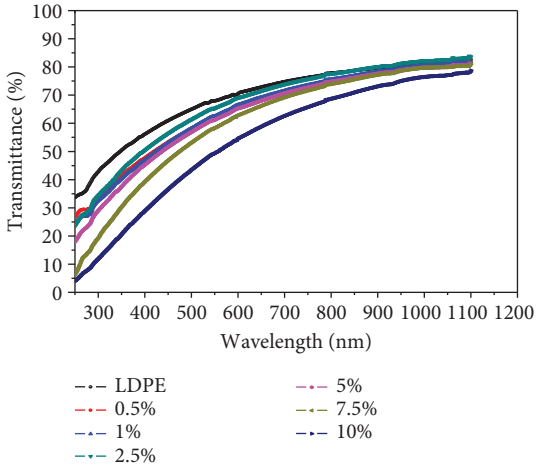

Figure 7: UV-visible spectra of LDPE/silica nanocomposite films.

SiO_2 its importance and allows it to be used in this application. We observe a decrease in the transmittance when the mixing ratio of SiO_2 increases. The changes in the average transmittance for wavelengths ranging from 7 to 10.5 μm are shown in Figure 6. We notice a sharp decline in transmittance when the ratio of SiO_2 is increased.

3.2.2. Ultraviolet-Visible Spectroscopy Study. The optical transmittance measurements of LDPE/silica nanocomposite substrate films were carried out with a UV-Vis-NIR spectrophotometer (A560 UV Spectrophotometer, AOE Instruments) at the normal incident of light in the wavelength range of 200-1100 nm. Figure 7 shows the transmittance spectra of the samples. The UV spectra show that the composite substrates (0.5, 1, 2.5, 5, and 7.5 wt% SiO_2) have no significant effect on the transmittance. On the other hand, a significant decrease in the transmittance is observed with a mixture ratio of 10 wt% SiO_2 compared to the LDPE without mixing. This decrease is addressed in Results and Discussion.

3.3. Thermal Study. We built a minigreenhouse using LDPE without mixing and another one using LDPE mixed with 2.5 wt% SiO_2. We also built a third minigreenhouse using window silka glass (the glass thickness is 6 mm, and the transmittance from 350 to 1100 nm is approximately 88%) (see Figure 8). All the three greenhouses have a cube shape with sides measuring 20 cm. Inside each greenhouse, we put a small plant. These plants were previously grown under similar conditions.

The temperature inside each greenhouse was measured using identical temperature sensors (Tecnologic UK with 0.1°C resolution). The external temperature was also measured using an identical sensor. All the measurements were made at the same moment every thirty minutes starting from 1 p.m. until 6 a.m. the next day. Figure 9 shows the temperature variations inside the three greenhouses along with the external air temperature. An increase in the temperature inside the greenhouse mixed with 2.5 wt% SiO_2 is noticed. This increase is estimated to be more than 2°C compared with the LDPE greenhouse without mixing (2°C overall and 2.2°C between 11 PM and 5 AM). We also notice that the transmittance of the greenhouse mixed with 2.5 wt% SiO_2 closely approaches that of the glass house (see the green and blue triangles in Figure 9). In fact, the average temperature difference is about 0.14°C overall and the two temperatures between 11 PM and 5 AM match each other very well.

(a) (b) (c)

Figure 8: Three greenhouses: (a) LDPE without mixing, (b) LDPE mixed with 2.5 wt% SiO_2, and (c) silica glass. This figure was reproduced from Alghdeir et al. [9] (under the Creative Commons Attribution License/public domain).

By studying the IR transmission in Figures 5, 6, and 10, a decrease in the transmittance near 9 μm with increasing mixture ratios is noticed. This result explains the rise in temperature inside the minigreenhouses (shown in Figure 10). The LDPE/silica nanocomposite barrier films preserve the thermal radiation of the ground. Thus, the internal temperature inside the greenhouse is maintained.

One can also notice that in the vicinity of 9 μm, the transmittance of the sample with a ratio of 5 wt% SiO_2 is very close to that of the sample with a ratio of 2.5 wt% SiO_2. We deduce that it may not be very beneficial to go beyond a ratio of 2.5 wt% SiO_2.

By studying the UV-VIS transmission in Figure 7, a significant decrease is noticed in the transmittance of the film with a ratio of 10 wt% SiO_2, compared with the other films with a lesser ratio (0.5, 1, 2.5, 5, and 7.5 wt% SiO_2). These five composite barrier films do not have any significant effect on the transmittance compared with that of the LDPE without

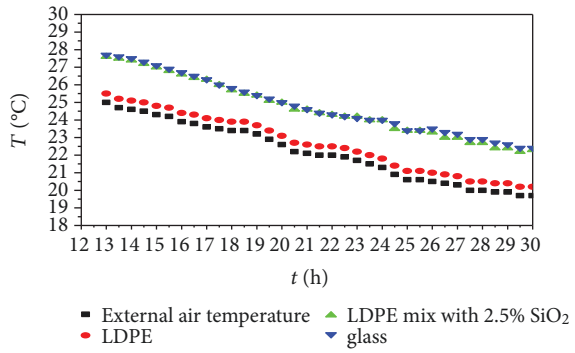

FIGURE 9: The variations of the difference of temperature (ΔT) between the temperature inside the greenhouse and the temperature in the external air during the time.

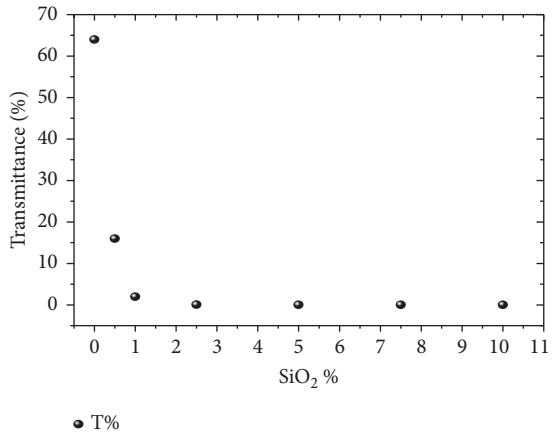

FIGURE 10: Transmittance at 9 μm as a function of different ratios of SiO_2.

mixing. Thus, the film with a ratio of 2.5 wt% SiO_2 composite was adopted to build the minigreenhouse. It has no effect on the UV-VIS transmission but it reduces the maximum transmission of the IR radiation to around 9 μm.

The refractive index of LDPE in the visible domain is 1.51, while the imaginary part is $k = 0$ [15]. It is very close to the value of the real part of the refractive index of SiO_2 which is equal to 1.43 [16]. Therefore, there should not be any significant change in the transmittance of the LDPE in the visible range when mixed with SiO_2. This is clearly seen in Figure 7) except for the last case where the ratio of SiO_2 is 10 wt%. Consequently, there should not be any significant change in the greenhouse temperature during sun-shining time. The significant reduction in the transmittance in the case where the ratio of 10 wt% SiO_2 is probably due to Mie scattering [17].

4. Conclusion

Throughout this study, silicon dioxide films with different ratios (0.5, 1, 2.5, 5, 7.5, and 10 wt% SiO_2) were mixed with a low-density polyethylene (LDPE) polymer using the melt mixing technique.

The effect of the incorporation of 0.5–10 wt% of silica particles to a tensile property of LDPE was investigated. The results showed that the addition of 1 wt% of nanosilica has successfully enhanced the tensile strength and elongation at break of the nanosilica-filled LDPE material. The incorporation of >1 wt% of nanosilica particles had caused agglomeration and uneven distribution of the particles in LDPE.

By using these LDPE/silica nanocomposites to build a minigreenhouse, SiO_2 reduces the transmission of radiation near 9 μm and allows the transmission of ultraviolet and visible radiation to pass through them during daytime (period of sunshine, without being exposed to direct sunshine). Thus, we were able to preserve the thermal radiation of the ground by raising the internal temperature of the greenhouse up to more than 2°C, compared with the same greenhouse without mixing. The temperature inside the LDPE/silica greenhouse was found to be almost identical to that inside the glass greenhouse.

Statistically speaking, the conclusions are acceptable because the experiment was replicated many times. The main gain is the fact that the LDPE/silica greenhouse has the same temperature as the glass-made greenhouse.

Data Availability

The data used to support the findings of this study are available from the corresponding author upon request.

Conflicts of Interest

The authors declare that they have no conflicts of interest.

References

[1] A. Kuzminova, A. Shelemin, M. Petr, O. Kylian, and H. Biederman, "Barrier coatings on polymeric foils for food packaging," in *WDS'13 Proceedings of Contributed Papers, Part III*, pp. 128–133, Prague, Czech Republic, 2013.

[2] O. Kylián, A. Choukourov, L. Hanyková, and H. Biederman, "Plasma technology for polymer food packaging materials," in *Ecosustainable Polymer Nanomaterials for Food Packaging: Innovative Solutions, Characterization Needs, Safety and Environmental Issues*, p. 119, Taylor and Francis Group, 2013.

[3] S. Ju, M. Chen, H. Zhang, and Z. Zhang, "Dielectric properties of nanosilica/low-density polyethylene composites: the surface chemistry of nanoparticles and deep traps induced by nanoparticles," *Express Polymer Letters*, vol. 8, no. 9, pp. 682–691, 2014.

[4] H. H. Redhwi, M. N. Siddiqui, A. L. Andrady, and S. Hussain, "Durability of LDPE nanocomposites with clay, silica, and zinc oxide: part I: mechanical properties of the nanocomposite materials," *Journal of Nanomaterials*, vol. 2013, Article ID 654716, 6 pages, 2013.

[5] A. Pal, *Low-Power VLSI Circuits and Systems*, Springer India, 2015.

[6] A. Yasunas, D. Kotov, V. Shiripov, and U. Radzionay, "Low-temperature deposition of silicon dioxide films in high-density plasma," *Semiconductor Physics, Quantum Electronics & Optoelectronics*, vol. 16, no. 2, pp. 216–219, 2013.

[7] A. Delimi, Y. Coffinier, B. Talhi, R. Boukherroub, and S. Szunerits, "Investigation of the corrosion protection of SiOx-like oxide films deposited by plasma-enhanced chemical vapor deposition onto carbon steel," *Electrochimica Acta*, vol. 55, no. 28, pp. 8921–8927, 2010.

[8] W. T. Li, R. Boswell, M. Samoc, A. Samoc, and R. P. Wang, *Thin Solid Films*, vol. 516, no. 16, pp. 5474–5477, 2008.

[9] M. Alghdeir, K. Mayya, M. Dib, and I. Alghoraibi, "Characterization of SiO_2/LDPE composite barrier films," *Journal of Materials and Environmental Sciences*, vol. 9, no. 7, pp. 2042–2050, 2018.

[10] Z. Liu, Z. Sun, X. Ma, and C. L. Yang, "Characterization of composite SiOx/polymer barrier films," *Packaging Technology and Science*, vol. 26, pp. 70–79, 2013.

[11] J. Lange and Y. Wyser, "Recent innovations in barrier technologies for plastic packaging—a review," *Packaging Technology and Science*, vol. 16, no. 4, pp. 149–158, 2003.

[12] H. Zou, S. Wu, and J. Shen, "Polymer/silica nanocomposites: preparation, characterization, properties, and applications," *Chemical Reviews*, vol. 108, no. 9, pp. 3893–3957, 2008.

[13] C. Y. Chee, N. L. Song, L. C. Abdullah, T. S. Y. Choong, A. Ibrahim, and T. R. Chantara, "Characterization of mechanical properties: low-density polyethylene nanocomposite using nanoalumina particle as filler," *Journal of Nanomaterials*, vol. 2012, Article ID 215978, 6 pages, 2012.

[14] R. Kitamura, L. Pilon, and M. Jonasz, "Optical constants of silica glass from extreme ultraviolet to far infrared at near room temperature," *Applied Optics*, vol. 46, no. 33, pp. 8118–8133, 2007.

[15] B. S. Mitchell, *An Introduction to Materials Engineering and Science for Chemical and Materials Engineers*, John Wiley & Sons, 2004.

[16] C. Xiong, W. Xu, Y. Zhao, J. Xiao, and X. Zhu, "New design graded refractive index antireflection coatings for silicon solar cells," *Modern Physics Letters B*, vol. 31, no. 19-21, article 1740028, 2017.

[17] M. Iqbal, *An Introduction to Solar Radiation*, Elsevier, 2012.

Hindawi
Journal of Nanomaterials
Volume 2019, Article ID 7470428, 6 pages
https://doi.org/10.1155/2019/7470428

Research Article

Multifunctional Polydiacetylenic Complex Films: Preferential Host-Guest Interaction with Specific Small Molecules and Recognition of Aldehyde Derivatives

Xin Wu,[1,2] Jingyuan Huang,[1,2] Xianling Piao,[3] Cheng-Shou An,[4] and Chunzhi Cui[1,2]

[1]*Department of Chemistry, College of Science, Yanbian University, Yanji 133002, China*
[2]*Key Laboratory of Natural Resource of Changbai Mountains & Functional Molecules, Ministry of Education, Yanbian University, Yanji 133002, China*
[3]*Affiliated Hospital of Yanbian University, Yanji 133000, China*
[4]*Department of Physics, College of Science, Yanbian University, Yanji 133002, China*

Correspondence should be addressed to Cheng-Shou An; anchengshou@ybu.edu.cn and Chunzhi Cui; cuichunzhi@ybu.edu.cn

Received 3 September 2018; Revised 15 October 2018; Accepted 23 October 2018; Published 18 February 2019

Guest Editor: Chandragiri V. Reddy

Two organic molecules, 10,12-pentacodiynoic acid (PCDA) and *para*-xylenediamine (*p*XDA), were complex in THF solution upon acid-base interactions and assembled into thin films with a highly ordered structure after evaporation of the solvent. The binding specificities of α-, β-, and γ-cyclodextrins (CDs) with the photopolymerized polydiacetylenic films were studied. According to the optical, morphological, and structural analyses, it was found that the films were preferentially interacted with α-CDs, as well as host-guest interaction. In addition, the polydiacetylenic films were applicable for recognizing toxic materials as aldehyde derivatives in both liquid and gas states. These fundamental results may provide more useful platforms of polydiacetylene-based materials as optoelectronic devices or chemical/biological sensors.

1. Introduction

Supramolecular assemblies have achieved great success in the construction of well-defined nano- or microarchitectures through noncovalent interactions as hydrogen bonding, π-π stacking, hydrophobic, and electrostatic interactions which resulted in tunable molecular alignment and novel functionality via a bottom-up approach [1–4]. These assembled architectures have been widely applied in many fields, including catalysis, biomedicine, optoelectronics, and energy conversion [5–9].

To date, these supramolecular assemblies can be carefully designed and controlled by external condition, such as temperature, pH, light irradiation, and electric or magnetic fields. The conformation control and tunable properties afforded by supramolecular materials would be particularly useful for functional materials containing conjugated polymers [10–13]. Owing to extended π-electron delocalization along their backbones, conjugated polymers exhibit optical properties for applications [14–16].

Polydiacetylenes (PDAs) are structurally very unique conjugated polymers [17, 18]. Under suitable conditions, the diacetylene (DA) monomers can assemble into well-ordered structures such as films and vesicles in solid and solution state. Photopolymerization of the assembled DA monomers can be initiated by UV irradiation. The resultant PDAs that possess alternating ene-yne conjugated backbone with well-organized side chains [19, 20]. When their arrayed p-orbitals are distorted under the influence of environmental perturbations such as heat, solvent, current, magnetic field, stain force, ions, pH, and ligand-receptor interaction, PDAs undergo distinct color changes (typically blue-to-red) [21, 22]. It has been considered that the change of side chain and backbone packing affects the electronic states of the PDAs, causing the change of their optical absorption and emission properties [23–25]. Our recent study presented a

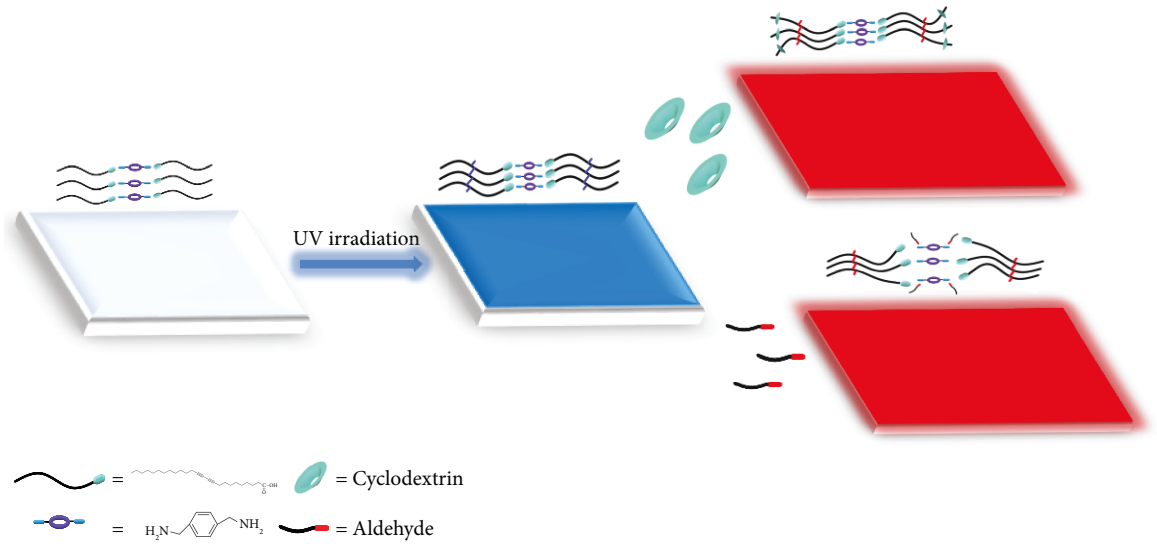

Scheme 1: Illustration of the complex film fabrication and target recognition.

facile method for fabrication of PDAs containing complex films with two organic building molecules, 10,12-pentacosadiynoic acid (PCDA) and *para*-xylenediamine (*p*XDA) [26]. The films were fabricated by acid-base interactions between the carboxylic acid of PCDA and the amino of *p*XDA. By adjusting the mixing molar ratio, the thermochromism reversibility of the complex films was modulated.

In this contribution, the complex films were endowed with other novel functions. As shown in Scheme 1, firstly, as the polymerized complex films were interacted with various sizes of small molecules, α-, β-, and γ-cyclodextrins (CDs), it is found that the α-CDs can induce a phase transition of the complex films upon specific host-guest interaction. Secondly, the complex films can selectively recognize aldehyde derivatives. In addition, the recognition induced fluorescent intensities of the complex films which were proportionate to the chain length of the aldehyde derivatives including formaldehyde, acetaldehyde, propanal, and butanal.

2. Experimental

2.1. Fabrication of the Polydiacetylenic Complex Films. A detailed fabrication method for polydiacetylenic complex films has been described in previous reports [27]. Firstly, PCDA and *p*XDA were dissolved in tetrahydrofuran (THF) as a concentration of 10 mM, respectively. Each of the pure PCDA and *p*XDA solutions was mixed as a stoichiometric molar ratio (2 : 1). Then, the mixture solution was used to form thin films by spin coating on a calcium fluoride (CaF_2) substrate by the use of a spin coater (Laurell WS-200-4T2). The resulting white films after evaporation of the solvent were photopolymerized 254 nm for 2 min at the intensity of 1 mW/cm^2. Upon the irradiation, the initial white-colored films were converted to blue-colored polydiacetylenic films. Red-phase polydiacetylenic films were obtained from the blue-phase polydiacetylenic films by applying thermal stimuli.

2.2. Characterization. The complex films were visualized with a scanning electron microscope (SEM; JEOL, JSM-5200) and a high-resolution transmission electron microscope (HR-TEM; JEOL, JEM-3010). The structure of the films was characterized by X-ray scattering (Bruker D8, Discover). The visible absorption spectra of the films were obtained using a UV-vis spectrophotometer (Agilent Technologies, HP 8453). The fluorescent images of the films were recorded using a fluorescence microscope (Olympus, BX51) excited by a Xe lamp. The circular dichroism (CD) spectra were collected on an Applied Photophysics Chirascan Spectrometer (CS30088). The measurement was carried out at the wavelength range of 200-400 nm at room temperature in a 1.0 cm length cell. The scanning speed is 100 nm min^{-1}. The baseline was corrected using deionized (DI) water.

3. Results and Discussion

3.1. Fluorescent and Absorption Analyses upon Interaction with CD Molecules. It is well-known that CDs can form inclusion complex with a variety of substrates upon host-guest interaction [28–30]. The polymerized complex films were incubated with various concentration of α-, β-, and γ-CDs. Figure 1(a) shows the fluorescent images of the polymerized complex films after incubation in an appropriate concentration of the CD solution for 20 min. Clearly, the films incubated in 5 and 10 mM α-CD solutions emit a red fluorescent signal. However, the films incubated in β- and γ-CDs and 1 mM α-CDs only emit pale fluorescent signals which can demonstrate the α-CDs respond to the best shape match with the alkyl side chain of the PDA molecules in the complex films through the host-guest interaction. It can be considered that the repulsive force between the adjacent

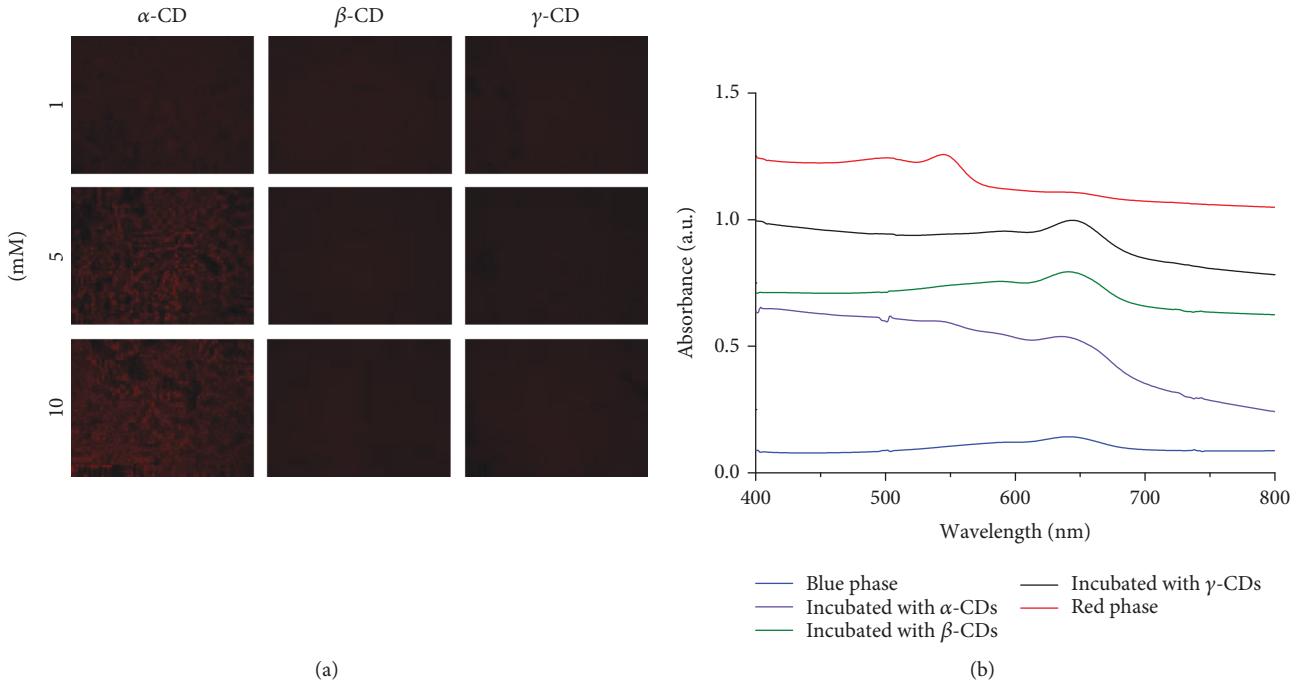

Figure 1: Fluorescent images (a) and UV-visible absorption spectra of the complex films after incubated with various CDs.

complexes (α-CDs and alkyl side chain) induces an irreversible phase transition of the PDA backbone. Figure 1(b) shows the absorption spectra of the polymerized complex films after incubation in an appropriate concentration (10 mM) of the CD solution for 20 min. Initially, the polymerized films show a typical blue phase corresponding to an absorption maximum wavelength at ~640 nm. After being incubated in α-CD solution, a new peak at ~540 nm can be observed which corresponds to the typical red-phase PDA materials; however, the absorption maximum peak remains at ~640 nm. It means electronic states of some PDA in the complex films were changed. It also matches with the result of the fluorescent image of the complex films after incubated in α-CD solution. Compared with the case of α-CD solution, neither β-CDs nor γ-CDs induced the phase transition of the PDA component. As the complex films were subjected to annealing treatment, the absorption maximum peak shifted to 540 nm, completely.

3.2. Morphological Analyses upon Interaction with CD Molecules. To observe the morphologic change upon incubation with CD solution, complex films were visualized with SEM (Figure 2). It shows that the complex films are consisted of numerous irregular flakes. However, flattened cuboid-type architectures are observed on the surface of the complex films after incubated in α-CD solution. On the contrary, the appearance of similar architectures cannot be observed in the ones which incubated in β- and γ-CDs. Hence, we consider that the flattened cuboid-type architectures are the ternary complex which is consisted of α-CDs, PCDA, and *p*XDA.

3.3. Structural Analyses upon Interaction with CD Molecules. To examine structural changes of the complex films, X-ray diffraction (XRD) patterns were observed (Figure 3). The XRD pattern of the initial complex films shows peaks at 3.5°, 5.2°, and 10.3° which corresponded to the (200), (300), and (600) planes, respectively, as well as the ones which incubated in β- and γ-CDs. Significantly, two new peaks can be observed at 5.7° and 11.4° in the pattern of the one which incubated in α-CDs. It means that the two peaks are originated from the new ternary complex which induced by the preferential host-guest interaction between α-CDs and polydiacetylenic films. The results of the XRD patterns are also matched with the morphological change of the complex films.

3.4. Interaction with Aldehyde Derivatives. In addition, the polydiacetylenic films were endowed with a recognition function of aldehyde derivatives. As a toxic material, formaldehyde is a probable human carcinogen, an allergen, and an intense irritant of the eyes and mucous membranes and is therefore considered as highly problematic indoor pollutant [31, 32]. Figure 4(a) shows the comparison of the fluorescent intensities which emitted from polydiacetylenic films after they were exposed to DI water, ammonia solution, ethanol, and formaldehyde solution, respectively. Compared with other films, only the ones exposed in formaldehyde solution emitted fluorescent signals. It means that recognition of formaldehyde is based on nucleophilic addition of an amine to the aldehyde, forming an imine [33, 34]. Meanwhile, the newly formed *p*XDA-imine-formaldehyde structures exert external stress

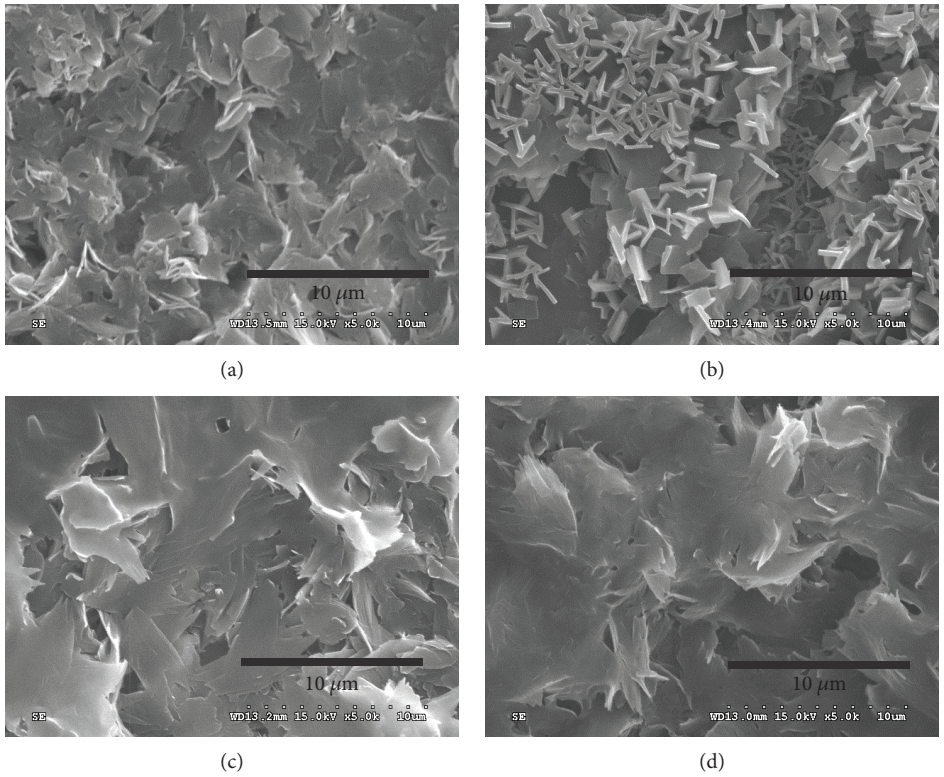

Figure 2: SEM images of initial complex films (a) and the films after incubated with α- (b), β- (c), and γ-CDs (d).

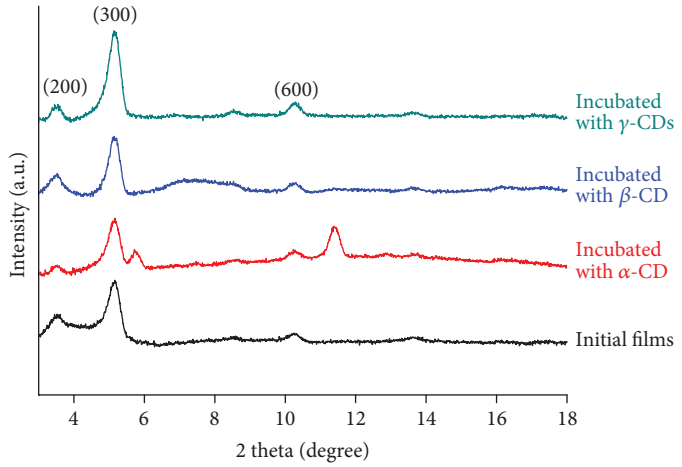

Figure 3: X-ray diffraction patterns for the initial complex films and the films after incubated with α-, β-, and γ-CDs.

on the PDA backbone, and it induces the disarrangement of the PDA backbone. Hence, only the ones exposed in formaldehyde solutions emit red fluorescent signal. In addition, as the polydiacetylenic films are also exposed in other aldehyde derivatives including acetaldehyde, propanal, butanal, and hexanal, one of the interesting phenomena which can be seen is that the fluorescent intensities are proportionate to the molecular weight of the aldehyde derivatives, as shown in Figure 4(b). It considered that the enhancement of fluorescent intensities is due to the increase of the length of alkane and the greater repulsive force resulting from it.

4. Conclusions

The study described above has led to the development of a recognition system based on polydiacetylenic complex films. Distinction is simply made using nonfluorescent-to-red fluorescent response. Specifically, the complex films are possible to recognize the exact size of α-CDs through preferential host-guest interaction. It also induces the morphological and structural change of the films. The red fluorescent intensity developed upon incubation of the complex films in aldehyde derivative solution is directly proportional to the length of alkane.

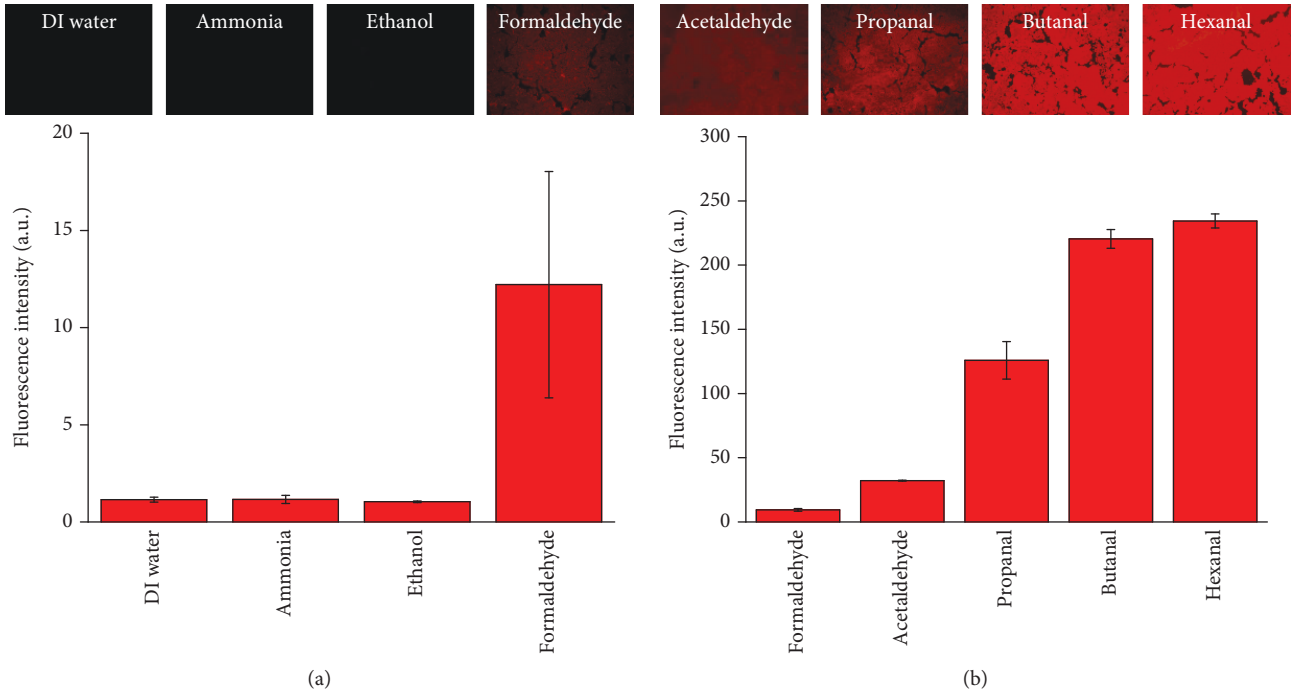

Figure 4: Fluorescent intensities of complex films after exposed to DI water, ammonia solution, ethanol, and formaldehyde solution, respectively (a). Fluorescent intensities of complex films after exposed to formaldehyde, acetaldehyde, propanal, butanal, and hexanal solution (b).

Data Availability

The data used to support the findings of this study are included within the article.

Conflicts of Interest

The authors declare that they have no conflicts of interest.

Authors' Contributions

Xin Wu and Jingyuan Huang contributed equally to this work.

Acknowledgments

This work was supported by the Jilin Provincial Science and Technology Department (Grant no. 20180520153JH) and the 111 Project.

References

[1] T. Aida, E. W. Meijer, and S. I. Stupp, "Functional supramolecular polymers," *Science*, vol. 335, no. 6070, pp. 813–817, 2012.

[2] P. K. Kundu, D. Samanta, R. Leizrowice et al., "Light-controlled self-assembly of non-photoresponsive nanoparticles," *Nature Chemistry*, vol. 7, no. 8, pp. 646–652, 2015.

[3] K. Ariga, Q. Ji, T. Mori et al., "Enzyme nanoarchitectonics: organization and device application," *Chemical Society Reviews*, vol. 42, no. 15, pp. 6322–6345, 2013.

[4] K. Ariga, J. Li, J. Fei, Q. Ji, and J. P. Hill, "Nanoarchitectonics for dynamic functional materials from atomic-/molecular-level manipulation to macroscopic action," *Advanced Materials*, vol. 28, no. 6, pp. 1251–1286, 2016.

[5] J. Fei and J. Li, "Controlled preparation of porous TiO_2-Ag nanostructures through supramolecular assembly for plasmon-enhanced photocatalysis," *Advanced Materials*, vol. 27, no. 2, pp. 314–319, 2015.

[6] D. K. Kumar and J. W. Steed, "Supramolecular gel phase crystallization: orthogonal self-assembly under non-equilibrium conditions," *Chemical Society Reviews*, vol. 43, no. 7, pp. 2080–2088, 2014.

[7] J. L. Zhang, J. Q. Zhong, J. D. Lin et al., "Towards single molecule switches," *Chemical Society Reviews*, vol. 44, no. 10, pp. 2998–3022, 2015.

[8] M. Li, M. Radić Stojković, M. Ehlers, E. Zellermann, I. Piantanida, and C. Schmuck, "Use of an octapeptide-guanidiniocarbonylpyrrole conjugate for the formation of a supramolecular β-helix that self-assembles into pH-responsive fibers," *Angewandte Chemie*, vol. 55, no. 42, pp. 13015–13018, 2016.

[9] S. Fleming and R. V. Ulijn, "Design of nanostructures based on aromatic peptide amphiphiles," *Chemical Society Reviews*, vol. 43, no. 23, pp. 8150–8177, 2014.

[10] M. Han, H. Y. Zhang, L. X. Yang, Q. Jiang, and Y. Liu, "A reversible luminescent lanthanide switch based on a dibenzo [24]-crown-8-dipicolinic acid conjugate," *Organic Letters*, vol. 10, no. 24, pp. 5557–5560, 2008.

[11] C.-L. Zhu, X.-W. Wang, Z.-Z. Lin, Z.-H. Xie, and X.-R. Wang, "Cell microenvironment stimuli-responsive controlled-release delivery systems based on mesoporous silica nanoparticles,"

Journal of Food and Drug Analysis, vol. 22, no. 1, pp. 18–28, 2014.

[12] P. Xue, J. Ding, M. Jin, and R. Lu, "Rapid gel-to-sol transition triggered by a photoacid generator under low-power light," *Journal of Materials Chemistry C*, vol. 5, no. 22, pp. 5299–5303, 2017.

[13] E. R. Draper and D. J. Adams, "Photoresponsive gelators," *Chemical Communications*, vol. 52, no. 53, pp. 8196–8206, 2016.

[14] L. Feng, C. Zhu, H. Yuan, L. Liu, F. Lv, and S. Wang, "Conjugated polymer nanoparticles: preparation, properties, functionalization and biological applications," *Chemical Society Reviews*, vol. 42, no. 16, pp. 6620–6633, 2013.

[15] C. Cui, D. H. Park, H. Choi, J. Joo, and D. J. Ahn, "Protein recognition by phase transition of aptamer-linked polythiophene single nanowire," *Small*, vol. 12, no. 9, pp. 1154–1158, 2016.

[16] J. Huang, J. Choi, G. Lee et al., "Photoluminescence enhancement of poly (3-methylthiophene) nanowires upon length variable DNA hybridization," *Polymers*, vol. 10, no. 1, pp. 100–107, 2018.

[17] D. H. Charych, J. O. Nagy, W. Spevak, and M. D. Bednarski, "Direct colorimetric detection of a receptor-ligand interaction by a polymerized bilayer assembly," *Science*, vol. 261, no. 5121, pp. 585–588, 1993.

[18] D. J. Ahn and J. M. Kim, "Fluorogenic polydiacetylene supramolecules: immobilization, micropatterning, and application to label-free chemosensors," *Accounts of Chemical Research*, vol. 41, no. 7, pp. 805–816, 2008.

[19] J. M. Kim, E. K. Ji, S. M. Woo, H. Lee, and D. J. Ahn, "Immobilized polydiacetylene vesicles on solid substrates for use as chemosensors," *Advanced Materials*, vol. 15, no. 13, pp. 1118–1121, 2003.

[20] D. J. Ahn, E. H. Chae, G. S. Lee et al., "Colorimetric reversibility of polydiacetylene supramolecules having enhanced hydrogen-bonding under thermal and pH stimuli," *Journal of the American Chemical Society*, vol. 125, no. 30, pp. 8976-8977, 2003.

[21] J. M. Kim, Y. B. Lee, S. K. Chae, and D. J. Ahn, "Patterned color and fluorescent images with polydiacetylene supramolecules embedded in poly (vinyl alcohol) films," *Advanced Functional Materials*, vol. 16, no. 16, pp. 2103–2109, 2006.

[22] B. Yoon, S. Lee, and J. M. Kim, "Recent conceptual and technological advances in polydiacetylene-based supramolecular chemosensors," *Chemical Society Reviews*, vol. 38, no. 7, pp. 1958–1968, 2009.

[23] R. W. Carpick, D. Y. Sasaki, and A. R. Burns, "First observation of mechanochromism at the nanometer scale," *Langmuir*, vol. 16, no. 3, pp. 1270–1278, 2000.

[24] M. K. Park, K. W. Kim, D. J. Ahn, and M. K. Oh, "Label-free detection of bacterial RNA using polydiacetylene-based biochip," *Biosensors & Bioelectronics*, vol. 35, no. 1, pp. 44–49, 2012.

[25] M. A. Reppy and B. A. Pindzola, "Biosensing with polydiacetylene materials: structures, optical properties and applications," *Chemical Communications*, vol. 42, pp. 4317–4338, 2007.

[26] C. Cui, G. S. Lee, and D. J. Ahn, "Composition-dependent thermochromatic reversibility of polymerized diacetylene-xylenediamine complex films," *Macromolecular Research*, vol. 21, no. 12, pp. 1372–1374, 2013.

[27] Z. H. Tang and B. A. Yang, "A novel approach to polydiacetylenic nanomaterials with thermochromatic reversibility," *Journal of Materials Science*, vol. 42, no. 24, pp. 10133–10137, 2007.

[28] J. M. Kim, Y. B. Lee, D. H. Yang, J.-S. Lee, G. S. Lee, and D. J. Ahn, "A polydiacetylene-based fluorescent sensor chip," *Journal of the American Chemical Society*, vol. 127, no. 50, pp. 17580-17581, 2005.

[29] J. T. Cho, S.-M. Woo, D. J. Ahn, K.-D. Ahn, H. Lee, and J.-M. Kim, "Cyclodextrin-induced color changes in polymerized diacetylene Langmuir-Schaefer films," *Chemistry Letters*, vol. 32, no. 3, pp. 282-283, 2003.

[30] C. W. Lee, H. Choi, M. K. Oh et al., "ZnO-based cyclodextrin sensor using immobilized polydiacetylene vesicles," *Electrochemical and Solid-State Letters*, vol. 10, no. 1, pp. J1–J3, 2007.

[31] G. D. Leikauf, *Environmental Toxicants: Human Exposures and their Health Effects*, M. Lippmann, Ed., Wiley, Hoboken, NJ, USA, 3rd edition, 2009.

[32] M. Krzyzanowski, *WHO Air Quality Guidelines for Europe*, World Health Organization, Copenhagen, 2nd edition, 2000.

[33] L. T. Gibson, W. J. Kerr, A. Nordon et al., "On-site determination of formaldehyde: a low cost measurement device for museum environments," *Analytica Chimica Acta*, vol. 623, no. 1, pp. 109–116, 2008.

[34] L. Feng, C. J. Musto, and K. S. Suslick, "A simple and highly sensitive colorimetric detection method for gaseous formaldehyde," *Journal of the American Chemical Society*, vol. 132, no. 12, pp. 4046-4047, 2010.

Hindawi
Journal of Nanomaterials
Volume 2019, Article ID 6262176, 7 pages
https://doi.org/10.1155/2019/6262176

Research Article

Pd Nanoparticles Stabilized by Hypercrosslinked Polystyrene Catalyze Selective Triple C-C Bond Hydrogenation and Suzuki Cross-Coupling

Linda Zh. Nikoshvili[1], **Nadezhda A. Nemygina**[1,2], **Tatiana E. Khudyakova**[1], **Irina Yu. Tiamina**[1], **Alexey V. Bykov**[1], **Barry D. Stein**[3], **Esther M. Sulman**[1] and **Lioubov Kiwi-Minsker**[2,4]

[1]*Tver Technical University, A.Nikitina str., 22, 170026 Tver, Russia*
[2]*Tver State University, Zhelyabova str., 33, 170100 Tver, Russia*
[3]*Indiana University, Department of Biology, IN, 47405 Bloomington, USA*
[4]*Ecole Polytechnique Fédérale de Lausanne, GGRC-ISIC-EPFL, CH-1015 Lausanne, Switzerland*

Correspondence should be addressed to Linda Zh. Nikoshvili; nlinda@science.tver.ru

Received 28 August 2018; Revised 1 November 2018; Accepted 8 November 2018; Published 13 January 2019

Guest Editor: Chandragiri V. Reddy

This paper describes the synthesis of Pd-containing catalysts based on nonfunctionalized hypercrosslinked polystyrene via impregnation with Pd acetate. Developed Pd nanoparticulate catalyst allowed achieving conversion of aryl halide up to 90% in Suzuki cross-coupling reaction under mild conditions and at the absence of phase-transfer agents. During the selective hydrogenation of triple C-C bond of 2-methyl-3-butyn-2-ol, up to 96% selectivity with respect to corresponding olefinic alcohol was found at 95% conversion. The influences of the procedure of catalyst synthesis like precursor decomposition and reductive activation method on Pd nanoparticle formation are discussed.

1. Introduction

Metal nanoparticles (NPs) have unique catalytic properties due to a high ratio of surface-to-total atoms allowing a high number of reactive sites [1]. Catalytic properties of NPs depend on their size, size distribution, and environment provided by support [2, 3]. The most important issue arising while developing nanoparticulate catalysts is control over NP sizes and morphology as well as prevention of their aggregation and leaching. Besides, low-cost, reproducible, and scalable synthetic approaches to the synthesis of catalytic NPs are of great importance [4]. Among the diverse catalytic materials, supported metal NPs are the most widely studied and extensively employed in industrial processes [5]. In particular, reactions catalyzed by Pd NPs are widespread in fine organic synthesis and the polymer-supported are one of the most prospective [6]. For understanding of the behavior of polymer-based palladium catalyst, the role of support should be carefully analyzed since the formation of NPs in nanostructured polymeric environment controls over NP size and size distribution stabilizing them but also may strongly influence the surface of NPs [6]. There are several approaches to the synthesis of Pd NPs using polymers: (i) formation of colloid metal NPs stabilized by block copolymer micelles; (ii) formation of metal NPs in ultrathin polyelectrolyte layers or brushes; and (iii) formation of metal NPs into the cavities (pores) of 3D polymeric networks [7, 8]. Among numerous supports, rigid nanostructured polymers such as hypercrosslinked polystyrene (HPS) can be considered the most promising. Recently, we have shown that the HPS of MN100 type bearing amino groups can be used as a support for

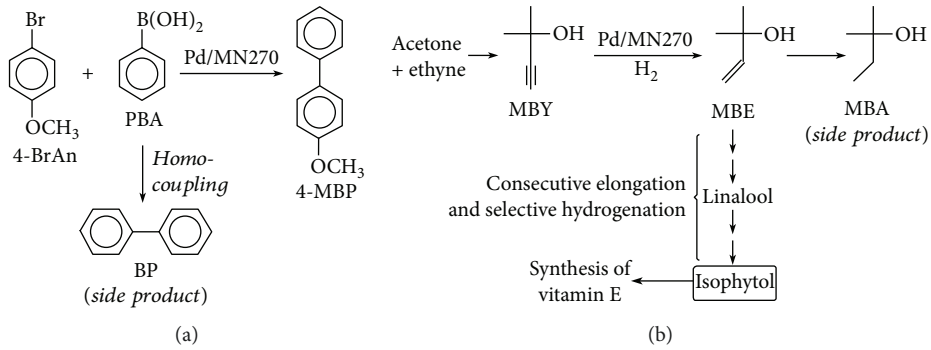

Figure 1: Reaction schemes of Suzuki cross-coupling of 4-BrAn and PBA (a) and selective hydrogenation of MBY (b).

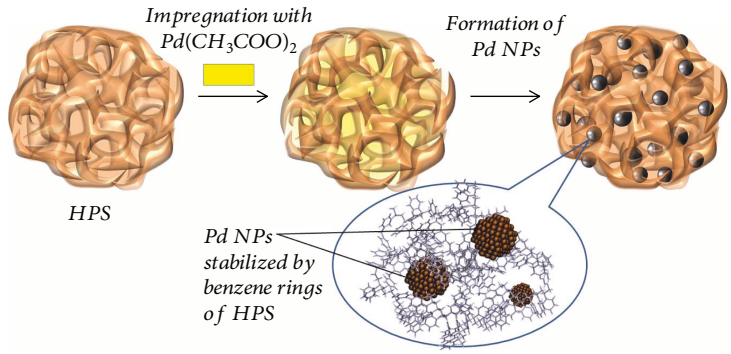

Figure 2: General scheme of Pd/HPS catalyst synthesis.

palladium NPs and clusters to catalyze effectively Suzuki reaction [9] and selective hydrogenation of triple bond in alkynols [10].

This work is devoted to the study of Pd-containing catalysts synthesized via impregnation of nonfunctionalized HPS of MN270 type by Pd acetate. We aimed at answering the questions regarding Pd NP formation and catalytic behavior of the Pd/MN270 system, in particular, (i) does the chosen combination of palladium precursor and the polymer support of the reduction step really matter, and (ii) does alkali metal addition to the catalyst composition improve catalytic properties of Pd/MN270 in C-C triple bond hydrogenation as it was observed [8] for Pd/MN100 catalytic system?

2. Materials and Methods

2.1. Materials. HPS Macronet MN270 (Purolite Int., UK) was washed with distilled water and acetone and dried under vacuum as described elsewhere [11]. 4-Bromoanisole (4-BrAn, ≥98%) was purchased from Merck KGaA. 4-Methoxybiphenyl (4-MBP, >99%) was purchased from Tokyo Chemical Industry Co. Ltd. Phenylboronic acid (PBA, 95%), diphenylamine (99%) (internal standard), biphenyl (BP, 99.5%), 2-methyl-3-butyn-2-ol (MBY, >99%), 2-methyl-3-buten-2-ol (MBE, >97%), 2-methyl-2-butanol (MBA, >96%), tetrahydrofuran (THF, ≥99.9%), toluene (99.8%), ethanol (EtOH, ≥99.8%), sodium carbonate (Na_2CO_3, ≥99.5%), and sodium hydroxide (NaOH, ≥98%) were obtained from Sigma-Aldrich. Palladium acetate ($Pd(CH_3COO)_2$, Pd content 47.68%) was purchased from JSC "Aurat" (Moscow, Russian Federation). All chemicals were used as received. Distilled water was purified with an Elsi-Aqua water purification system.

2.2. Catalyst Synthesis. HPS-based Pd-containing catalyst with calculated metal loading 1.5 wt.% was synthesized via conventional wet impregnation according to the procedure, which we described earlier elsewhere [9–12]. In a typical experiment, 1 g of pretreated (washed with distilled water and then with acetone), dried, and crushed (<70 μm) granules of HPS was impregnated with 2.7 mL of the $Pd(CH_3COO)_2$ THF solution (concentration 0.058 mol/L). The Pd-containing polymer was dried at 70°C, treated with 2.7 mL of Na_2CO_3 aqueous solution (concentration 0.035 mol/L), and dried until a constant weight was achieved. The catalyst was washed with distilled water until neutral pH and dried at 70°C. Catalyst was designated as Pd/MN270-NaW, where "Na" indicates treatment with sodium carbonate and "W" indicates washing until neutral pH. The aim of treatment with Na_2CO_3 was the decomposition of Pd precursor and acceleration of Pd precipitation in the form of PdO or Pd NPs inside the HPS pores. The catalyst was tested in Suzuki cross-coupling between 4-BrAn and PBA (Figure 1(a)) and selective hydrogenation of the C-C triple bond of MBY (Figure 1(b)). The reactions are industrially important, for example, as a semiproduct of fragrant synthesis and fat-soluble vitamins [13]. It is important to underline that catalyst was used either as synthesized or after preliminary gas-phase reduction (Figure 2) in hydrogen (flow rate 100 mL/min, temperature 300°C, 2 h). In the latter case, the catalyst was designated as Pd/MN270-NaW-H_2. Additionally, in the case of MBY hydrogenation, the in situ treatment

with hydrogen at reaction conditions during 60 min (liquid-phase reduction) was applied in order to ensure the formation of Pd NPs before the reaction starts.

2.3. Catalyst Testing. Catalytic testing of synthesized HPS-based samples was carried out in a 60 mL isothermal glass batch reactor installed in a shaker at vigorous stirring (more than 800 two-sided sharing per minute), which avoids external diffusion limitation. The internal diffusion limitations were also excluded via crashing of HPS up to the size less than 70 μm. The total volume of liquid phase was 30 mL. A recirculating bath (LOIP LT 100, Saint-Petersburg, Russia) was used to stabilize the reaction temperature within ±1°C with water as a heating medium.

Liquid-phase hydrogenation of MBY was carried out at 90°C using toluene (30 mL) as a solvent. The reactor in this case was connected to a gasometrical burette for on-line hydrogen consumption control. At the beginning of each experiment, the temperature was set and allowed to stabilize (ca. 30 min), the reactor was charged with catalyst (Pd quantity was 0.0019 mmol), and hydrogen was then introduced for liquid-phase catalyst activation during 60 min. Then MBY (17.85 mmol) was introduced and the reaction started. Samples of the reaction mixture were analyzed via GC (Kristallux 4000 M) equipped with FID and capillary column ZB-WAX (60 m × 0.53 mm i.d., 1 μm film thickness). Retention times for MBY, MBE, and MBA are 3.81 min, 2.52 min, and 2.39 min, respectively. Helium was used as a carrier gas. The concentrations of the reaction mixture components were calculated using an absolute *calibration* method.

Suzuki cross-coupling was carried out in the same set-up but under an inert atmosphere (nitrogen). Mixture of EtOH and water (EtOH: H_2O vol. ratio = 5) was used as a solvent (30 mL). In each experiment, the quantity of 4-BrAn was equal to 1.00 mmol with a 1.5 molar excess of PBA. Pd quantity was 0.0066 mmol. Before the catalyst addition in the reactor (time "zero," $t = 0$ for the reaction), in each experiment, the control experiment (duration of 60 min) was carried out in order to ensure that the reaction does not take place in the absence of a catalyst. A noninvasive liquid sampling system allowed a controlled removal of aliquots (0.1–0.5 cm^3) from the reactor by the syringe and analyzed via GC-MS (Shimadzu GCMS-QP2010S) equipped with a capillary column HP-1MS (30 m × 0.25 mm i.d., 0.25 μm film thickness). Helium was used as a carrier gas. The concentrations of the reaction mixture components were calculated using the internal standard (diphenylamine) *calibration* method. Retention times for 4-BrAn, BP, diphenylamine, 4-MBP, and PBA are 3.05 min, 4.58 min, 6.05 min, 6.31 min, and 9.67 min, respectively.

2.4. Catalyst Characterization

2.4.1. X-Ray Photoelectron Spectroscopy (XPS). XPS data were obtained using Mg Kα (hν = 1253.6 eV) radiation with an ES-2403 spectrometer (Institute for Analytic Instrumentation of RAS, St. Petersburg, Russia) equipped with energy analyzer PHOIBOS 100-MCD5 (SPECS, Germany) and X-ray source XR-50 (SPECS, Germany). All the data were acquired at an X-ray power of 250 W. Survey spectra were recorded at an energy step of 0.5 eV with analyzer pass energy 40 eV, and high resolution spectra were recorded at an energy step of 0.05 eV with analyzer pass energy 7 eV. Samples were allowed to outgas for 180 min before analysis and were stable during the examination. The data analysis was performed by CasaXPS.

2.4.2. Transmission Electron Microscopy (TEM). Pd NP sizes were evaluated by TEM using a JEOL JEM1010 instrument at an electron accelerating voltage of 80 kV. Samples were prepared by embedding the catalyst in epoxy resin following microtomming (ca. 50 nm thick) at ambient temperature. Images were obtained with the Gatan digital camera and analyzed with the Adobe Photoshop software package and the Scion Image Processing Toolkit.

2.4.3. Diffuse Reflectance Infrared Fourier Transform (DRIFT) Spectroscopy. DRIFT spectra were recorded in the range of 4000–500 cm^{-1} with the step 4 cm^{-1} using an IRPrestige-21 spectrophotometer equipped with a DRS-8000 diffuse reflectance accessory (Shimadzu, Japan). The material of the mirror of the optical system of DRS-8000 was used as a background.

3. Results and Discussion

3.1. Catalyst Characterization. TEM investigation of Pd/MN270-NaW showed that independently of the reduction method (gas-phase reduction in hydrogen flow or liquid-phase reduction in situ, which was also applied along with the H_2 gas-phase reduction in the case of MBY hydrogenation), impregnation of MN270 with $Pd(CH_3COO)_2$ results in the formation of relatively small Pd NPs with a mean diameter of ~3–5 nm (see Figures 3(b) and 3(d)). Interesting in the catalyst taken after the reaction of Suzuki cross-coupling, Pd NPs with a mean diameter of 3.7 ± 0.7 nm were found (Figure 3(a)) being about the same as in the case of preliminarily reduced sample (see Figure 3(c)). This observation also shows the ability of HPS of controlling to some extent the process of Pd NP formation probably as a result of the transmetalation step involved in a mechanism [14] of Suzuki cross-coupling.

For as-synthesized catalysts, the XPS data revealed that the surface of all the samples contains chlorine (remained in a traces after the HPS synthesis), carbon, oxygen, and Pd. The following components were found on the surface of unreduced catalysts: $Pd(CH_3COO)_2$, PdO, small Pd_n clusters ($n \leq 13$) [15], and Pd NPs. The presence of PdO in the catalyst composition is due to the precursor decomposition during the catalyst synthesis and/or to the partial oxidation of the surface of Pd NPs since the catalysts were synthesized and stored in air. It is worthy to note that the HPS structure remains stable during the impregnation with Pd acetate as well as during the catalyst reduction (see the results of DRIFT spectroscopy in Supporting Materials, Figure S1). Values of binding energy of Pd $3d_{5/2}$ obtained from high resolution spectra (Figure S2) of differently synthesized samples are presented in Table 1.

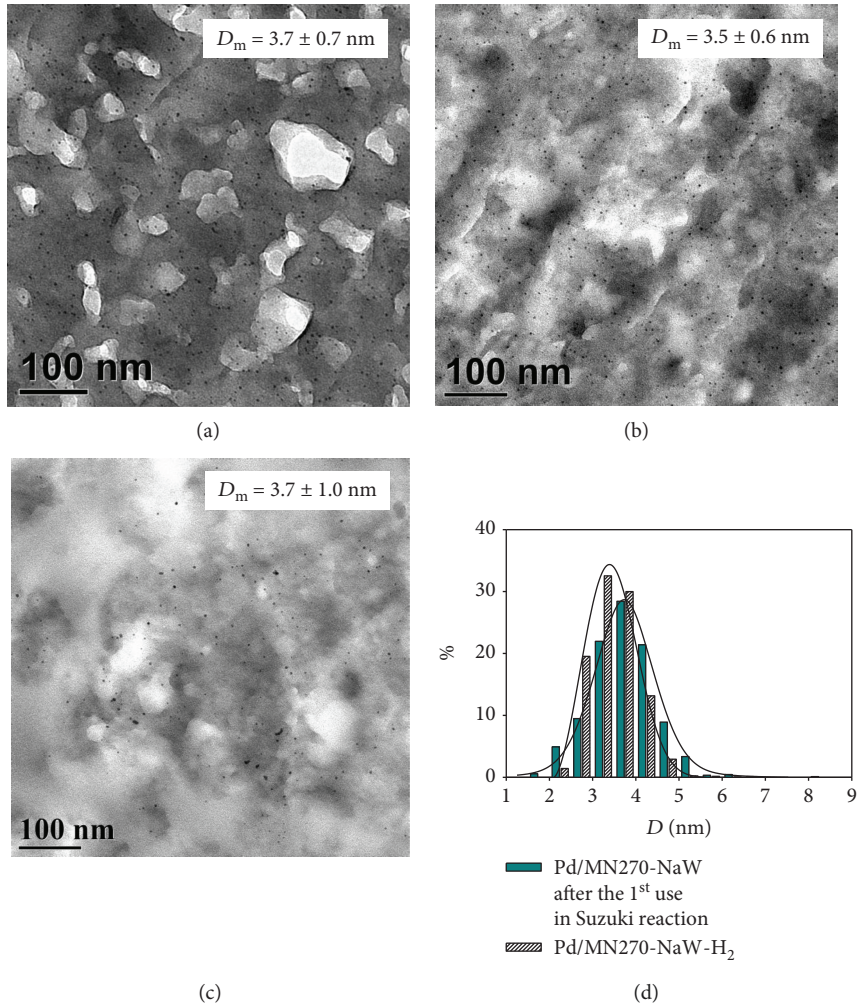

Figure 3: TEM images of Pd/MN270-NaW (taken after the first use in Suzuki reaction (a), preliminarily reduced in hydrogen flow (b), and taken after liquid-phase reduction in situ at conditions of MBY hydrogenation (c)) and comparison of NP size distributions (d).

As it can be seen from the XPS data (Table 1), preliminarily treatment of the catalyst with sodium carbonate accelerates the precursor decomposition and formation of metal NPs during the subsequent reduction in hydrogen flow. The fact that mainly PdO is on the surface of reduced Pd/MN270-NaW-H_2 can be ascribed to the partial oxidation of NP surface after exposition of the catalyst in air. We believe that since PdO is positioned on the particle surface, it is more accessible for XPS analysis than Pd(0).

3.2. Suzuki Cross-Coupling. Results of catalytic testing of Pd/MN270-NaW and Pd/MN270-NaW-H_2 samples in a model reaction of Suzuki cross-coupling of 4-BrAn and PBA (Figure 1(a)) are presented in Figure 4. After 1 h of reaction, conversion of 4-BrAn reached 90.0% and 79.4% for Pd/MN270-NaW and Pd/MN270-NaW-H_2, respectively. Selectivity to 4-MBP was about the same for both samples: 97.8% and 98.1% with BP formed as by-product.

Generally, it is accepted that virtually any form of Pd (Pd^{2+}, Pd(0) in clusters or NPs) can catalyze the cross-coupling since this process involves the cycle of Pd oxidation-reduction during catalysis [17]. Recently, we have shown [9] that 98.4% conversion of 4-BrAn can be achieved after 1 h using unreduced HPS of MN100 type impregnated with $PdCl_2(CH_3CN)_2$ and containing about 85% of Pd(II) without any bulk Pd(0) corresponding to NPs. In the case of Pd/MN100, the process of NP formation is relatively slow, possibly due to the strong interaction of MN100 with Pd salt. In contrast, for Pd/MN270-NaW, a fast Pd precipitation in the form of numerous NPs takes place (see Figure 3(a)) and conversion of 4-BrAn reached only 90%. The reduction of Pd/MN270-NaW in gaseous hydrogen diminished further the catalyst efficiency allowing conversion only about 80% after 1 hour of reaction.

At the same time, to the best of our knowledge, for preliminarily reduced catalysts [9], Pd NPs serve as a source of catalytic species at the beginning of the reaction and are responsible for observed activity. Taking into account this fact, it is not surprising that in the case of Pd/MN270-NaW-H_2, for which the formation of small Pd NPs (3.5 nm) in H_2 medium occurs relatively fast, 4-BrAn conversion reached 79.4% that is in 1.4 times higher in

Table 1: XPS data for Pd/MN270 and Pd/MN270-NaW samples.

Chemical state of palladium	Surface Pd content (at %) and the corresponding binding energy (eV) [16]			
	Pd/MN270	Pd/MN270-H_2	Pd/MN270-NaW	Pd/MN270-NaW-H_2
$Pd(CH_3COO)_2$	58 (338.8)	30 (338.3)	29 (338.6)	—
PdO	25 (337.3)	28 (337.3)	22 (337.1)	60 (337.4)
Pd NPs	7 (335.0)	20 (335.0)	13 (335.0)	13 (335.0)
Pd_n clusters	10 (335.9)	22 (336.0)	36 (335.9)	27 (335.8)

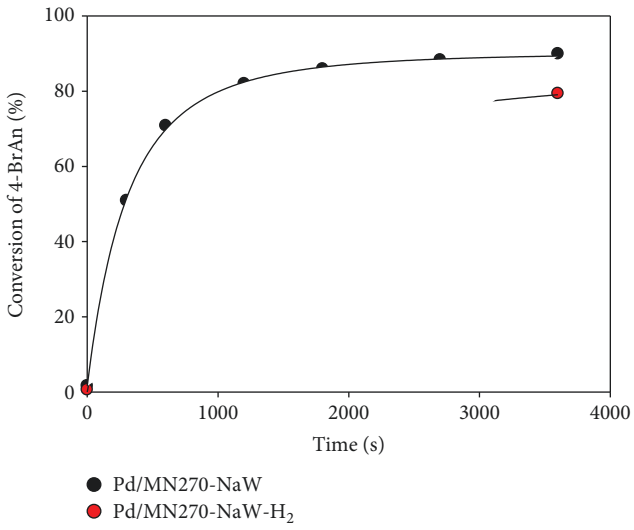

Figure 4: Kinetic curves of 4-BrAn conversion obtained while using Pd/MN270-NaW and Pd/MN270-NaW-H_2 in Suzuki cross-coupling.

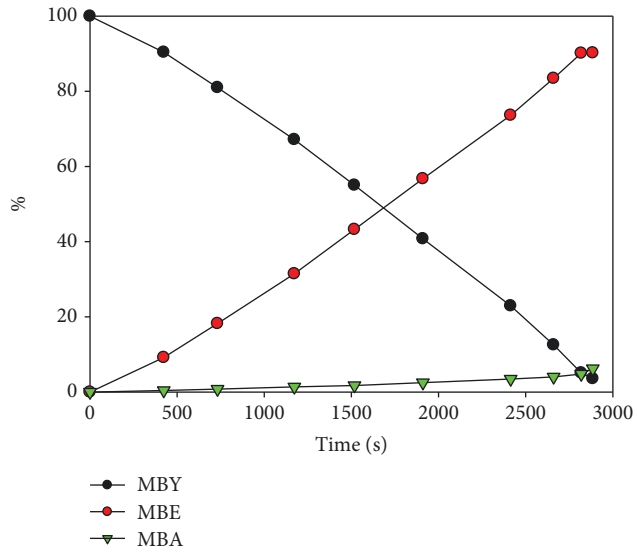

Figure 5: Kinetic curves obtained while using Pd/MN270-NaW in MBY hydrogenation.

comparison with a reported earlier result for preliminarily reduced MN100-based sample, for which conversion of 4-BrAn was only about 58% [9].

3.3. Hydrogenation of MBY. Results of testing of Pd/MN270-NaW in MBY hydrogenation (Figure 1(b)) are presented in Figure 5. As it can be seen, MBY hydrogenation occurs according to the classical Langmuir-Hinshelwood kinetics observed for triple bond semihydrogenation [18, 19] with slight induction period. These results suggest that Pd NPs were mostly formed (during H_2 liquid-phase reduction of Pd/MN270-NaW at conditions of MBY hydrogenation) and probably are responsible for observed catalytic activity.

Recently, we have found that the presence of alkali metals strongly influences the behavior (activity and selectivity) of hydrogenation catalysts synthesized while using chloride-containing Pd salt [10]. Moreover, the sample treatments after impregnation with sodium carbonate accelerates precursor decomposition rendering Pd oxide and Pd NPs (see the results of XPS data). In order to verify if this treatment is necessary, we compared the activity of Pd/MN270 and Pd/MN270-H_2 with that of Pd/MN270-NaW and the results are presented in Table 2.

As it can be seen from Table 2, the sodium carbonate treatment of the Pd catalyst prepared with HPS of MN270 type by impregnation with Pd acetate as a precursor has

Table 2: Results of testing of HPS-based catalysts in MBY hydrogenation: influence of reduction method and treatment of the catalyst with Na_2CO_3.

Catalyst	Selectivity, ±0.5% (calculated at MBY conversion 95%)	Catalytic activity *R*, molMBY/(molPd*s)
Pd/MN270-NaW	94.6	3.2
Pd/MN270	95.2	3.7
Pd/MN270-H_2	96.0	3.1
Pd/MN270-H_2 without preliminarily liquid-phase reduction	95.4	3.4

almost no influence on the observed activity (*R*). The selectivity also remains the same with the value of about 95-96% at 95% of MBY conversion. That means that Pd NPs responsible for catalysis are easily formed under reaction conditions as well as during gas-phase reduction in hydrogen flow (see also TEM data). Moreover, for the sample Pd/MN270-H_2, it was also shown that its pretreatment in-situ is not necessary (see Table 2 and Figure 6), which is also proven by linear dependence of hydrogen uptake on MBY conversion.

Thus, the procedure of catalyst synthesis based on impregnation of MN270 with $Pd(CH_3COO)_2$ can be

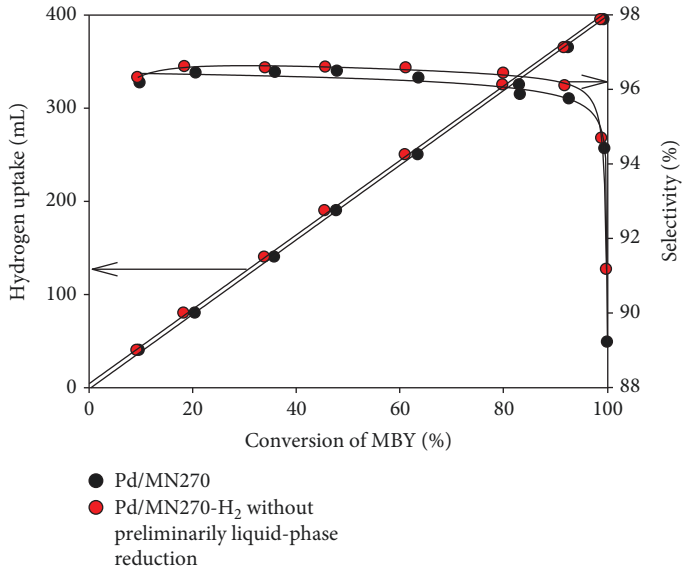

Figure 6: Influence of reduction method on selectivity to MBE and hydrogen uptake.

simplified, because such combination of HPS type and palladium precursor allows easy formation of Pd NPs *in situ* under reaction conditions without any additional treatment. It is important to underline that activity of Pd/MN270 catalyst is about 35% higher as compared to industrial Lindlar catalyst (2%-Pd/$CaCO_3$, 2.4 molMBY/molPd*s), which presents comparable (94.6%) selectivity to MBE.

4. Conclusions

Formation of Pd NPs of about 3-4 nm and relatively narrow particle size distributions were shown to proceed very fast in nonfunctionalized HPS of MN270 type after impregnation by Pd acetate and be independent on reduction method with molecular hydrogen (gas-phase at 300°C or liquid-phase *in situ* under reaction conditions at 90°C). Moreover, in contrast to analogous catalysts impregnated with chloride-containing palladium salts, the Pd/MN270 sample does not need any pretreatment with alkali metal compounds (such as Na_2CO_3) simplifying the catalyst synthesis. Pd NPs stabilized within MN270 catalyze effectively Suzuki cross-coupling allowing 90% conversion of 4-BrAn and have about 35% higher activity as compared to industrial Lindar catalyst in selective hydrogenation of MBY.

Data Availability

The data used to support the findings of this study are available from the corresponding author upon request.

Conflicts of Interest

The authors declare that they have no conflicts of interest.

Acknowledgments

Financial support was provided by the Russian Science Foundation (project 15-19-20023).

Supplementary Materials

Figure S1: normalized DRIFT spectra of initial MN270 and Pd/MN270-NaW (as synthesized and reduced in H_2 flow). Figure S2: high resolution spectra of Pd 3d of freshly prepared Pd/MN270 (a) and Pd/MN270-NaW (b) and reduced in H_2 flow Pd/MN270-H_2 (c) and Pd/MN270-NaW-H_2 (d). *(Supplementary Materials)*

References

[1] G. Schmid, Ed., *Nanoparticles: From Theory to Application*, Wiley-VCH Verlag GmbH & Co. KGaA, Weinheim, Germany, 2004.

[2] G. A. Somorjai, A. M. Contreras, M. Montano, and R. M. Rioux, "Clusters, surfaces, and catalysis," *Proceedings of the National Academy of Sciences*, vol. 103, no. 28, article 10577, 10583 pages, 2006.

[3] L. Liu and A. Corma, "Metal catalysts for heterogeneous catalysis: from single atoms to nanoclusters and nanoparticles," *Chemical Reviews*, vol. 118, no. 10, pp. 4981–5079, 2018.

[4] B. R. Cuenya, "Synthesis and catalytic properties of metal nanoparticles: size, shape, support, composition, and oxidation state effects," *Thin Solid Films*, vol. 518, no. 12, pp. 3127–3150, 2010.

[5] J. M. Campelo, D. Luna, R. Luque, J. M. Marinas, and A. A. Romero, "Sustainable preparation of supported metal nanoparticles and their applications in catalysis," *ChemSusChem*, vol. 2, no. 1, pp. 18–45, 2009.

[6] D. Astruc, F. Lu, and J. R. Aranzaes, "Nanoparticles as recyclable catalysts: the frontier between homogeneous and

heterogeneous catalysis," *Angewandte Chemie, International Edition*, vol. 44, pp. 7852–7872, 2005.

[7] A. Balanta, C. Godard, and C. Claver, "Pd nanoparticles for C–C coupling reactions," *Chemical Society Reviews*, vol. 40, no. 10, pp. 4973–4985, 2011.

[8] L. D. Pachón and G. Rothenberg, "Transition-metal nanoparticles: synthesis, stability and the leaching issue," *Applied Organometallic Chemistry*, vol. 22, no. 6, pp. 288–299, 2008.

[9] N. A. Nemygina, L. Z. Nikoshvili, A. V. Bykov et al., "Catalysts of suzuki cross-coupling based on functionalized hyper-crosslinked polystyrene: influence of precursor nature," *Organic Process Research and Development*, vol. 20, no. 8, pp. 1453–1460, 2016.

[10] L. Z. Nikoshvili, A. V. Bykov, T. E. Khudyakova et al., "Promotion effect of alkali metal hydroxides on polymer-stabilized pd nanoparticles for selective hydrogenation of C–C triple bonds in alkynols," *Industrial and Engineering Chemistry Research*, vol. 56, no. 45, pp. 13219–13227, 2017.

[11] E. M. Sulman, L. Z. Nikoshvili, V. G. Matveeva et al., "Palladium containing catalysts based on hypercrosslinked polystyrene for selective hydrogenation of acetylene alcohols," *Topics in Catalysis*, vol. 55, no. 7-10, pp. 492–497, 2012.

[12] N. A. Nemygina, L. Z. Nikoshvili, V. G. Matveeva, M. G. Sulman, E. M. Sulman, and L. Kiwi-Minsker, "Pd-nanoparticles confined within hollow polymeric framework as effective catalysts for the synthesis of fine chemicals," *Topics in Catalysis*, vol. 59, no. 13-14, pp. 1185–1195, 2016.

[13] M. Eggersdorfer, D. Laudert, U. Létinois et al., "One hundred years of vitamins-A success story of the natural sciences," *Angewandte Chemie, International Edition*, vol. 51, no. 52, pp. 12960–12990, 2012.

[14] M. Pérez-Lorenzo, "Palladium nanoparticles as efficient catalysts for suzuki cross-coupling reactions," *Journal of Physical Chemistry Letters*, vol. 3, no. 2, pp. 167–174, 2012.

[15] T. Wu, W. E. Kaden, W. A. Kunkel, and S. L. Anderson, "Size-dependent oxidation of Pd_n ($n \lesssim 13$) on alumina/NiAl(110): correlation with Pd core level binding energies," *Surface Science*, vol. 603, no. 17, pp. 2764–2770, 2009.

[16] C. D. Wagner, W. M. Riggs, L. E. Davis, J. F. Moulder, and G. E. Muilenberg, *Handbook of X-ray photoelectron spectroscopy*, Perkin-Elmer Corporation, 1979, NIST X-ray Photoelectron Spectroscopy Database, Version 3.5.

[17] D. B. Eremin and V. P. Ananikov, "Understanding active species in catalytic transformations: From molecular catalysis to nanoparticles, leaching, "Cocktails" of catalysts and dynamic systems," *Coordination Chemistry Reviews*, vol. 346, pp. 2–19, 2017.

[18] N. Semagina, E. Joannet, S. Parra, E. Sulman, A. Renken, and L. Kiwi-Minsker, "Palladium nanoparticles stabilized in block-copolymer micelles for highly selective 2-butyne-1,4-diol partial hydrogenation," *Applied Catalysis A: General*, vol. 280, no. 2, pp. 141–147, 2005.

[19] S. Vernuccio, A. Meier, and P. R. von Rohr, *Industrial and Engineering Chemistry Research*, vol. 56, no. 17, pp. 4929–4937, 2017.

Hindawi
Journal of Nanomaterials
Volume 2018, Article ID 9456971, 8 pages
https://doi.org/10.1155/2018/9456971

Research Article

Micromorphology and Mechanical and Dielectric Properties of Bismaleimide Composite Modified by Multiwalled Carbon Nanotubes and Polyethersulfone

Yufei Chen,[1,2] **Chengbao Geng**,[2] **Yang Han**,[2] **Mingzhuo Chai**,[2] **Hongyuan Guo**,[2] **Chunyan Yue**,[2] **and Yingyi Ma**[2]

[1]*Key Laboratory of Engineering Dielectrics and Its Application, Ministry of Education, Harbin University of Science and Technology, Harbin 150080, China*
[2]*The College of Materials Science and Engineering, Harbin University of Science and Technology, Harbin 150040, China*

Correspondence should be addressed to Yufei Chen; chenyufei@hrbust.edu.cn

Received 19 June 2018; Revised 19 September 2018; Accepted 4 October 2018; Published 19 November 2018

Guest Editor: Bathula Babu

Multiwalled carbon nanotubes (MWCNTs) were modified by oxidizing agent to obtain O-MWCNTs, and the surface of it was coated with active group. 4,4′-Diaminodiphenylmethane bismaleimide (MBMI) was used as matrix, 3,3′-diallyl bisphenol A (BBA) and bisphenol-A diallyl ether (BBE) were used as reactive diluent, polyethersulfone (PES) as toughening agent, and O-MWCNTs as modifier; OMWCNT/PES-MBAE composite was prepared through in situ sol-gel method. The effect of PES and OMWCNTs on the mechanical and dielectric properties of composite was analyzed, and the microstructure was examined by transmission electron microscope (TEM) and scanning electron microscope (SEM). The mechanism of composite toughened by PES and OMWCNTs was observed and analyzed. The results showed that Diels-Alder reaction between MBMI and allyl compounds occurred completely and unsaturated double bond disappeared. O-MWCNTs and PES resin dispersed smoothly in polymer matrix and were used as reinforcement, and PES resin and O-MWCNTs could synergistically improve the properties of the composite and exhibited a typical ductile fracture. The impact and bending strengths were 16.09 kJ/m^2 and 153.57 MPa, which were 74.32% and 53.08% higher than those of the MBAE matrix, respectively, and the dielectric constant and the dielectric loss were 3.76 (100 Hz) and 2.79×10^{-3} (100 Hz), when the content of PES was 2 wt% and O-MWCNTs was 0.02 wt%. The outstanding properties of the material made it play an important role in high-performance insulating material applications.

1. Introduction

Bismaleimide (BMI) is a kind of outstanding polymer matrix; due to its excellent processability, heat resistance, radiation resistance, and good insulation properties, it is widely used in aerospace field and electrical insulating materials, such as aircraft floor, isolation wall, exhaust system and piping, and other components. In addition, combined with carbon fiber, it can also be used for aircraft bearing or nonbearing structural parts, wing skin, tail, aircraft fuselage, and skeleton. However, unmodified BMI cannot meet the requirements of processing and using; due to its high brittleness and bad shock resistance, the toughening modification of BMI resin is a hot topic all the time [1, 2]. Li et al. reported that PDMS-AN/BDM composite has a flexural strength of 80.74 MPa, a flexural modulus of 3294.72 MPa, and an impact strength of 8.06 kJ/m^2 [3]. Ji and coworkers reported that a reactive hyperbranched polysiloxane (HPSiE) terminated by epoxy groups was designed and synthesized to develop a novel high-performance modified bismaleimide-triazine resin, resulting in an impact strength of 16.5 kJ/m^2 [4]. Yan et al. prepared novel bismaleimide nanocomposites with Si_3N_4 nanoparticles; the highest impact strength and flexural strength were 15 kJ/m^2 and 85 MPa, respectively [5]. These studies have improved the properties of bismaleimide resin to some extent. Polyethersulfone (PES) is one of the most widely used special engineering plastics; it has excellent heat resistance, physical and mechanical properties,

insulation properties, and so on; and it can keep the stability of performance at high temperatures and can be usually used as a toughening agent to improve the toughness of BMI resin [6, 7].

In recent years, carbon nanotechnology has been the focus of research and is widely used in many fields, due to their excellent physical and chemical properties, and the development of carbon nanomaterials has promoted the progress in materials, medicine, chemical engineering, artificial intelligence, and other fields. Multiwalled carbon nanotube (MWCNT) is a new type of high-strength carbon material, which has unusual mechanical, electrical, and chemical properties, and it is usually used as effective reinforcement of the composite; exhibits good strength, elasticity, fatigue resistance, and isotropy; and greatly improves the performances of the composite [8–10]. Unmodified MWCNTs are prone to reunite in the polymer matrix, so the modification of MWCNTs is very important [11, 12]. In this paper, multiwalled carbon nanotubes (MWCNTs) were modified by concentrated sulfuric acid to obtain O-MWCNTs. 4,4′-Diaminodiphenylmethane bismaleimide (MBMI) was used as matrix, 3,3′-diallyl bisphenol A (BBA) and bisphenol-A diallyl ether (BBE) were used as reactive diluent to synthesize polymer matrix (MBAE), polyethersulfone (PES) was used as toughening agent, and OMWCNTs was used as modifier; O-MWCNT/PES-MBAE composite was prepared through in situ sol-gel method. And then, the morphology of MWCNTs and O-MWCNT/PES-MBAE composite was observed by TEM and SEM, respectively. Furthermore, the mechanical and dielectric properties of the composite were discussed; PES and O-MWCNTs have a good compatibility with the resin matrix and can synergistically toughen the resin matrix. The study can provide a valuable reference for further application of BMI resin in the engineering field.

2. Experimental

2.1. Materials. Multiwalled carbon nanotubes (MWCNTs) were purchased from Guangzhou Hongwu Material Technology Co. Ltd. (CHN); the diameter is 40–60 nm, and the length is 5–15 μm. 4,4′-Diaminodiphenylmethane bismaleimide (MBMI), a yellow powder with a melting point of 155°C, has a density of 1.43 g/cm^3. 3,3′-diallyl bisphenol A (BBA) and bisphenol-A diallyl ether (BBE) were all purchased from Laizhou Laiyu Chemical Co. Ltd. (CHN); BBA is a light yellow liquid with a density of 1.08 g/cm^3, and BBE is a colorless liquid with a density of 1.03 g/cm^3. Polyethersulfone (PES) was from Changchun Jida Special Plastic Engineering Co. Ltd. (CHN); the molecular weight is 30,000; the intrinsic viscosity is 0.32; and the continuous use temperature is about 180–200°C. Concentrated sulfuric acid (H_2SO_4) and concentrated nitric acid (HNO_3), chemically pure, were purchased from Shanghai Chemical Reagent Factory (CHN).

2.2. Modification of MWCNTs. Four grams of pristine MWCNTs and 100 ml solution of sulfuric acid and nitric acid mixture with a volume ratio of 3 : 1 were added into a round bottom flask, MWCNT/acid mixture flask was sonicated for 20 min in an ultrasonic bath at 70°C in order to prevent agglomeration of MWCNTs, then the cooled mixture was diluted with deionized water and washed subsequently until the pH value was about 7, and finally O-MWCNTs were obtained by the removal of residual solvent under vacuum.

Table 1: The type and component of the composite.

Number of samples	Component	PES content (wt%)	O-MWCNT content (wt%)
A	MBAE	0	0
B0	PES-MBAE	2	0
B1	MWCNTs/PES-MBAE	2	0.01
B2	MWCNTs/PES-MBAE	2	0.02
B3	MWCNTs/PES-MBAE	2	0.03
B4	MWCNTs/PES-MBAE	2	0.04

2.3. Preparation of O-MWCNT/PES-MBAE Composite. The mixed solution of BBA and BBE was gotten in a mass ratio of 3 : 2, transferred to a three-necked flask, and stirred for 15 min at 70°C in an ultrasonic cleaner; O-MWCNTs were added into the solution and stirred for 2 h. Then, PES resin was added into the mixture at 170°C and finally stirred until they were dispersed evenly. MBMI was dispersed in the above solution at 130°C and obtained a uniform mixture, and the mixture was removed to a preheated mold and was in a vacuum oven. The curing process was carried out at five steps; 130°C/1 h, +150°C/1 h, +180°C/1 h, +200°C/1 h, and +230°C/1 h. The samples were numbered as in Table 1.

2.4. Measurements. The surface morphology of O-MWCNTs and composites were characterized by transmission electron microscope (TEM, JEM-2100 UHR, JEOL Ltd., Tokyo, Japan) and by scanning electron microscope (SEM, JAPA). Samples were deposited on a sample holder with adhesive carbon foil and were sputtered with gold.

The FT-IR spectra, which were used to study the chemical structure of the materials, were performed with an Equinox-55 Fourier-transform spectrometer (GER), in the 400–4000 cm^{-1} range. And it could be seen that there existed the characteristic absorption peaks of the materials.

The impact strength of specimens was tested by Charpy impact machine tester (Jinan Huaxing Laboratory Equipment Co. Ltd.), according to the standard of GB/T 2567-2008, and the specimens needed no bubbles, cracks, scars, and other defects. For each sample, five measurements were made at least and the average value was taken; the test was carried out at room temperature.

The bending strength of samples was tested by CSS-44300 electronic testing machine (Shanghai Technical Instrument Co. Ltd., CHN) according to the standard of GB/T 2567-2008. Standard of bending strength experiments was performed at room temperature, with a speed of 2 mm/min. For each sample, five measurements were made at least and the average value was taken.

Dielectric constant (ε) and dielectric loss (tanδ) of the composite material were measured with Agilent-4292A

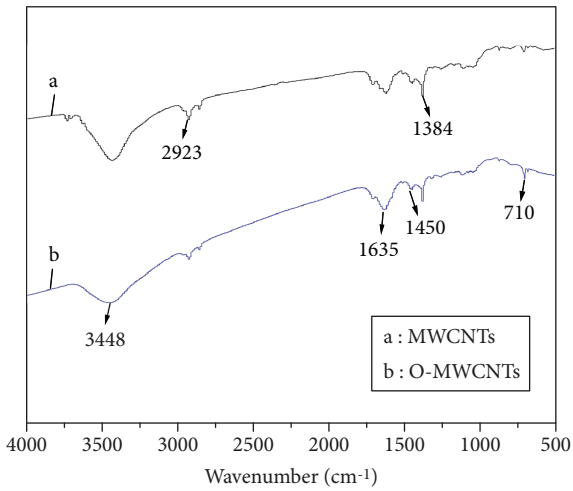

Figure 1: FT-IR spectra of MWCNTs.

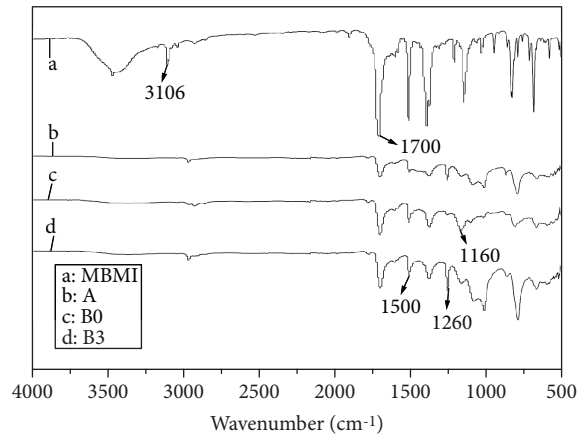

Figure 2: FT-IR spectra of the composite.

precise impedance analyzer (Japan) in the frequency range of 100 Hz–100 kHz at room temperature according to GB/T 1409-2006.

3. Results and Discussions

3.1. FT-IR Spectral Analysis. FT-IR spectra of MWCNTs and O-MWCNTs were presented in Figure 1. The peak at 1450 cm^{-1} was the stretching vibration of carbon skeleton, and the peaks at 2923 cm^{-1} and 1384 cm^{-1} were the asymmetrical stretching vibration of -CH_2- and the symmetrical bending vibration of -CH_3-, respectively. The broad peak at 3448 cm^{-1} was the stretching vibration of intermolecular associative -OH in curve b, and the peaks at 1635 cm^{-1} and 710 cm^{-1} were the stretching vibration of -C=O and S-O, respectively. It revealed that a certain amount of carboxyl groups has been deposited in the surface of O-MWCNTs [13].

FT-IR spectra of materials were exhibited in Figure 2. The curves a, b, c, and d represented MBMI resin, MBAE matrix, PES-MBAE, and O-MWCNT/PES-MBAE composite, respectively.

In curve a, the peak at 3106 cm^{-1} was caused by the stretching vibration of C=C in MBMI; however, this characteristic peak vanished in curves b, c, and d. The emergence of this phenomenon corroborated that the Diels-Alder reaction between MBMI and allyl compounds has taken place [14]. In curves a, b, c, and d, the peaks at 1700 cm^{-1} and 1500 cm^{-1} were the stretching vibration of C=O and the stretching vibration of C=C in the benzene ring skeleton, respectively. The peak at 1160 cm^{-1} was the stretching vibration of O=S=O in curves c and d. The peak of curve d at 1260 cm^{-1} was caused by the stretching vibration of C-O and indicated that the O-MWCNTs have been doped to the composite [15]. The results of FT-IR spectra suggested that O-MWCNT/PES-MBAE composite has been prepared successfully.

3.2. Analysis of TEM Patterns. The micromorphology of MWCNTs and O-MWCNTs was investigated by TEM in Figure 3, so as to observe the effect of modification and verify the above results.

Figure 3 displayed the TEM images of MWCNTs and O-MWCNTs; Figure 3(a) shows the MWCNTs; Figures 3(b) and 3(c) show the O-MWCNTs, the magnification was 4×10^4 times and 1×10^4 times, respectively; and Figure 3(d) image shows the energy spectrum of the selected region. In Figure 3(a), it would be seen that MWCNTs were scrolls and intertwined and exhibited nanowire-like morphology and a smooth surface with nothing adhering to them, as it was a stable structure of C=C bond and had no active group. The oxidation of MWCNTs by strong acid treatment significantly alters the surface roughness of nanotubes. Figures 3(b) and 3(c) showed that the reunion of O-MWCNTs weakened, the ratio of length and diameter did not change, and its walls became rough and had many active cross-linking points; this was because there were more defects on its surface; hydroxy groups and carboxyl groups appeared at the defects to form active cross-linking points [16]. The energy spectrum was used to analyze element component in order to explore the function of modification. Figure 3(d) shows the energy-spectra of O-MWCNTs; the surface of the marked area was broken and formed hollow. In the selected area, C element was dominant; the weight ratio of N, O, and S elements was lower, 1.7 wt%, 2.7 wt%, and 0.3 wt%; the nitrified degree and sulfonated degree were about 7.65% and 0.92%, respectively. It is indicated that the surface of O-MWCNTs had active groups of $-SO_3H$ and $-NO_2$; these polar groups could make the compatibility better between MWCNTs and resin matrix and do not destroy the structure of MWCNTs [17, 18].

3.3. Analysis of SEM Patterns. The microscale cross-section morphology of the material could be studied by the SEM, and the pictures of the composite were shown in Figure 4. Figures 4(a) and 4(b) show the morphology of sample A, Figures 4(c) and 4(d) show sample B0, and Figures 4(e) and (f) show sample B2. Figures 4(a) and 4(b) showed that the fracture surface of sample A had no obvious microcracks and was a typical morphology of brittle fracture; the reason

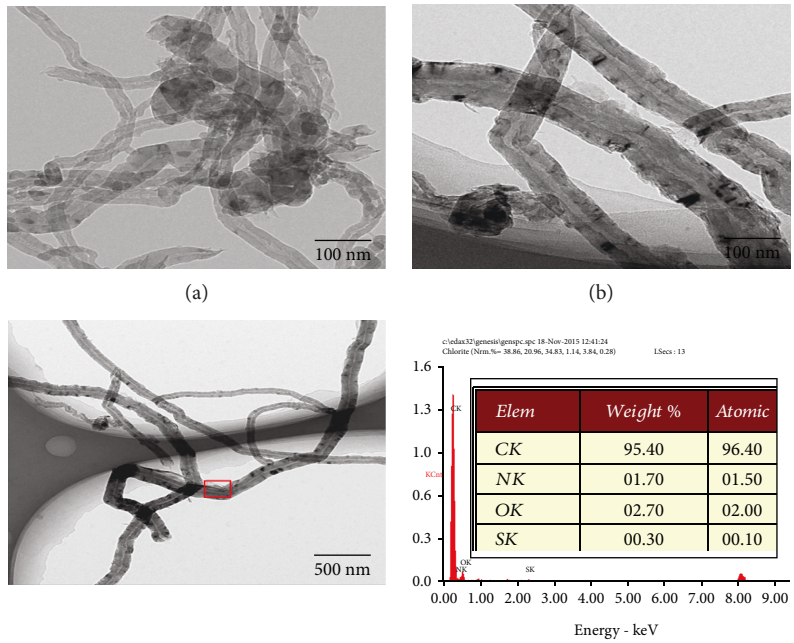

Figure 3: TEM patterns and energy spectrum of MWCNTs.

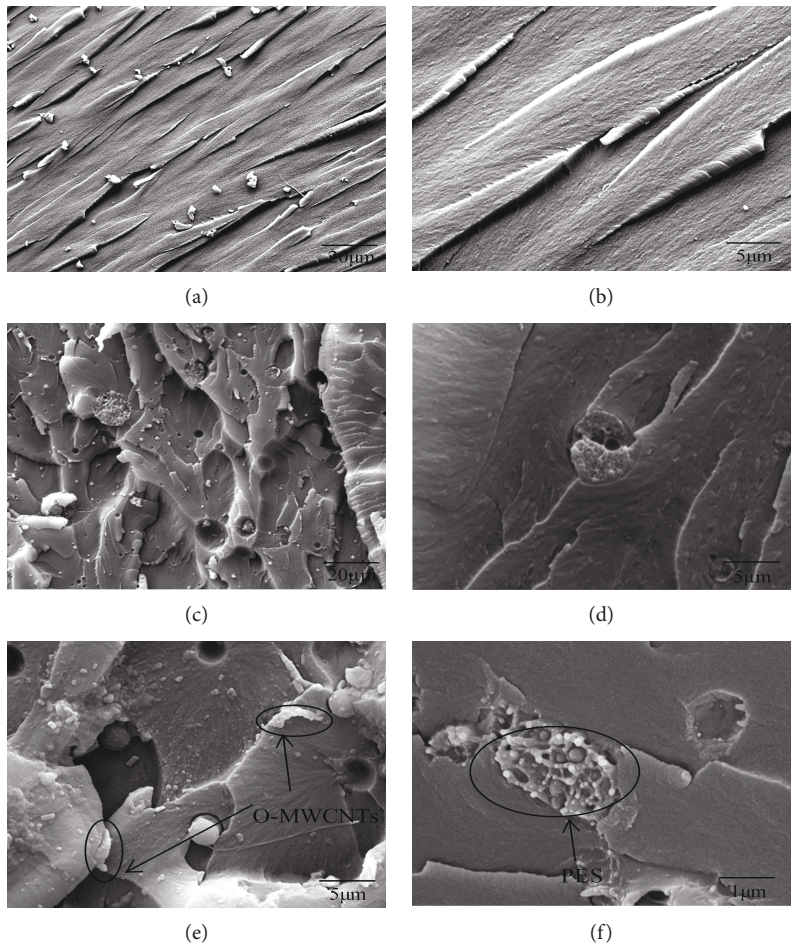

Figure 4: SEM photographs of the composite: (a) A ×1000, (b) A ×5000, (c) B0 ×1000, (d) B0 ×5000, (e) B2 ×5000, and (f) B2 ×20,000.

was that the chemical structure of MBMI was symmetric and the crystallinity could lead the material to become brittle. There existed many "honeycombs" in Figures 4(c) and 4(d); the size of its scale was about 5 μm and it was a PES resin [19]. It could be seen that the PES particles were inlaid in the matrix and presented as a two-phase structure in the composite. The cross-section surface of PES-MABE had obvious microcracks, and the fracture was ductile; the main reason was that the PES phase evenly dispersed in continuous MABE phase and the interaction between two phases was strong. The material would crack along the direction of the force when the composite suffered external force; a great number of microcracks formed as the interface function between two phases combined well and played a role of toughening effects [20, 21]. The formation of microcracks and shear zone could absorb a quantity of energy and cause a ductile fracture.

SEM pictures of sample B2 were displayed in Figures 4(e) and 4(f); it could be distinctly seen that PES resin and O-MWCNTs were uniformly dispersed in the matrix; due to the presence of active groups on the surface of O-MWCNTs, these groups could cross-bond with polar groups of the matrix and PES resin [22], and O-MWCNTs and PES resin had synergistical toughening effects. The mutual entanglement between MWCNTs was weakened, and the interaction with the matrix was enhanced, thereby, to improve the dispersion of the PES resin in the matrix. In addition, there are mutual infiltration and interpenetration between PES resin and the matrix. When the PES phase encountered the external force during the fracture process, the cracks were passivated, and the direction of the cracks had changed. This effect was beneficial to improve the performance of the composite; meanwhile, there are polar groups on the surface of O-MWCNTs and PES resin, and they would form a synergistic effect [23–25]. When the composite suffered external force, this synergistic effect would hinder the development of microcracks and absorb a quantity of energy to enhance the interaction between the phase interfaces. Therefore, the composite of O-MWCNTs/PES-MBAE exhibited a typical ductile fracture.

3.4. Mechanical Properties of Composite. Impact strength and bending strength were two important indicators of mechanical properties; their results were shown in Table 2. Their tendency was increased first and then decreased, and the properties of sample B2 was the best; impact strength and bending strength were 16.09 kJ/m^2 and 153.57 MPa, which were higher by 74.32% and 53.08% than that of sample A, respectively. This indicated that PES resin and O-MWCNTs had a great influence on the mechanical properties of composites to some extent. The main reasons were that the PES resin could disperse in the polymer matrix and present a two-phase structure according to the SEM results, and the toughening theory of PES accorded with outside toughening mechanism; the interfaces formed due to the interaction among continuous phase (MBAE), PES, and O-MWCNTs. Additionally, O-MWCNTs had good compatibility with the system and could be evenly dispersed in the matrix resin and simultaneously formed a synergistic effect with the PES resin. The interaction among three components was enhanced, which effectively prevented the development of cracks and absorbed more energy when the material was broken. In the bending process of material, the external force firstly caused stress yield and a large number of silver streak and microcracks appeared inside the material and finally formed a macroscopic fracture [26]. O-MWCNTs could effectively suppress the development of microcracks in the yielding process of material and could block the microcracks and change its developing direction to make the microcracks develop irregularly; when the silver streak or microcracks appeared, it was beneficial to improve the mechanical properties of the composite.

Table 2: Impact strength and bending strength of the composite.

Type	Impact strength (kJ/m^2)	Increasing rate (%)	Bending strength (MPa)	Increasing rate (%)
A	9.23	0	100.32	0
B0	10.36	12.24	117.36	16.99
B1	13.37	44.85	124.09	23.69
B2	16.09	74.32	153.57	53.08
B3	14.41	56.12	128.64	28.22
B4	12.73	37.92	121.04	20.65

3.5. Dielectric Properties of Composite. Dielectric constant and dielectric loss were two important characteristic indicators of the dielectric materials. The internal factors of influencing dielectric constant were the condition of dielectric polarization and polarization divided into electronic polarization, atomic polarization, orientation polarization, and interfacial polarization according to different molecular polarization mechanisms. The dielectric constant of polar molecule depended on the orientation polarization and increased with the increasing of polarization extent. Figure 5 displayed the dielectric constant curves of the composite. The permittivity of the composite decreased gradually with the increasing frequency (from 10^2 to 10^6 Hz); nevertheless, the rate of descent was accelerated when the frequency was over 10^4 Hz. At low frequency, the dielectric constant varied slowly, the period of the variation was much longer than the relaxation time, and the polarization was completely comparable to the electric field. At high frequency, the electric field varied rapidly, the period was very short and almost much shorter than the relaxation time, the relaxation polarization could not keep up with the variation of the electric field, and the instantaneous polarization occurred; it led to the decrease of the permittivity [27].

The permittivity of sample B0 was higher than that of sample A. On the one hand, the PES resin contained polar groups and the density of the polar groups increased. On the other hand, the PES resin formed an interface with the matrix resin, which could absorb a large amount of charge and initiate interface polarization; therefore, the permittivity of materials increased slightly.

The dielectric constant of O-MWCNT/PES-MBAE composite was lower than that of sample B0, and sample A was

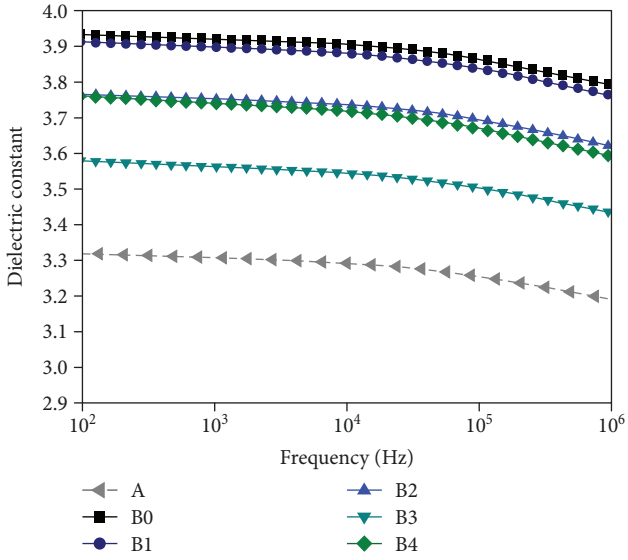

Figure 5: Dielectric constant of the composite.

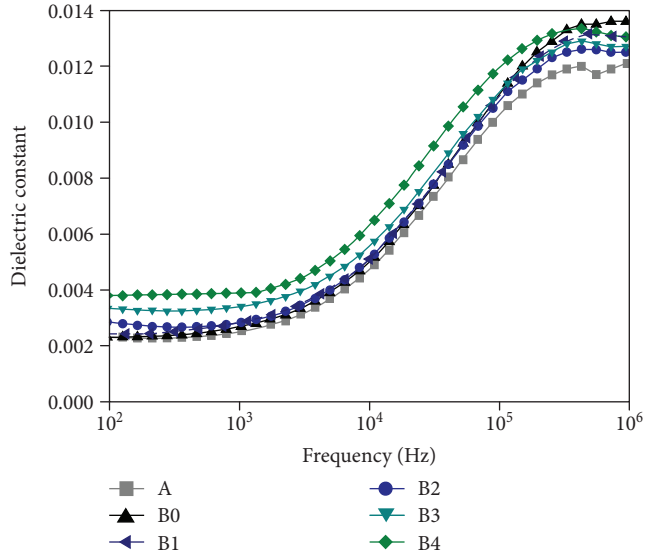

Figure 6: Dielectric loss of the composite.

the lowest at the same frequency. Commonly, the addition of O-MWCNTs would increase the conductivity and decrease the dielectric constant. However, with the increase of O-MWCNT doping content, the binding density increased, the chain segment motion of polymer was hindered by the binding entanglement effect, and the orientation polarization of the dipole in the system was restrained. Due to a little doping amount of O-MWCNTs, the effect of binding entanglement played a dominant role, resulting in the decrease of dielectric constant [28]. When the content of O-MWCNTs was 0.04 wt%, the interface interaction between the O-MWCNTs and the resin matrix increased, the binding effect of carriers in the interface overlap region was weakened, the interfacial polarization was enhanced, and the migration of carriers became easy, so the permittivity of materials increased.

Figure 6 showed the dielectric loss curves of the composite; the frequency was from 10^2 Hz to 10^6 Hz. The dielectric loss of the composite was 0.002 to 0.004 with the slight fluctuation at low frequency (10^2–10^3 Hz), but the dielectric loss increased rapidly at 10^3 Hz–10^5 Hz. The reasons were probably that the polarization could completely keep up with the change of the electric field at low frequency, and the absorbed energy could be returned to the electric field in time, so the dielectric loss was smaller. At high frequency, the orientation polarization needed to overcome the internal resistance of the material, while the dipole steering lagged behind the variation of the electric field and the relaxation phenomenon was obvious [29]. When the frequency was adequately high, the orientation polarization needed a long time in the relaxation process, so the variation of the dielectric loss was small at this time.

The dielectric loss of sample A was the lowest, sample B0 was the second, and the dielectric loss of O-MWCNTs/PES-MBAE composite was slightly higher than that of the others at the same frequency. This phenomenon could be explained as follows: the cross-linking density declined because the PES resin presented as a two-phase structure in the matrix, and the friction resistance increased due to the interaction between PES and matrix. A large number of interfaces were formed, which caused the dipole's steering to be suppressed, and more energy was required to overcome the friction resistance. At the same time, the PES resin carried with polar groups and the relaxation polarization ability increased, so the dielectric loss of sample B0 increased [30, 31]. Additionally, O-MWCNTs may carry with carriers to material and generate a conductive current when the electric field was applied to the composite. Therefore, the dielectric loss increased with the addition of O-MWCNTs. Because the content of O-MWCNTs was very low, the dielectric loss was still ideal, and the insulation performance of the composite material could meet the applied requirement.

4. Conclusions

O-MWCNTs have good compatibility with the polymer matrix, the Diels-Alder reaction between MBMI and allyl compounds has taken place, and the O-MWCNT/PES-MBAE composite has been prepared. PES resin evenly disperses in a "honeycomb" two-phase structure in the MBAE matrix. PES resin and O-MWCNTs can synergistically toughen the composite, and O-MWCNTs/PES-MBAE composite exhibits a typical ductile fracture. The comprehensive performance of O-MWCNT/PES-MBAE composite is the best when the content of PES resin is 2 wt% and O-MWCNTs is 0.02 wt%; the impact and bending strengths are 16.09 kJ/m^2 and 153.57 MPa, which are 74.32% and 53.08% higher than those of MBAE matrix, respectively. The permittivity and the dielectric loss of O-MWCNT/PES-MBAE composite are 3.76 (100 Hz) and 2.79×10^{-3} (100 Hz). O-MWCNTs could greatly improve the mechanical properties of the composite material, and its dielectric properties have decreased slightly; its performance could meet the requirement of insulating material.

Data Availability

All data included in this study are available upon request by contact with the corresponding author.

Conflicts of Interest

The authors declare that there is no conflict of interests regarding the publication of this paper.

Acknowledgments

The authors would like to express their appreciation to the project support by the Natural Science Foundation of China (21604019) and the Harbin Technology Bureau Subject Leader (2015RAXXJ029).

References

[1] Z. Yian, W. Zhiying, S. L. Keey, and C. G. Boay, "Long-term viscoelastic response of E-glass/bismaleimide composite in seawater environment," *Applied Composite Materials*, vol. 22, no. 6, pp. 693–709, 2015.

[2] H. Yan, R. Ning, G. Liang, Y. Huang, and T. Lu, "The effect of silane coupling agent on the sliding wear behavior of nanometer ZrO_2/bismaleimide composites," *Journal of Materials Science*, vol. 42, no. 3, pp. 958–965, 2007.

[3] W. Li, F. Liu, L. Wei, and T. Zhao, "Synthesis, morphology and properties of polydimethylsiloxane-modified allylated novolac/4,4′-bismaleimidodiphenylmethane," *European Polymer Journal*, vol. 42, no. 3, pp. 580–592, 2006.

[4] L. Ji, A. Gu, G. Liang, and L. Yuan, "Novel modification of bismaleimide–triazine resin by reactive hyperbranched polysiloxane," *Journal of Materials Science*, vol. 45, no. 7, pp. 1859–1865, 2010.

[5] H. Yan, L. Pengbo, Z. Junping, and N. Rongchang, "Mechanical properties of novel bismaleimide nanocomposites with Si_3N_4 nanoparticles," *Journal of Reinforced Plastics and Composites*, vol. 29, no. 10, pp. 1515–1522, 2010.

[6] L. Wang, M. He, T. Gong et al., "Introducing multiple biofunctional groups on the poly(ether sulfone) membrane substrate to fabricate an effective antithrombotic bio-interface," *Biomaterials Science*, vol. 5, no. 12, pp. 2416–2426, 2017.

[7] Y. Yu, S. Wang, J. Shao, Y. Zhou, and C. Gao, "Effect of the drying temperature on sulfonated polyether sulfone nanofiltration membranes prepared by a coating method," *Journal of Coatings Technology and Research*, vol. 15, no. 2, pp. 425–435, 2018.

[8] A. Abdolmaleki, S. Mallakpour, and M. Rostami, "Performance evaluation of fructose-functionalized multiwalled carbon nanotubes/biodegradable poly(amide–imide) based on *N,N′*-(pyromellitoyl)-bis-*S*-valine bionanocomposite," *High Performance Polymers*, vol. 27, no. 8, pp. 903–910, 2015.

[9] Q. W. Li, Y. Li, X. F. Zhang et al., "Structure-dependent electrical properties of carbon nanotube fibers," *Advanced Materials*, vol. 19, no. 20, pp. 3358–3363, 2007.

[10] M. Alsawat, T. Altalhi, K. Gulati, A. Santos, and D. Losic, "Synthesis of carbon nanotube–nanotubular titania composites by catalyst-free CVD process: insights into the formation mechanism and photocatalytic properties," *ACS Applied Materials & Interfaces*, vol. 7, no. 51, pp. 28361–28368, 2015.

[11] C.-C. Hou, S. Cao, W.-F. Fu, and Y. Chen, "Ultrafine CoP nanoparticles supported on carbon nanotubes as highly active electrocatalyst for both oxygen and hydrogen evolution in basic media," *ACS Applied Materials & Interfaces*, vol. 7, no. 51, pp. 28412–28419, 2015.

[12] E. Ramya, N. Momen, and D. N. Rao, "Preparation of multiwall carbon nanotubes with zinc phthalocyanine hybrid materials and their nonlinear optical (NLO) properties," *Journal of Nanoscience and Nanotechnology*, vol. 18, no. 7, pp. 4764–4770, 2018.

[13] L. Zhanjun, C. Hui, W. Jing, X. Xiaohong, L. Hongbo, and Y. Li, "Surface modification of short carbon fibers with carbon nanotubes to reinforce epoxy matrix composites," *Journal of Nanoscience and Nanotechnology*, vol. 18, no. 7, pp. 4940–4952, 2018.

[14] Y. Chen, Z. Li, C. Teng, F. Li, and Y. Han, "Dielectric properties of polyether sulfone/bismaleimide resin composite based on nanolumina modified by super-critical ethanol," *Journal of Electronic Materials*, vol. 45, no. 11, pp. 6026–6032, 2016.

[15] P. Molla-Abbasi, K. Janghorban, and M. S. Asgari, "A novel heteropolyacid-doped carbon nanotubes/Nafion nanocomposite membrane for high performance proton-exchange methanol fuel cell applications," *Iranian Polymer Journal*, vol. 27, no. 2, pp. 77–86, 2018.

[16] S. Versavaud, G. Regnier, G. Gouadec, and M. Vincent, "Influence of injection molding on the electrical properties of polyamide 12 filled with multi-walled carbon nanotubes," *Polymer*, vol. 55, no. 26, pp. 6811–6818, 2014.

[17] P. Chen, Q. Shen, G. Luo, C. Wang, M. Li, and L. Zhang, "Role of interface tailoring by Cu coating carbon nanotubes to optimize Cu–W composites," *Journal of Materials Research*, vol. 30, no. 24, pp. 3757–3765, 2015.

[18] J. Pascual, F. Peris, T. Boronat, O. Fenollar, and R. Balart, "Study of the effects of multi-walled carbon nanotubes on mechanical performance and thermal stability of polypropylene," *Polymer Engineering and Science*, vol. 52, no. 4, pp. 733–740, 2012.

[19] P. Li, T. Li, and H. Yan, "Mechanical, tribological and heat resistant properties of fluorinated multi-walled carbon nanotube/bismaleimide/cyanate resin nanocomposites," *Journal of Materials Science & Technology*, vol. 33, no. 10, pp. 1182–1186, 2017.

[20] G. Wang, R. Wang, G. Fu et al., "Study on phenolphthalein poly(ether sulfone)-modified cyanate ester resin and epoxy resin blends," *Polymer Engineering and Science*, vol. 55, no. 11, pp. 2591–2602, 2015.

[21] Y. Huang, J. Ding, X. Chen, and X. Sun, "Synthesis, mechanical property, and thermal stability of reduced graphene oxide-zinc oxide/cyanate ester/bismaleimide resin composites," *Journal of Adhesion Science and Technology*, vol. 31, no. 12, pp. 1348–1360, 2017.

[22] W. Li, M. Wang, Y. Yue, W. Ji, and R. Ren, "Enhanced mechanical and thermal properties of bismaleimide composites with covalent functionalized graphene oxide," *RSC Advances*, vol. 6, no. 59, pp. 54410–54417, 2016.

[23] R. Konnola, C. P. R. Nair, and K. Joseph, "High strength toughened epoxy nanocomposite based on poly(ether sulfone)-grafted multi-walled carbon nanotube," *Polymers for Advanced Technologies*, vol. 27, no. 1, pp. 82–89, 2016.

[24] A. Reghunadhan, J. Datta, N. Kalarikkal, J. T. Haponiuk, and S. Thomas, "Toughness augmentation by fibrillation and

yielding in nanostructured blends with recycled polyurethane as a modifier," *Applied Surface Science*, vol. 442, pp. 403–411, 2018.

[25] J. Jose, K. Joseph, J:. Pionteck, and S. Thomas, "PVT behavior of thermoplastic poly(styrene-co-acrylonitrile)-modified epoxy systems: relating polymerization-induced viscoelastic phase separation with the cure shrinkage performance," *Journal of Physical Chemistry B*, vol. 112, no. 47, pp. 14793–14803, 2008.

[26] G. Q. Peng, F. H. Shi, Y. F. Wang et al., "Effects of three types of T700 carbon fiber on the mechanical properties of their composites with bismaleimide resin," *New Carbon Materials*, vol. 31, no. 2, pp. 176–181, 2016.

[27] B. Zhang, W. Gao, P. Chu, Z. Zhang, and G. Zhang, "Trap-modulated carrier transport tailors the dielectric properties of alumina/epoxy nanocomposites," *Journal of Materials Science-Materials in Electronics*, vol. 29, no. 3, pp. 1964–1974, 2018.

[28] Y. Wang, K. Kou, G. Wu, A. Feng, and L. Zhuo, "The effect of bis allyl benzoxazine on the thermal, mechanical and dielectric properties of bismaleimide–cyanate blend polymers," *RSC Advances*, vol. 5, no. 72, pp. 58821–58831, 2015.

[29] M. Jiang, X. Zou, Y. Huang, and X. Liu, "The effect of bismaleimide on thermal, mechanical, and dielectric properties of allyl-functional bisphthalonitrile/bismaleimide system," *High Performance Polymers*, vol. 29, no. 9, pp. 1016–1026, 2017.

[30] Z. Zhang, L. Yuan, G. Liang, and A. Gu, "Fabrication and origin of flame retarding glass fiber/bismaleimide resin composites with high thermal stability, good mechanical properties, and a low dielectric constant and loss for high frequency copper clad laminates," *RSC Advances*, vol. 6, no. 24, pp. 19638–19646, 2016.

[31] J. Qiu, Q. Wu, and L. Jin, "Effect of hyperbranched polyethyleneimine grafting functionalization of carbon nanotubes on mechanical, thermal stability and electrical properties of carbon nanotubes/bismaleimide composites," *RSC Advances*, vol. 6, no. 98, pp. 96245–96249, 2016.

Hindawi
Journal of Nanomaterials
Volume 2018, Article ID 5839037, 8 pages
https://doi.org/10.1155/2018/5839037

Research Article

Green Preparation, Spheroidal, and Superior Property of Nano-1,3,5,7-Tetranittro-1,3,5,7-Tetrazocane

Xinlei Jia, Jingyu Wang, Conghua Hou, and Yingxin Tan

School of Chemical and Environmental Engineering, Shanxi Engineering Technology Research Center for Ultrafine Powder, North University of China, Taiyuan, Shanxi 030051, China

Correspondence should be addressed to Conghua Hou; houconghua@163.com

Received 19 June 2018; Accepted 1 August 2018; Published 18 September 2018

Academic Editor: Chandragiri V. Reddy

Herein, a green process for preparing nano-HMX, mechanical demulsification shearing (MDS) technology, was developed. Nano-HMX was successfully fabricated via MDS technology without using any chemical reagents, and the fabrication mechanism was proposed. Based on the "fractal theory," the optimal shearing time for mechanical emulsification was deduced by calculating the fractal dimension of the particle size distribution. The *as*-prepared nano-HMX was characterized by X-ray diffraction (XRD), scanning electron microscopy (SEM), and differential scanning calorimetry (DSC). And the impact sensitivities of HMX particles were contrastively investigated. The raw HMX had a lower fractal dimension of 1.9273. The ideal shearing time was 7 h. The resultant nano-HMX possessed a particle size distribution ranging from 203.3 nm to 509.1 nm as compared to raw HMX. Nano-HMX particles were dense spherical, maintaining β-HMX crystal form. In addition, they had much lower impact sensitivity. However, the apparent activation energy as well as thermal decomposition temperature of nano-HMX particles was decreased, attributing to the reduced probability for hotspot generation. Especially when the shearing time was 7 h, the activation energy was markedly decreased.

1. Introduction

HMX has been widely used as the main component of high-energy explosives. It exhibits high energy density, good heat resistance, stable detonation, and high detonation speed. However, high mechanical sensitivity and poor shock wave sensitivity limit its application to a large extent [1]. With the rapid development of modern warfare and the deteriorating battlefield environment, the safety performance for weapons and ammunition becomes ever more critical. Ammunition need not only meet the requirements of long range, high precision, and strong power but also require insensitivity. Therefore, insensitivity has become an important indicator to measure the performance of explosives [2, 3]. One of the ways to achieve this goal is the ultrafining technology of explosives. Through refinement, the surface of the explosives becomes smooth, the particle size gets smaller, and the particle morphology tends to be spherical. In this case, the probability of hotspot generation and propagation is reduced, thus achieving desensitization [4].

In recent years, more and more researchers are devoted to the refinement of single explosives, mainly consisting of the nuclear growth method and the ultrafine grinding method to realize the ultrafining treatment. However, these two methods have their own obvious shortcomings. The nuclear growth method is to formulate ultrafine particles of a specified size by controlling conditions for crystal nucleation growth. During the preparation process, high temperatures may be required, which may cause explosive explosion and deflagration. In addition, the explosives refined by this method may undergo crystal transformation, thus affecting the sensitivity. Song et al. [5] used solvent-nonsolvent method to prepare ultrafine HMX. The raw material possessed β-HMX, but the refined particles contained γ-HMX, which could reduce the purity of the product. van der Heijden and Bouma [6] spheroidized HMX and RDX through simple mixing and stirring in a special solvent. However, the spheronization effect was not obvious, and the quality of the obtained crystal was poor. An et al. [7] prepared HMX with a particle size distribution of 40~130 nm by

green recrystallization process. The resultant HMX was polyhedron and spherical. However, there was a certain degree of crystal transformation during the recrystallization process, and a large amount of organic solvents were used in the experiment, so this method was not truly "green." Shang and Zhang [8] used different solvents to prepare HMX with different particle sizes by supercritical antisolvent method (GAS) recrystallization method. However, this method had a low yield, and the subsequent processing was troublesome. The ultrafine grinding method is to pulverize large-sized particles by a certain means to reduce the particle size. In the field of energetic materials, there are many reports on the preparation of ultrafine explosive particles via mechanical ball milling. However, there exist certain disadvantages in such process. With the increase of milling time, high temperature and high pressure appear in the barrel of the ball mill. In this way, on the one hand, the safety performance will be reduced; on the other hand, some physicochemical reactions (such as crystal transformation) may occur when the crystal grains are activated [9]. Liu et al [10] prepared nano-RDX by mechanical ball milling, which reduced the impact sensitivity by 30% and the friction sensitivity by 92.8%, but this method was easy to introduce impurities. Wang et al. [11] prepared HMX by wet milling, solvent-antisolvent, and wet sieve method. For particles obtained by solvent-antisolvent method, the particle size distribution was narrow and the surface was relatively smooth. However, the experiment has poor repeatability and serious environmental pollution.

In this work, based on the shortcomings of the above refinement process, we proposed an improved green approach to refine HMX, i.e., mechanical demulsification shearing (MDS) technology. This technology addressed the unfavorable factors of the existing refinement. First of all, this method effectively solved the problem of the crystal transformation of explosives, because the entire experiment was a physical process and no new substances and impurities were generated. Secondly, the whole process was highly repeatable, and no organic solvents were used throughout the experiment, thus achieving the goal of environmental protection. Finally, to achieve nanometerization, the explosives were refined by relying on mechanical shearing of explosive particles and collisions between particles in a narrow space. Therefore, this technology greatly improved the safety performance during the mechanical ball milling and avoided the introduction of impurities.

1.1. Experimental Section

1.1.1. Materials. HMX was provided by Gansu Yinguang Chemical Industry Group Co. Tween-80 and ethanol were from Tianjin Shen Tai Chemical Reagent Co., Ltd. Span-80 was obtained from Tianjin Damao Chemical Reagent Factory. Pure water is provided by pure water supply of Taiyuan Iron and Steel Co., Ltd.

1.1.2. Experimental Process. The experimental procedure for preparing nano-HMX via mechanical demulsification shearing (MDS) technology is as follows:

(1) Preparation of composite emulsifier. Composite emulsifier is obviously superior to single emulsifier in improving the stability of emulsion explosives. Based on this, 2.65 g Tween-80 and 2.35 g Span-80 were added to the beaker with $M_{(\text{Tween-80})} : M_{(\text{Span-80})}$ of 53 : 47. Stir for 10 minutes under the action of a magnetic stirrer until the emulsion was completely mixed and then set aside.

(2) Preparation of HMX emulsion. Diluted HMX (10 g) and purified water (500 ml) were added to the beaker, respectively; then, a certain amount of self-made composite emulsifier was added to the beaker, too. The stirring speed was set as 500 rad/min, and the mixed solution was uniformly stirred for 40 min at 30°C. Here, a homogenous HMX emulsion was obtained.

(3) Preparation of nano-HMX by MDS. The beaker containing the HMX emulsion was placed under the emulsifying machine. Then slowly increase the speed to 7500 rad/min and continue stirring (the reaction process was carried out in a low temperature circulating condensate pump, and the shear temperature was maintained at 40°C throughout the experiment). After stirring, the solution was let to stand, followed by filtration and natural drying for 12 hours, affording high-quality nano-HMX particles.

As shown in Figure 1, due to strong fluid shear and severe high-frequency mechanical effects, the HMX emulsion was sucked into the rotor from the bottom of the beaker for strong mixing. Then, it threw from stator gap and hit each other under the action of centrifugal force. Driven by high-speed rotating stator, HMX particles collided with each other in a small space (in the long-hole rotor). And plus the constant shear of the fluid, the nano-HMX was finally obtained. In order to explore the optimal shearing time by MDS, under the same experimental conditions, we cut the *as*-prepared nano-HMX at different time points of 4 h, 5 h, 6 h, 7 h, and 8 h and labeled them as nano-HMX-1, nano-HMX-2, nano-HMX-3, nano-HMX-4, and nano-HMX-5, respectively.

1.2. Characterization. Field-emission scanning electron microscopy (FESEM) images were taken on a MIRA3 LMH SEM (TESCAN) at 10 k. X-ray diffraction (XRD) patterns were obtained using a DX-2700 (Dandong Haoyuan Corporation, Liaoning, China) X-ray diffractometer with Cu-Kα (40 kV, 30 mA) radiation at $\lambda = 1.5418$ Å. All samples were scanned from 5° to 50° with steps 0.03 and 6 s counting time. Thermal analysis was performed on a differential scanning calorimeter (DSC-131, France SETARAM Corporation, Shanghai, China) at heating rates of 5, 10, 15, and 20°C/min. The impact sensitivity was tested with a homebuilt type 12 drop hammer apparatus. The special height (H50) represents the height from which 2.500 ± 0.002 kg drop hammer will result in an explosive event in 50% of the trials. In each determination, 25 drop tests were made to calculate the H50. The particle size tested by QICPIC dynamic particle

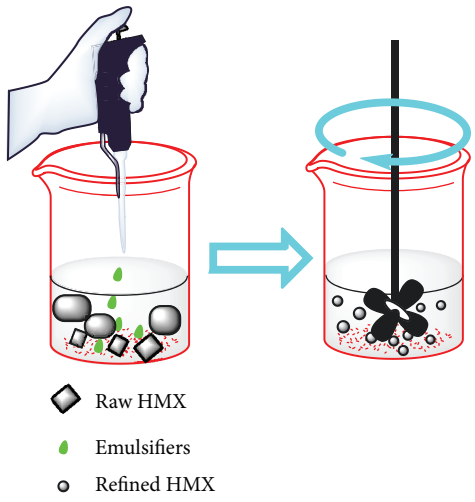

Figure 1: Schematic formation of nano-HMX.

analyzer (Sympatec Co., Ltd., Germany), and its working environment is 5~35°C, relative humidity is less than 85%, light source type is He-Ne laser, power is 2.0 mW, and wavelength is 0.6328 μm.

2. Results and Discussion

2.1. SEM Images of HMX Samples. Field-emission scanning election microscope (FESEM; HITACHI S4700) was used to display typical SEM images of HMX samples in Figure 2.

As observed in Figure 2, raw HMX is irregular in shape and has a wide and uneven particle size distribution, and there exist cracks. However, nano-HMX prepared via MDS performs better qualities. With the increase of the emulsification shearing time, the particle size gradually becomes smaller, the surface becomes smoother, the particle distribution is more uniform, and the morphology gets close to spherical in shape. Therefore, from the apparent analysis, it contributes to reducing the sensitivity. In particular, nano-HMX as prepared at the emulsification shearing time of 7 h has the best morphology and particle size distribution. When the shearing time is less than 7 h (as shown in Figures 2(b)–2(d)), the distribution of HMX particles is noticeably uneven, and there are particles with large morphology. While the shearing time is greater than 7 h (Figure 2(f)), the particles are severely agglomerated. This can be explained by the granularity fractal theory [12] of nano-HMX particles. The analysis of the particle size distribution of raw HMX and nano-HMX as prepared by MDS shows that the refined nano-HMX particle size distribution is unimodal (Figure 3), which is in good accordance with the granularity fractality of powder particles [13]. In other words, the particle size distribution of HMX has the fractal feature, which satisfies formula (1):

$$Y\omega(d) \infty d^{3-D}, \tag{1}$$

where d is the particle diameter, $Y\omega(d)$ is the ratio of the total mass of particles less than d to the total mass of all particles in the particle system, and D is the fractal dimension. According to formula (1), if there is a linear correlation between ln $Y\omega(d)$ and ln d, it means that the particle size distribution of the powder has fractal characteristics. If the straight line slope k is obtained, the fractal dimension of the particle size distribution can be calculated as $D = 3 - k$. And the fractal analysis of the particle size distribution of nano-HMX particles is further performed, listed in Table 1.

As Table 1 represents, as the shearing time increases, the particle size of nano-HMX gradually decreases. The correlation coefficient of the straight line of the double logarithmic coordinate system is as high as 0.9898–0.9976, which indicates that the particle size distribution of the raw HMX and the refined HMX has fractal phenomenon. And the particle size distribution of raw HMX has a lower fractal dimension of only 1.9273, which is easily broken. When the shearing time is 4~7 h, the particle size distribution dimension of nano-HMX gradually increases. While when the shearing time is 6~7 h, the fractal dimension decreases slightly, attributing to severe agglomeration between ultrafine particles. And the density of agglomerated particles is slightly lower than that of other particles, thus affecting the proportional relationship in formula (1). From the above discussion, we can see that when the shearing time is 7 h, the resultant nano-HMX has a narrow particle size distribution and smooth surface, and the particle agglomeration is not obvious. Therefore, the shearing time of 7 h is the best time to fabricate nano-HMX via MDS method.

2.2. Crystal Structure of HMX Samples. XRD analysis was carried out to investigate whether the phase transformation of HMX occurred. X-ray diffraction of HMX samples is displayed in Figure 4:

As illustrated in Figure 4, using the JADE software, nano-HMX (JCPDS no. 00-044-1620) has the same crystal structure as raw HMX at 2θ of 12.32°, 14.17°, 19.25°, 22.11°, and 32.27°. It reveals that the crystal structure of the refined HMX is consistent with that of the raw HMX, both maintaining β-form. The peak of the nano-HMX is much weaker and wider than that of the original HMX, which can be explained by the Scherrer formula (formula 2). The particle size of the particles is inversely proportional to the peak width of the diffraction peak. And it is precisely because the size of ultrafine HMX becomes smaller, resulting in widening of diffraction peaks [14, 15]. Also, this phenomenon indicates that the HMX crystals are nanosized.

$$D_{hkl} = k\frac{\lambda}{\beta}\cos\theta, \tag{2}$$

where D_{hkl} is the grain diameter perpendicular to the crystal plane (hkl), k is the Scherrer constant (usually 0.89), λ is the incident X-ray wavelength (wavelength is 1.5418 Å), θ is the Bragg diffraction angle (°), and β is the peak width of diffraction peak at half height (rad).

2.3. DSC Analysis of Different HMX Particles. Thermal stability is widely considered as a key performance for

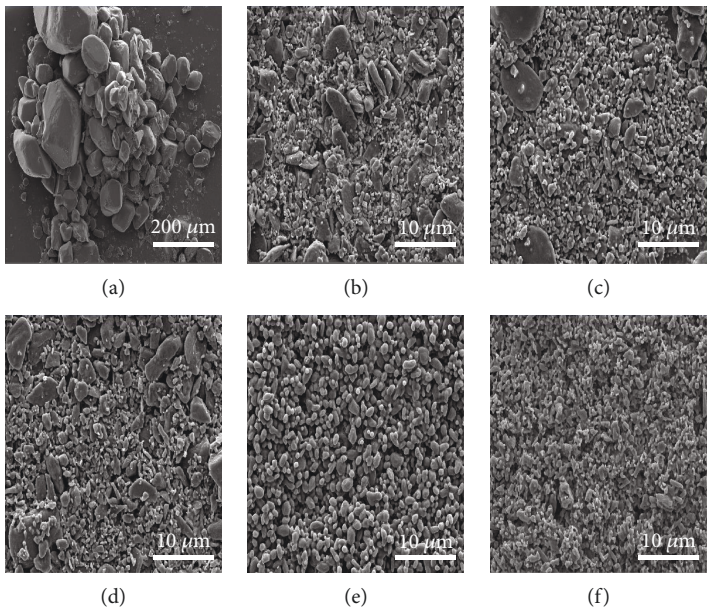

Figure 2: Displays typical SEM images of the HMX samples before and after refined.

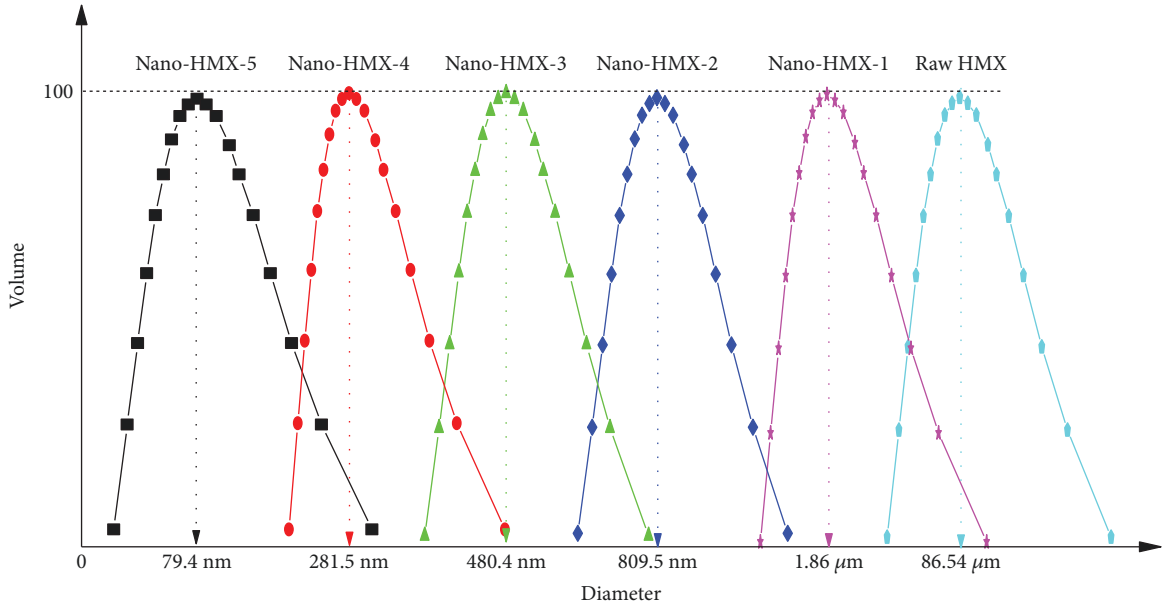

Figure 3: Particle size and size distribution of HMX particles.

Table 1: Fractal geometry analysis data of HMX particles.

Samples	Shearing time/h	Mean diameter	The dispersion dimension	Correlation coefficients
Raw HMX	0	86.54 μm	1.9273	0.9938
Nano-HMX-1	4	1.86 μm	2.7499	0.9989
Nano-HMX-2	5	809.5 nm	2.7534	0.9898
Nano-HMX-3	6	480.4 nm	2.8497	0.9971
Nano-HMX-4	7	281.5 nm	2.9600	0.9914
Nano-HMX-5	8	79.4 nm	2.3501	0.9976

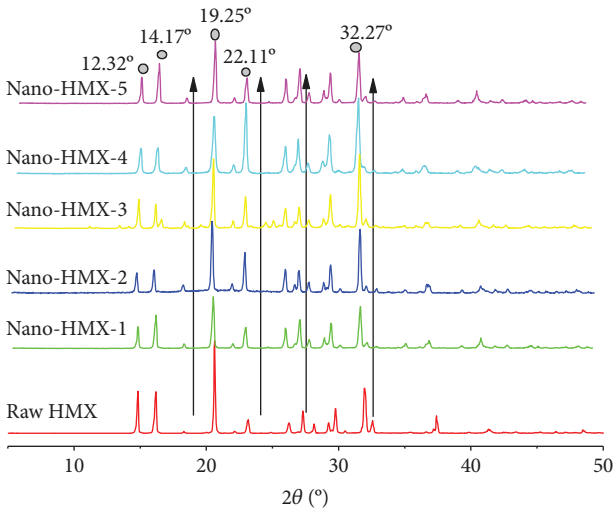

Figure 4: XRD spectra of HMX particles.

energetic materials [16]. In our paper, thermal properties of raw HMX and nano-HMX were analyzed by DSC, and their activation energy was calculated. And the changes of thermal properties before and after refinement were compared.

Figure 5 shows that for different heating rates, the decomposition peak temperatures of raw HMX and nano-HMX increase with the enhancement of the heating rate. By Kissinger equation [17–20] (3), from the four exothermic peaks at heating rates of 5 K/min, 10 K/min, 15 K/min, and 20 K/min, their apparent activation energy and preexponential factor can be calculated, respectively.

$$\ln\left(\frac{\beta_i}{T_{pi}^2}\right) = \ln\left(\frac{AR}{E_a}\right) - \frac{E_a}{RT_{pi}}, \tag{3}$$

where β_i is the heating rate (K/min); T_{pi} is the decomposition peak temperature of the explosive at different heating rates; A is the preexponential factor ($\min^{-1}$); R is the gas constant, 8.314 J/(mol·K); and E_a is the apparent activation energy.

As shown in Figure 6, taking $1/T_p$ as the abscissa and $\ln(\beta/T_p^2)$ as the ordinate, we performed linear fitting on the measurement results and found that the fitting coefficient R is as high as 0.99537~0.99911. Using E_a and 4, when the heating rate of HMX approaches 0, the peak temperature T_{p0} can be obtained. Then, through the calculation formula (5), the critical temperature of thermal explosion T_b can be calculated. And the results are listed in Table 2.

$$T_{pi} = T_{p0} + b\beta_i + c\beta_i^2, \tag{4}$$

$$T_b = \frac{E - \sqrt{E^2 - 4RET_{p0}}}{2R}. \tag{5}$$

It can be seen from Table 2 and Figure 7 that the E_a and thermal decomposition peak temperatures of the nano-HMX particles are lower than those of the raw HMX, indicating that nano-HMX is more susceptible to decomposition than raw HMX under thermal stimuli. When the shearing time reaches 8 h, E_a decreases from 485.28 to 427.84 kJ/mol, and the thermal stability of HMX decreases significantly. Such change can be attributed to the fact that for the same quality HMX, the smaller the particle size is, the larger the surface area will be. At a certain heating rate, the external energy absorbed by the particles increases for a period of time, and the heated area and the reactivity increase. In addition, owing to the massive agglomeration of particles, its specific surface area and the number of atoms located on the surface increase [21, 22]. Therefore, E_a and the thermal decomposition temperature have decreased as compared to the raw HMX.

2.4. The Impact Sensitivity Analysis. Impact sensitivity is also a key parameter to evaluate the safety performance of energetic materials. The impact sensitivities of the HMX samples were separately tested according to GJB 722 A-1997 method 610. 302 tool. The impact sensitivity test results are shown in Figure 8.

As illustrated in Figure 8, compared with the raw material, the H50 of nano-HMX particles gradually increases with the increase of the shearing time. This can be explained by the hotspot theory [23–25]. On the one hand, as the shearing time increases, the appearance of the HMX particles gradually becomes smoother, and the internal defects gradually decrease, so that the heat transfer rate between the particles increases. When subjected to external forces, it is difficult to form hotspots. On the other hand, for HMX of the same quality, the smaller the particle size is, the more effective the spheroidization will be. As a result, the specific surface area and the gap between the particles increase, resulting the decreased pressure from which the HMX will suffer for the same height falling ball. Therefore, the characteristic height H50 of nano-HMX increases visibly, thus improving the safety performance.

3. Conclusion

The superiority of nano-HMX fabricated by mechanical demulsification shearing (MDS) technology was demonstrated, namely, green preparation, spherical shape, and high-quality properties. More importantly, this method solves the defects of the conventional technology when refining HMX, such as crystal transformation, impurity generation, troublesome follow-up processing, complicated process, and serious pollution. In the paper, nano-HMX was prepared in this way. Based on the experimental analysis, the mechanical emulsification shearing (MDS) technology was proposed through the "fractal theory." The best shearing time for preparing nano-HMX was 7 h. Under this condition, the *as*-prepared particles tended to possess a spherical morphology and uniform particle size distribution. And no crystal transformation occurred. Compared with the raw HMX, the resultant HMX particles will have better safety performance. However, the apparent activation energy and the thermal decomposition temperature of nano-HMX particles can be decreased,

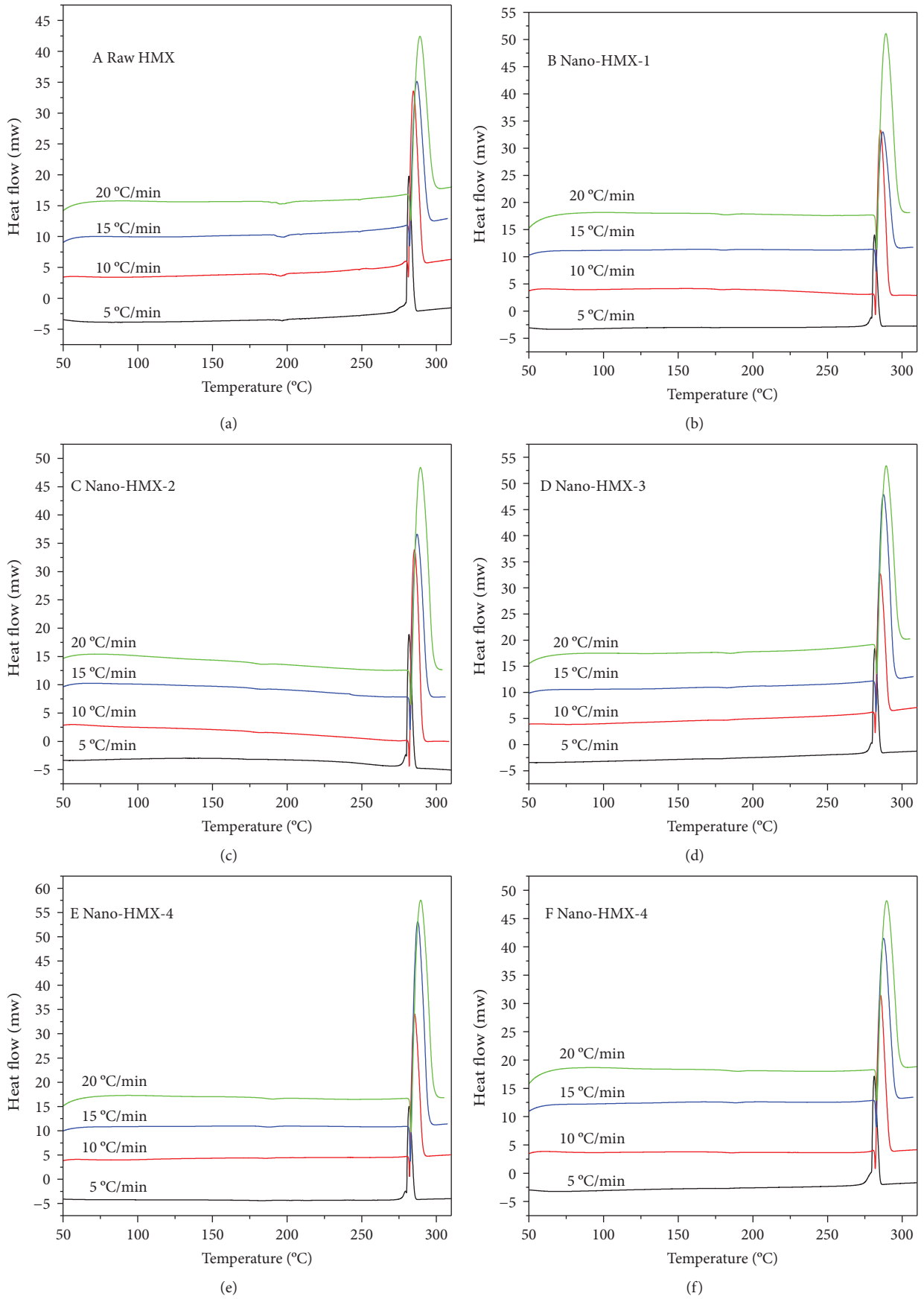

Figure 5: DSC curves of HMX particles.

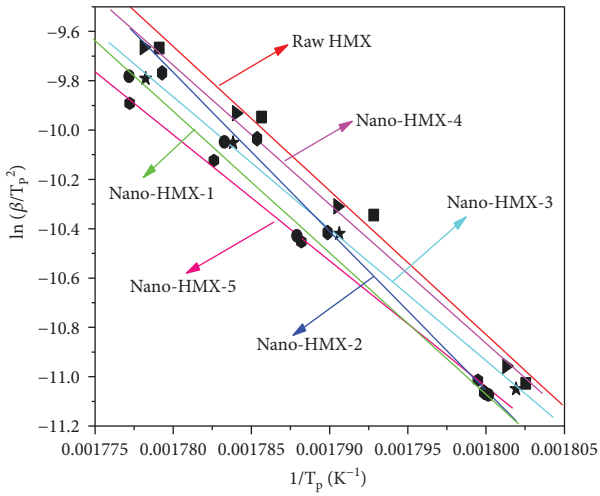

Figure 6: Kissinger's plots of $\ln(\beta/T_p^2)$ vs. reciprocal peak temperature $1/T_p$ for raw HMX and nano-HMX. Symbol R is used to identify the linear correlation coefficient of $\ln(\beta/T_p^2)$ to $1/T_p$.

Table 2: Thermal decomposition kinetic parameters of different HMX samples.

Samples	E_a/kJ·mol^{-1}	log(A·S^{-1})	T_b/°C	T_{p0}/°C
Raw HMX	485.28	45.69	278.68	277.35
Nano-HMX-1	470.00	44.23	276.60	275.25
Nano-HMX-2	468.50	44.08	277.35	275.98
Nano-HMX-3	468.01	44.03	277.82	276.45
Nano-HMX-4	460.79	43.34	277.92	276.53
Nano-HMX-5	427.84	10.24	276.41	274.93

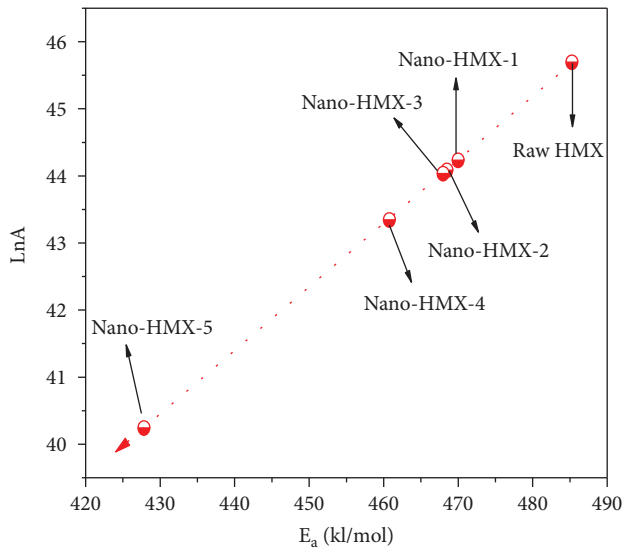

Figure 7: Kinetic compensation effect for thermal decomposition of HMX samples.

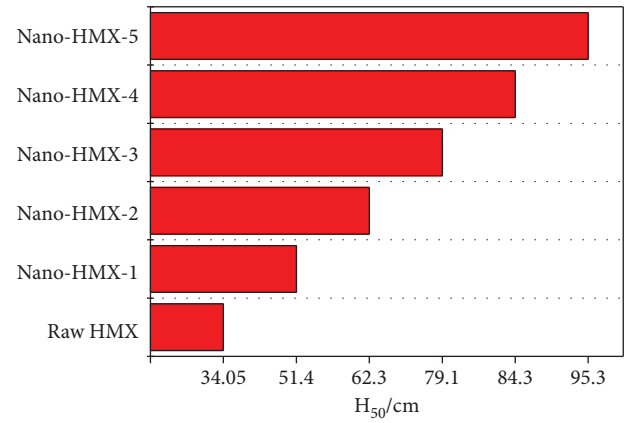

Figure 8: Impact sensitivities of HMX samples.

attributing to the reduced hotspot generation probability of the refined particles.

Data Availability

The data used to support the findings of this study are available from the corresponding author upon request.

Conflicts of Interest

The authors declare that they have no conflicts of interest.

References

[1] X. Mao, L. Jiang, C. Zhu, and X. Wang, "Effects of aluminum powder on ignition performance of RDX, HMX, and CL-20 explosives," *Advances in Materials Science and Engineering*, vol. 2018, Article ID 5913216, 8 pages, 2018.

[2] D. M. Badgujar, M. B. Talawar, S. N. Asthana, and P. P. Mahulikar, "Advances in science and technology of modern energetic materials: an overview," *Journal of Hazardous Materials*, vol. 151, no. 2-3, pp. 289–305, 2008.

[3] S. M. Walley, J. E. Field, and M. W. Greenaway, "Crystal sensitivities of energetic materials," *Materials Science and Technology*, vol. 22, no. 4, pp. 402–413, 2006.

[4] H. Liu, G. Deng, Y. Yang, and F. N. Li, "Study on the superfining of explosive by LS superfine pulverizers," *Explosive Materials*, vol. 33, no. 5, pp. 32–35, 2004.

[5] X. Song, Y. Wang, C. An, X. Guo, and F. Li, "Dependence of particle morphology and size on the mechanical sensitivity and thermal stability of octahydro-1,3,5,7-tetranitro-1,3,5,7-tetrazocine," *Journal of Hazardous Materials*, vol. 159, no. 2-3, pp. 222–229, 2008.

[6] A. E. D. M. van der Heijden and R. H. B. Bouma, "Crystallization and characterization of RDX, HMX, and CL-20," *Crystal Growth & Design*, vol. 4, no. 5, pp. 999–1007, 2004.

[7] C. An, H. Li, W. Guo, X. Geng, and J. Wang, "Nano cyclotetramethylene tetranitramine particles prepared by a green recrystallization process," *Propellants Explosives Pyrotechnics*, vol. 39, no. 5, pp. 701–706, 2015.

[8] F. F. Shang and J. L. Zhang, "Effect of solvent on particle morphology and crystal phase in recrystallization of HMX by different supercritical carbon dioxide as antisolvent," *Initiators & Pyrotechnics*, vol. 1, pp. 16–20, 2014.

[9] M. L. Panchula and J. Y. Ying, "Mechanical synthesis of nanocrystalline α-Al_2O_3 seeds for enhanced transformation kinetics," *Nanostructured Materials*, vol. 9, no. 1–8, pp. 161–164, 1997.

[10] J. Liu, L. I. Qing, and J. Zeng, "Mechanical pulverization for the production of sensitivity reduced nano-RDX," *Explosive Materials*, vol. 42, no. 4, pp. 1–4, 2013.

[11] Y. Wang, X. Song, D. Song, W. Jiang, H. Liu, and F. Li, "Dependence of the mechanical sensitivity on the fractal characteristics of octahydro-1,3,5,7-tetranitro-1,3,5,7-tetrazocine particles," *Propellants, Explosives, Pyrotechnics*, vol. 36, no. 6, pp. 505–512, 2011.

[12] Y. Liu, Z. Wang, and T. Chai, "Influence of HMX particle size and gradation on the shock sensitivity and output of a PBX explosive," *Acta Armamentarii*, vol. 4, pp. 357–360, 2000.

[13] X. L. Song, X. D. Guo, J. L. Zhang, C.-W. An, and F.-S. Li, "Dependence of size and size distribution on safety performance of nitroamine explosives and the multi-component explosives," *Initiators & Pyrotechnics*, vol. 16, no. 4, pp. 17–21, 2007.

[14] C. An, P. Ding, B. Ye, X. Geng, and J. Wang, "Carbon-coated copper nanoparticles prepared by detonation method and their thermocatalysis on ammonium perchlorate," *AIP Advances*, vol. 7, no. 3, article 035324, 2017.

[15] J. Liu, J. Wei, F. Li et al., "Effect of drying conditions on the particle size, dispersion state, and mechanical sensitivities of nano HMX," *Propellants, Explosives, Pyrotechnics*, vol. 39, no. 1, pp. 30–39, 2014.

[16] Q. L. Yan and S. Zeman, "Theoretical evaluation of sensitivity and thermal stability for high explosives based on quantum chemistry methods: a brief review," *International Journal of Quantum Chemistry*, vol. 113, no. 8, pp. 1049–1061, 2013.

[17] H. E. Kissinger, "Reaction kinetics in differential thermal analysis," *Analytical Chemistry*, vol. 29, no. 11, pp. 1702–1706, 1957.

[18] W. Sha, "Determination of activation energy of phase transformation and recrystallization using a modified Kissinger method," *Metallurgical and Materials Transactions A*, vol. 32, no. 11, pp. 2903-2904, 2001.

[19] M. F. Foltz, C. L. Coon, F. Garcia, and A. L. Nichols, "The thermal stability of the polymorphs of hexanitrohexaazaisowurtzitane, part I," *Propellants, Explosives, Pyrotechnics*, vol. 19, no. 1, pp. 19–25, 1994.

[20] B. Ye, C. An, Y. Zhang, C. Song, X. Geng, and J. Wang, "One-step ball milling preparation of nanoscale CL-20/graphene oxide for significantly reduced particle size and sensitivity," *Nanoscale Research Letters*, vol. 13, no. 1, p. 42, 2018.

[21] C. Hou, X. Jia, J. Wang, Y. Tan, Y. Zhang, and C. Li, "Efficient preparation and performance characterization of the HMX/F_{2602} microspheres by one-step granulation process," *Journal of Nanomaterials*, vol. 2017, Article ID 3607383, 7 pages, 2017.

[22] C. H. Hou, X. L. Jia, J. Y. Wang, and X. M. Jiang, "Preparation of refinement HMX by non-solvent and its performance characterization," *Chinese Journal of Explosives & Propellants*, vol. 39, no. 4, pp. 27–31, 2016.

[23] X. L. Jia, C. H. Hou, Y. X. Tan, J. Y. Wang, and B. Y. Ye, "Fabrication and characterization of PMMA/HMX-based microcapsules via in situ polymerization," *Central European Journal of Energetic Materials*, vol. 14, no. 3, pp. 559–572, 2017.

[24] Z. Li, Y. Wang, Y. Zhang, L. Liu, and S. Zhang, "CL-20 hosted in graphene foam as a high energy material with low sensitivity," *RSC Advances*, vol. 5, no. 120, pp. 98925–98928, 2015.

[25] Y. Wang, X. Song, D. Song, L. Liang, C. An, and J. Wang, "Synthesis, thermolysis, and sensitivities of HMX/NC energetic nanocomposites," *Journal of Hazardous Materials*, vol. 312, pp. 73–83, 2016.